Swift heavy ion induced effects in III-V compound semiconductors

Thesis submitted for the degree of

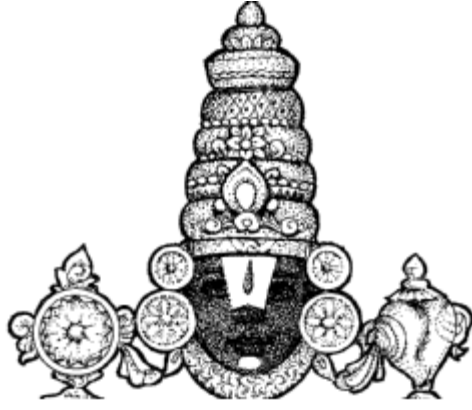## Doctor of Philosophy

by

Devaraju Gurram

School of Physics
University of Hyderabad
Central University P O
Gachibowli, Hyderabad-500 046
India
January 2012

&

To my parents and Gurus

DECLARATION

I hereby declare that the work embodied in this thesis entitled "**Swift heavy ion induced effects in III- V compound semiconductors**" carried out by me, under the supervision of **Prof. Anand P Pathak**, School of Physics, University of Hyderabad, Hyderabad, India, has not been submitted for any other degree or diploma either in part or in full to this or to any other University or Institution.

(**G Devaraju**)

Place: Hyderabad

Date:

CERTIFICATE

This is to certify that the work described in this dissertation entitled "**Swift heavy ion induced effects in III- V compound semiconductors**" has been carried out by Mr. G Devaraju under my direct supervision for the full period prescribed under PhD ordinances of the University and the same has not been submitted for any other degree or diploma to this or any other University or Institution.

(**Dean, School of Physics**)   (**Prof. Anand P Pathak**)

                                                                    (**Thesis Supervisor**)

Place: Hyderabad

Date:

Acknowledgements

It is a great pleasure to thank my mentor, teacher, philosopher and guide Prof A P Pathak who has been instrumental in inculcating scientific temper at various levels at varied frequencies. I used to have discussions regularly on day-to-day assignments. This eventually enhanced my subject understanding and substantiated logics in due course of study. Many a times, in spite of his busy schedule, I was lucky enough to get him in time for discussions. It is rare to have such dedicated and determined teacher. I usually owe to him as my classical guru like Lord Krishna. He taught us value of work and consequences of it either directly or indirectly (Miles to go before I sleep). Just as an example, when he was admitted to hospital for his heart surgery, his strength was such that the recovery time was faster than the operation time. Most interestingly, even at those critical times he was busy in correcting my manuscript. In other words, his acts of intelligence and deeds have been most influential and imprinted in me which cannot be wiped out so easily. Over the years he built several collaborations across the world with outstanding scientists, which eventually gave us ample opportunities to interact and discuss our ideas. As a consequence of that, I could visit the best labs across the globe for collaborative research work. I once again thank Prof Pathak for his unprecedented help and support. Discussions with Kittu about his project work enabled me in updating printing technology. Finally, my family members are indebted to his family for their endless help and encouragement starting from M Sc to PhD days.

I thank Dr D K Avasthi for his valuable suggestions during beam time experiments. His indirect way of obtaining answers by logical sequence of questions has influenced me a lot. During discussion, he always gives emphasis on inferences preceded by reasoning and logic. I am also thankful to the members of Pelletron group and other supporting labs in Inter University Accelerator Centre for necessary support during the experiments. Mr Saif Khan has been very innovative and enthusiastic in extending help during the experiments. I thank him for that.

Prof B M Arora of TIFR (now at IITB) has taught me HRXRD in my early stages of research career. I understood and comprehended the importance of X-ray work for

Dr S Dhamodaran has given me enough impetus during my initial days to research. I still remember his discussions and his passion for research during our visit to TIFR for HRXRD and PL measurements. I thank him for his help. Dr Sai Sravanan of Gallium Arsenide Enabling Technology Centre (GAETEC) enabled me to understand different advanced technologies. I thank him for extending support to use Rapid Thermal Annealing (RTA) facility. Most of the time, I was with Dr N Sathish who is friendly and helpful in any situation. His enlightened thinking enabled us to perform different experiments. I thank him for his support and discussions throughout my PhD course. Dr Juby George is very jovial and helpful with whom I had good interactions. I thank her for the support. I thank Dr N Srinivasa Rao for helping me in many situations. He is always instrumental in bringing any situation to cordial. Mr V Saikiran is very friendly and ready to accept any challenge. I wish him all the best. Ms. Vendamani and Mr Manikanthababu are greatly acknowledged for their support.

I also thank technical staff Mr Laxminarayana , Mr Thirumalaiah and Mr Durga Prasad for their help. I thank all my M Sc (P Srinivas, N Srinivas, Ramu, Devendra, Swaroop, Venkat Ram) and PhD (Ugendhar, Namani Srinivas, Shankaraiah, Parthu, Vasu, Sita, Deepak, Anil, Sadik, Rambabu, Sendil, Vijayan, Venkaiah) classmates for their help. I also thank all my IUAC friends (Prikishit, Shivpoojan, Rahul, Sunilkalkal, Abhinav, Babu). I also thank Dr Lakshmi and Shri Sunny family for their support during our stay IUAC,New Delhi.

It is my sincere thanks to Dr C Ramaiah for his unconditional love and mercy towards me. He has been source of inspiration since my childhood. He is always there to safeguard my interests. It is he who has supported my education for all these years. As a guardian and teacher, what best he could do to me has been done. I, Swapna and Animesh are indebted to him for his unprecedented help. Dr C Srinivas and Dr C Padma have influenced my thinking through their scientific discussions. I also thank them for their wonderful support and encouragement. He has been my all time source of inspiration. I take this opportunity to thank Shri Achu and Shri Raji and their families for their extraordinary help.

TABLE OF CONTENTS

Chapter VII

My CV with list of publications

Synopsis

Ion beams are extensively used for modification and characterization of different materials. Ion beams under low energy regime (~ 1 keV/amu), on one hand, are being used for ion implantation to fabricate the IC circuits and on the other hand, for characterizing different materials for depth dependence study of composition (RBS, NRA,PIXE). Here, most of the energy loss to the target is via elastic collisions resulting in atomic displacements and is called nuclear stopping. In the swift heavy ion regime (~ 1 MeV/amu), ions deposit energy via inelastic collisions to target electrons resulting in electronic excitation and ionization and the process is called electronic stopping [1-4]. It is understood that high density of electronic excitations initiates radiation damage and defects migration [5,6]. Swift heavy ion (SHI) irradiation induced damage annihilation has also been reported in InP and GaAs [7,8]. The weakening of chemical bonds due to ion solid interactions in matter is not yet completely understood [9-11]. Moreover, understanding SHI induced effects in III- V compound semiconductors is far from mature. In this thesis, much emphasis has been laid in understanding defects creation and annihilation as well as strain and band gap engineering. There are pertinent questions related to critical radiation damage and its effects on free carrier concentrations in hetero-structures (HS) and multi quantum wells (MQWs). This is the motivation for current thesis work entitled "Swift heavy ion induced effects in III- V compound semiconductors". In the first chapter, motivation and aim of the thesis work has been described. Second chapter includes all the experimental details that are used towards these investigations. Third chapter describes introduction, results and discussion on Ion beam modification studies in InGaAs/InP MQWs. Fourth chapter describes electronic energy loss dependence studies in metal organic chemical vapour deposition (MOCVD) grown GaN/ Al_2O_3. Defects densities and shift in phonon modes as a function of electronic energy loss have also been discussed in this chapter. Fifth chapter describes Swift heavy ion induced effects in MOCVD grown AlGaN/GaN MQW's. Photoluminescence and Rocking curve measurements as function of fluence and electronic energy loss are also described here. Sixth chapter explains vividly how Ion beams modify nearly lattice matched and tensile strained AlInN/GaN HS. All the conclusions derived from above chapters and future outlook are comprehended in the final (seventh) chapter.

Chapter I

Introduction

This chapter describes motivation and aim of this thesis work by citing pertinent literature. Most importantly, basics of ion solid interactions and their consequences in material properties are discussed. Materials of interest for this work are discussed very lucidly. Much emphasis has been laid in understanding the effects of ion beams on strain, band gap engineering, interfaces, surface morphology and creation or annihilation of defects in III-V compound semiconductors. Importance and limitation of Thermal spike and Coulomb explosion models are compared and how these models are essential in interpreting current results are also discussed.

Chapter II

Experimental Details

This chapter includes all experimental details that have been used in this work. III-V compound semiconductors inlcudes InGaAs/InP, GaN, AlInN/GaN hetero structures (HS) and Multi Quantum Wells (MQWs). InGaAs/InP, AlGaN/GaN MQWs have been grown using metal organic chemical vapour deposition (MOCVD) at Warsaw, Poland. AlInN/GaN HS have been grown using MOCVD at TIFR, Mumbai. Subsequently, these films were subjected to heavy ion bombardment for engineering strain and band gap. Swift heavy ion irradiation on strained structures has been carried out using the 15MV pelletron at IUAC New Delhi. RBS work has been done using the 1.7MV tandetron facility at IGCAR Kalpakkam. Pristine and irradiated samples were characterized by different characterization techniques like High resolution X ray diffraction (HRXRD), Micro Raman, Atomic Force Microscope (AFM), Scanning Electron Microscopy (SEM), Photoluminescence (PL) and Transmission electron microscopy (TEM). Necessary theory and instrumentation part for each of the above mentioned characterization techniques are discussed in detail.

Chapter III

Ion beam modification studies in InGaAs/InP multi quantum wells

This chapter describes effects of heavy ion bombardment on the interfaces of MQWs. Importance of materials and their consequences on tailoring strain and band gap engineering under charged particle bombardment has been emphasized. Effects of irradiation and subsequent annealing in engineering band gap are discussed. Tensile strained InGaAs/InP Multi quantum wells were investigated before and after irradiation using different characterization techniques like HRXRD, AFM and PL for interfaces, surface morphology and band gap, respectively [12]. It is concluded that irradiation improves interface quality but changes strain which is correlated with the increase in band gap. Band gap shift of 40 meV and 70 meV has been observed for the irradiated ion fluences of 5×10^{12} and 1×10^{13} ions/cm^2 ,and subsequent annealing, respectively. AFM studies revealed no significant change in surface morphology.

Chapter IV

Electronic energy loss dependence studies in MOCVD grown GaN/ Al$_2$O$_3$

GaN (5micron) thick samples on Al$_2$O$_3$ along (0001) have been used. These samples were irradiated with 80 MeV Ni and 100 MeV Ag ions at a fixed fluence of 1×10^{13} ions/cm^2 followed by rapid thermal annealing (RTA) at 700°C in nitrogen atmosphere for 60 sec to anneal out irradiation induced defects. Ion species and energies are chosen such that the difference in their electronic energy loss (S$_e$) would be significant (in this case it is 8 keV/nm). Effects of Ag on structural and optical properties over Ni ions have been discussed extensively. We have also investigated damage creation and annihilation under energetic ion bombardment at a fixed fluence. The effects of defects on luminescence were studied with photoluminescence measurements. Band to band transitions are observed from pristine samples but there is no evidence of them on irradiated GaN. It shows a BL band at 450 nm besides YL emissions from Ni ion irradiated GaN. It seems

that a high concentration of radiation annealed gallium vacancies have a quenching effect on YL emission intensity while the vacancy concentration of nitrogen favors BL. PL measurements show the effective reduction in YL intensity with irradiation and subsequent thermal annealing [13].

On the other hand, HRXRD and Raman characterization techniques were used to understand the defect densities and lattice vibrations upon irradiation, respectively. Defect densities from pristine and irradiated samples are calculated and compared using Williamson–Hall method. Change of strain and vibrational modes as a function of S_e has been discussed. Increase in crystalline nature and induced compressive strain upon irradiation has been noticed from decrease of FWHM and shift in Bragg peak to lower angles. Defect densities from W–H plots show that irradiation leads to increase in defect densities. Raman studies yield E_2 mode that is sensitive to local strain. Blue shift in E_2 mode for higher S_e value is attributed to compressive strain [14]. The variation of the line shape of the A_1 (LO) mode of GaN with S_e is basically due to the coupling of A_1 (LO) mode with an over damped Plasmon.

Chapter V

Swift heavy ion induced effects in MOCVD grown AlGaN/GaN MQWs

III-nitride strained layer super lattices offer extra degree of freedom to alter the band gap of lattice-mismatched HS. Swift Heavy Ion (SHI) irradiation is a post growth technique to alter the band gap of semiconductors, spatially. In the present study, strained AlGaN/GaN Multi Quantum wells (MQWs) were grown on sapphire with insertion of AlN and GaN as buffer layers between substrate and epi-layers by MOCVD. Such grown AlGaN/GaN MQWs were irradiated with 200 MeV Au , 120 MeV Au and 80MeV Ni ions at a fluence of 5×10^{11} , 1×10^{12} and 3×10^{12} ions/cm^2. Several symmetric and asymmetric scans are recorded to estimate in plane and out of plane strains. Increase in intensity of satellite peaks of AlGaN/GaN MQWs has been attributed to SHI induced dynamical annealing processes. Measured values show that lattice mismatch increases upon irradiation. However, increase in the mismatch upon irradiation has affected the band gap of MQWs, which has been confirmed by PL measurements. PL shows [15] that there is an increase

of intensity of luminescence of GaN and MQWs by one order of magnitude upon irradiation, which is attributed to SHI induced dynamic annealing processes.

It is known for long time that defect propagation direction plays vital role for device performance. High angle annular dark filed- scanning transmission electron microscopy (HAADF-STEM) has been used to understand the nature of interfaces of MQWs and buffer layers. HAADF-STEM gives not only the thickness of individual layers but also the position of individual atomic columns. Diffraction pattern at the interfaces of AlN and sapphire has shown deviations due to large lattice mismatch. Improved interface quality and reduced defect propagation along c-axis has been observed due to AlN and GaN buffer layers. HAADF –STEM of AlGaN/GaN MQWs are compared with that of the BF-TEM and noticed that HAADF-STEM better resolves MQWs. HAADF-STEM is a power full technique to get exact value of thickness, quality of interfaces and defect propagation. The composition gradient as a function of Se with analytical HAADF-STEM has also been studied and consequently has been verified with other complementary techniques like HRXRD. Interface quality has been analyzed with aberration corrected HRTEM images. HRXRD and Micro-Raman studies [16] have been carried out to understand ion beam induced strain and vibrational modes, respectively. Finally, the effects of ion beams on MQW's interfaces have been discussed.

Chapter VI

Structural changes induced by swift heavy ion beam in AlInN/GaN heterostructures

Tensile strained $Al_{(1-x)}In_xN/GaN/ Al_2O_3$ (0001) HS were realized using MOCVD technique with indium composition as 12 % and 17 %. These structures were irradiated with 100 MeV Ag and 70 MeV Ni ions at a varied fluences 1×10^{12} and 3×10^{12} ions/cm^2. Under this energy regime, the structural changes in $Al_{(1-x)}In_xN$ would occur due to the intense ultrafast excitations of electrons along the ion path. Structural characterization studies like fluence dependence on strain and composition were carried out. Obtained results from pristine and irradiated samples are compared. Change of strain as a function of ion fluence and electronic energy loss has been observed. AFM images clearly show

the change of surface morphology with irradiation leading to reduction in granular sizes. Significantly, Ag ions at moderate ion fluence have resulted in lower surface roughness from 5 to 3.6 nm, while the reduction in rms roughness is insignificant (4.2 nm) for Ni ions irradiated samples [17]. Nearly lattice matched AlInN/GaN HS upon irradiation, progressively becomes compressively strained. This has been attributed to ion beam mixing effects with the help of thermal spike effects. Increase in strain with increase of Se has been noticed from HRXRD measurements. Eventually, this work demonstrates that ion irradiation can create point defects which affect lattice expansion or compression (reduction). RBS and HRXRD results obtained from pristine and irradiated samples are extensively discussed in results and discussion part.

Chapter VII

Conclusions and future outlook

This thesis presents studies on ion beam processing of materials in general and nitride compounds in particular. The basics of ion solid interactions and their relevance in interpretation of observed effects have been highlighted. It also laid emphasis on how ion beams can be used for engineering strain and band gap in MOCVD grown III-V HS and MQWs. In some cases, radiation induced defects are annealed out by rapid thermal annealing as a function of different annealing temperatures. Significantly, tailoring of band gap of MQWs has been achieved to 40 meV and 70 meV for the irradiated and subsequently annealed samples. Most importantly, defects creation, annihilation and propagation direction, as a function S_e and fluence of irradiating ion beams have been studied. GaN phonon modes corresponding to free charge carriers and strain as a function of S_e are investigated with micro Raman measurements. Incidentally, moderate S_e ions irradiation improved interface quality. In MOCVD grown GaN, YL and BL emissions upon irradiation have been noticed besides band to band transitions. Defect densities calculated from W-H plots for pristine and irradiated samples are compared. It is observed that defect densities increases with increase of S_e. Finally, we conclude that during MeV ion bombardment, the defect densities, strain, band gap, surface morphology strongly depend on ion beam parameters. Improved interface quality of AlGaN/GaN MQWs have been observed for moderate S_e. However, a significant rupturing of bonds at

the interfaces has resulted in mixing effects as evident from TEM analysis for beyond critical S_e. The results obtained from HRXRD and TEM are found to be consistent. More interestingly, initially strained AlInN/GaN HS have been strained further by ion bombardment. Finally, Ion beam induced intermixing effects have been discussed from RBS and HRXRD measurements.

The interesting results obtained in the current investigations have opened several directions which should be pursued in future. For example, quantification of point defect concentration in ion beam treated semiconductors like GaAs and GaN using coherent acoustic phonon interferometry and related techniques will be interesting. Another interesting subject is to enhance the optical properties of GaN with ion beams by reducing YL and BL emission related defects. Optical responses to local defect concentration as a function of ion beam parameters and subsequent annealing temperatures are other areas which could be investigated.

References:

1. M Y Fan, Radiation Effects in Semiconductors, Ref. 2, p.411

2. J W McKay and E E Klontz, Radiation Effects in Semiconductors, Ref 2.p.41.

3. J W McKay, E E Klontz, and G W Goveli , Phys. Rev. Lett. 2, 164 (1959)

4. P. Stampfli, Nucl. Instrum. Methods. Phys. Res. B 107, 138 (1996)

5. M Toulemonde, C Dufour, and E Paumier, Phys. Rev. B 46, 14362 (1992).

6. L. Fleischer, P. B. Price, and R. M. Walker, J. Appl. Phys. 36, 3645 (1965).

7. A. Kamarou, W. Wesch, E. Wendler, and S. Klaumünzer, Nucl. Instr. and Meth. B 225, 129 (2004).

8. W. Wesch, A. Kamarou, and E. Wendler, Nucl. Instr. and Meth. B 225, 111 (2004)

9. E. M. Bringa and R. E. Johnson, Phys. Rev. Lett. 88, 165501 (2002).

10. G. Schiwietz, K. Czerski, M. Roth, F. Staufenbiel, and P. L. Grande, Nucl. Instr. and Meth. B 226, 683 (2004).

11. S. Klaumünzer, *Ion Beam Science: Solved and Unsolved Problems*, The Royal Danish Academy of Sciences and Letters,Copenhagen, p. 293, (2006)

12. G. Devaraju , S. Dhamodaran, A.P. Pathak , G. Sai Saravanan, J. Gaca, M. Wojcik, A. Turos, S.A. Khan , D.K. Avasthi , B.M. Arora , Nucl. Instr. and Meth. B, 266, 3552 (2008)

13. G. Devaraju , A.P. Pathak , N. Srinivasa Rao , V. Saikiran , Francesco Enrichi , Enrico Trave , Nucl. Instr. and Meth. B, 269, 1925 (2011)

14. G. Devaraju , A.P. Pathak , N. Sathish , N. Srinivasa Rao , V. Saikiran and A.I. Titov, Nucl. Instr. and Meth. B 269, 890 (2011)

15. G. Devaraju, N. Sathish, A.P. Pathak , A. Turos , M. Bazzan , E. Trave , P. Mazzoldi , B.M. Arora, Nucl. Instr. and Meth. B, 268, 3001 (2010)

16. G Devaraju, A P Pathak, et al. (Accepted for publication in Radiation Effects and Defects in Solids)

17. G Devaraju, A P Pathak , et al. (accepted for MRS proceeding 2011)

Introduction

1.1 Motivation

III- V compound semiconductors are a novel class of materials for optoelectronics & high power, high temperature device applications. In spite of huge defect densities [1] these materials show excellent luminescence and electrical properties for device applications such as Blue Light Emitting Diodes (LEDs) to violet laser diodes (LDs) , UV photo detectors and High Electron Mobility Transistors (HEMTs). Also, these materials are the best candidates for microwave electronics for base stations of cell phones. AlGaN/GaN hetero structures (HS) also have numerous optoelectronic applications including semiconductor photodiodes. Among family of nitrides, the $Al_{(1-x)}$ In_xN alloys are least investigated compared to $In_x Ga_{(1-x)}$N and $Al_x Ga_{(1-x)}$N due to significant difference of thermal stability between InN and AlN [2–4]. However, $Al_{(1-x)}In_x$N is a promising candidate in Bragg reflectors and field effect transistors [5-6] and hence deserves to be investigated in greater details.

Due to their technological importance in satellite communications, there is a need to understand how device performance degrades under radiation treatment. Much has not been explored but it is observed that high-energy ions create carrier traps which compromise electrical and optical properties [7, 8]. Hence there is a great demand to understand the irradiated III-V compound semiconductor, specially their interfaces, strain vs defects and surface morphology.

Fast moving heavy ions while traversing target material deposit energy to target electrons by inelastic collision processes and create defects into the quantum well active region, which allows atomic diffusion and defect migration to take place between the quantum wells and barriers [9,10]. Effects of defects on charged particle propagation in crystalline solids are also important in this context [11]. In some cases, Swift heavy ion (SHI) irradiation induced damage annihilation has also been reported in InP and GaAs [12,13]. Recently, we have demonstrated strain modification using SHI in lattice-matched and strain relaxed GaAs hetero structures and Multi quantum wells [14]. The possibility of material reconstruction and interface smoothening has also been demonstrated using SHI. In detail, S O Kucheyev el.al, [15] have studied, the MeV ion impact on GaN, AlN,

AlGaN and InGaN HS. But the weakening of chemical bonds due ion-solid interactions in matter is not yet completely understood [16-18].

Moreover, in spite of recent research, basic understanding of SHI induced effects in III- V compound semiconductors is far from mature. In this thesis, significant emphasis has been laid towards understanding the defects creation and annihilation as well as strain and band gap engineering in GaAs and GaN HS and MQWs. We have attempted to address some of the pertinent questions related to critical radiation damage and its effects on free carrier concentrations in HS and MQWs. Similarly, the composition gradient (leading to atomic diffusions) at the interfaces in AlGaN/GaN MQWs, and lattice swelling in bulk GaN as a function of ion velocity dependant studies are important. These motivated us to completely comprehend Swift heavy ion irradiation induced effects in III-V based semiconductors as a function of projectile velocity, mass and its critical fluence.

1.2. Ion - solid interactions

Ion beams not only introduces the modification, but are also used as an essential tool for material analysis. Ion propagation in solids creates radiation damage by means of energy loss and charge exchange process. When an energetic ion moves through the material, ion loses energy by depositing its energy either to target electrons or to the target nucleus. The types of emissions which can result from both nuclear and electronic collisions are illustrated in Fig 1.1, Emitted and ejected particles or electromagnetic radiation upon ion bombardment gives information on the near-surface composition and structure. The most important ion beam analysis methods are listed in Table 1.1 along with selected references which provide details of each technique.

At high projectile velocities even the innermost electrons of projectile are stripped off and essentially bare nucleus moves in solid. As the energetic ions move in matter and lose their energy via different process, corresponding Ion velocity decreases by various means. As the projectile velocity approaches successively the velocities of its inner orbital electrons, the probability of capturing electrons in the corresponding shells increases, whereas probability of losing electrons from projectile decreases.

At these high velocities, these ions in materials create columnar defects [19] and cylindrical tracks [20] resulting in amorphization [21] and recrystallizations [22]. Finally,

at low velocities below ($v_0Z_1^{2/3}$), essentially a neutral projectile atom moves in the solid. In this low velocity region, the probability of projectile interaction with target atom/nucleus is very high compared to target electrons.
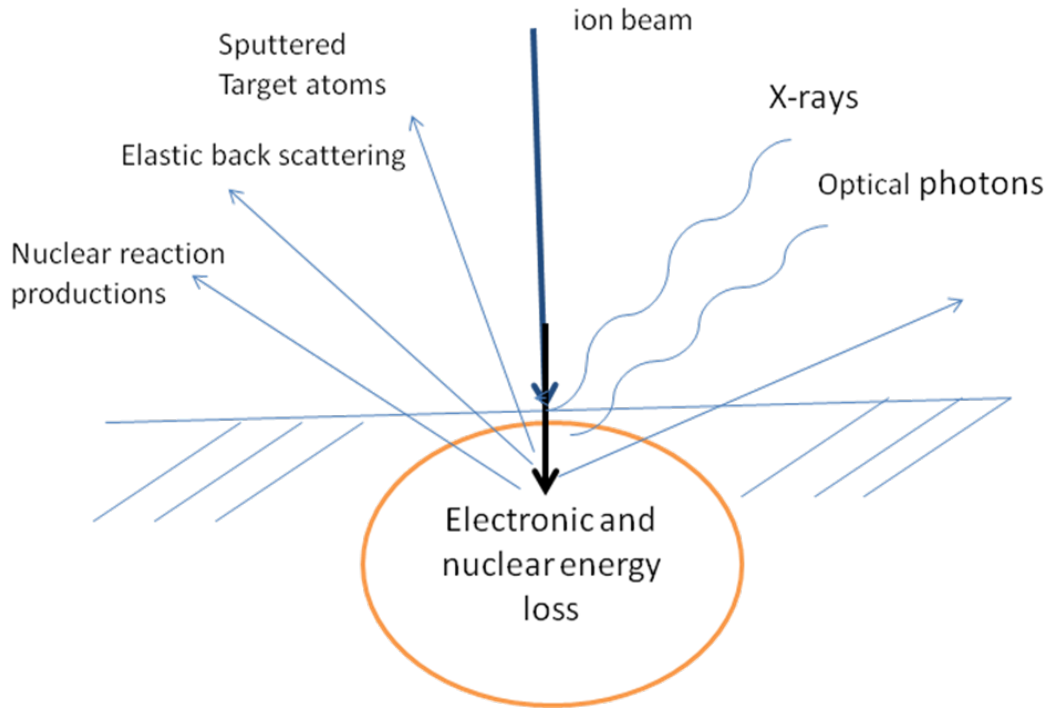
Fig.1.1 Basic ion-solid interaction process

At the end of the ion range, projectile interaction with the target atoms leads to dislodging those atoms from regular lattice sites. Depending on energy loss (dE/dx), these processes are classified as i) Electronic energy loss (S_e) and ii) Nuclear energy loss (S_n). As an example, energy loss as a function of projectile energy and depth in GaN are shown in Fig 1.2 a) and b).

1.2.1 Electronic Energy loss (S_e)

It is prominent at velocities much greater than the speed of electrons (for $v \gg v_0Z_1^{2/3}$) in their outer most orbits. At these velocities, charge Z_1e interacts elastically (inelastically) with free electrons (bound electrons) in the target.

$$\frac{d\sigma}{dT} = \frac{-\pi}{E_0} \frac{M}{m} \left(\frac{Ze^2}{4\pi\varepsilon_0} \right)^2 \frac{1}{T^2} \qquad (1.1)$$

11

Where M is the projectile mass, m_e is electron mass and T is kinetic energy of projectile. A difficulty in evaluating the stopping cross section arises from the fact that $d\sigma \sim (T)^{-2}$, so that the integral diverges with a lower limit $T \to 0$. Therefore, a lower limit T_{min} has to be introduced corresponding to a maximum impact parameter b_{max}. An estimation of b_{max} is obtained by the so-called "adiabatic cutoff ".

Table.1.1 Material analysis from Ion beam induced emission process

Emission Process	Analysis methods	Key references
Incident ion scattering	Low energy ion scattering Ion surface scattering Rutherford scattering	Heiland and Taglauer (1973) Buck and Poate (1974) Chu et a1 (1978)
Sputtered target atoms	Secondary ion mass spectroscopy Auger electron spectroscopy	Wittmaack (1980) Kirsher and Etzkorn (1979)
Nuclear reaction process	Ion induced gamma rays Nuclear reaction analysis Resonant nuclear process	Mayer and Rimini (1977) Bird (1980) Langley et al (1974)
X- rays	Proton induced X rays Heavy ion induced X rays	Folkmann (1975) Heitz et al (1978)
Optical photons	Ion beam sputtering for chemical analysis	Tolk et al (1977)
Electrons	Ion induced Auger secondary electron emission	Thomas et a1 (1980) Hasselkamp et a1 (1980) MacDonald et a1 (1983)
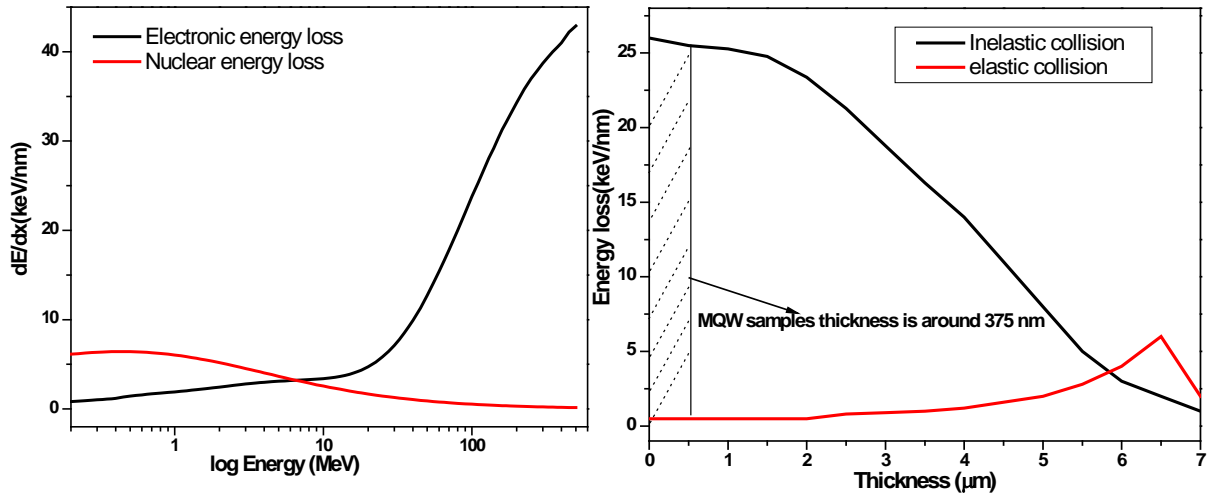
Fig 1.2 a) Variation of dE/dx of Au ions in GaN, b) Plots of S_e and S_n as a function of depth from surface of GaN for 120 MeV Au ions

Assuming a characteristic time interval τ of the interaction, the electrons of a target atom contribute to energy loss only if their mean orbital frequency ω is small compared to the

inverse of the characteristic collision time. Otherwise, at large orbital frequencies, the electron would attach adiabatically to the moving ion. Using the momentum approximation, the characteristic collision time can be estimated from the transverse momentum transfer and its associated force integral so that the integration is limited to a maximum impact parameter (b_{max}).

$$-\frac{dE}{dx} = N.Z_2 \int T.\frac{d\sigma}{dT} dT \tag{1.2}$$

$$-\frac{dE}{dx}\bigg|_{el} = N.Z_2.\pi.\left(\frac{Z_1 e^2}{4\pi\varepsilon_0}\right)^2 . \frac{2M}{m.E_0} . \ln\left(\frac{2\,b_{max}}{r_{min}}\right) \tag{1.3}$$

Where b_{max} is replaced by Ionization potential (I), $= \dfrac{2}{mv^2}\left(\dfrac{Z_1 e^2}{4\pi\varepsilon_0}\right)^2 \dfrac{1}{b_{max}^2}$ and r_{min}

$$= \frac{2Z_1 e^2}{4\pi\varepsilon_0 mv^2}$$

Then, the result becomes (the classical "Bohr" formula).

$$-\frac{dE}{dx}\bigg|_{el} = \frac{NZ_2 Z_1^2 e^4}{4\pi\varepsilon_0^2} \frac{1}{2m_e v^2} . \ln\left(\frac{2m_e v^2}{I}\right) \tag{1.4}$$

In the classical picture, the energy dependence of the electronic stopping reads as $\sim E^{-1} \ln(CE^{3/2})$, C being a constant.

Calculating the scattering cross section in Born approximation (includes intra atom excitations) gives the Bethe formula

$$-\frac{dE}{dx}\bigg|_{el} = \frac{NZ_2 Z_1^2 e^4}{4\pi\varepsilon_0^2} \frac{1}{m_e v^2} . \ln\left(\frac{2m_e v^2}{I}\right) \tag{1.5}$$

According to Bloch, a reasonable approximation for $I \approx I_0 Z_2$ with $I_0 = 10$ eV

Bethe- Bloch has given electronic stopping power for relativistic velocities,

$$-\frac{dE}{dx}\bigg|_{el} = \frac{NZ_2 Z_1^2 e^4}{4\pi\varepsilon_0^2} \frac{1}{m_e \beta^2 c^2} . \left[\ln\left(\frac{2m_e \beta^2 c^2 \gamma^2}{I}\right) - \beta^2\right] \tag{1.6}$$

Where v = βc

Assuming further approximations, Fano [23] described a relativistic version of Bethe-Bloch energy loss formula where two additional corrective terms are included, the shell correction term C/Z_2 and the density effect correction term $\delta/2$ and it is given as,

$$S = \frac{4\pi e^4 Z_1^2 NZ_2}{m_e v^2}\left[\ln\left(\frac{2m_e v^2}{\bar{I}}\right) - \ln\left(1-\beta^2\right) - \beta^2 - \frac{C}{Z_2} - \frac{\delta}{2}\right] \tag{1.7}$$

which is simplified using the definitions,

$$r_o \equiv e^2\big/mc \qquad \text{(the Bohr electron radius)}$$

$$f(\beta) \equiv \ln\left[\frac{2mc^2\beta^2}{1-\beta^2}\right] - \beta^2 \tag{1.8}$$

$$S = \frac{4\pi r_0^2 m_e c^2 Z_1^2 NZ_2}{\beta^2}\left[f(\beta) - \ln <I> - \frac{C}{Z_2} - \frac{\delta}{2}\right] \tag{1.9}$$

There have been many corrections proposed to improve on Fano's theoretical approximations. Traditionally, this is done by expanding this equation in powers of Z_1, which can be used to add additional corrections to the ion and target interaction.

1.2.2 Nuclear Energy loss (S_n)

At low velocities, an additional energy loss process occurs. In this regime, energy of ion is transferred from nucleus of projectile to target nucleus by electrostatic interaction (elastic collision) between the screened charges of the two nuclei. As suggested by Bohr and later developed by Lindhard et al, S_n becomes another major component of energy loss at low energies, especially for heavy projectile atoms. Nuclear energy loss has two regimes, displacement followed by replacement collisions. At the entrance of surface the ions dislodge atoms from lattice site and the number of displaced atoms can be calculated using well known Kinchin- Pease formula. Replacement collision occurs at the end of the ion range where the collision cascades are dominant. Damage profile of GaN is quantified using Transport of Ions in matter (TRIM) calculation by taking effective displacement energy (E_d) for Ga and N sub lattices as 25 eV.

1.2.3 Effective charge

The average charge of the ion, which depends on its velocity, is denoted as "effective" charge, Z_{1eff},. Most importantly, when ions of arbitrary charge state are impinging on a solid surface, the actual charge state of ions in matter continuously fluctuates and is determined by the net difference of electron loss and electron capture. At high velocities, electron loss dominates, so that the ions become a bare nucleus with $Z_{1eff} = Z_1$ at sufficiently high energy. In low energy regime atomic electrons interact with the electrons of the solid and then ion becomes almost neutral by vanishing effective charge. Quantitatively, if the ion velocity is lower than the characteristic orbital velocity of its target atomic electrons then electron attachment to the projectile is effective. Under these conditions, electrons from the electron gas of the solid have sufficient time to adjust with the moving ion. At the end of range, ion velocities are very low which starts interacting with target atoms thereby dislodging atoms from regular lattice sites.

1.3 Consequent/ competing process

Thermal spike: SHI irradiation is known for depositions of high density of energy to electrons along the ion path within very short intervals of time. According to the thermal spike model [24] during the passage of swift heavy ions, the kinetic energy of the electrons is transported to target lattices via electron- electron or electron-phonon interaction causing sufficient increase of local lattice temperature above the melting point of the material. The temperature increase is followed by a thermal quenching at an extremely high quenching rate 10^{11}–10^{14} K s^{-1}. At these quenching rates, pre existing defects in semiconductors can be annealed out.

Coulomb explosion: In this case, an incident energetic ion excites the electron cloud producing charge separation along its path through the solid which results in repulsion between the transiently ionized atoms in the solid causing "Coulomb explosion"[25]. Such transiently ionized region produced by an incident ion is known as an "ionization track" which can produce craters [26] and sputtering [27–29], as well as damage tracks in solids [30,31]. Coulomb explosion model and the thermal spike model are used to describe defect production in insulators and semiconductors [32]. It is somewhat remarkable since Coulomb explosion is a mechanism for coupling of the electronic excitation energy into atomic motion, whereas a thermal spike model describes the

transport of energy out of a heated region. Mostly, Thermal spike model is used to interpret the observed effects in semiconductors and Coulomb explosion model is being used to explain the observed effects in insulators. However, it is observed that these interaction processes compete with each other in all the materials. Even in insulators, with in short intervals of time and few nms after entering the target, enough electrons are generated to screen out the projectile charge resulting in transition from coulomb explosion to thermal spike situation.

1.4 Introduction to III-V compound semiconductors

1.4.1 III-V compound semiconductors

III-V compound semiconductors are extensively studied due to their technological advantage in optoelectronic devices. Among III-V compound semiconductors, $In_xGa_{1-x}As/InP$ heterostructures are extensively investigated due to the possibility of both compressive and tensile strain depending on the composition. These materials exhibit zinc-blende structure where the two FCC sublattices are chemically distinct. Generally, this is the crystal structure for III–V semiconductor compounds. In this case, the each Ga atom would be on one FCC sublattice (ions) is surrounded by four As atoms which would be on other FCC sublattice and vice versa, in a tetrahedral geometry as shown in Fig.1.3.
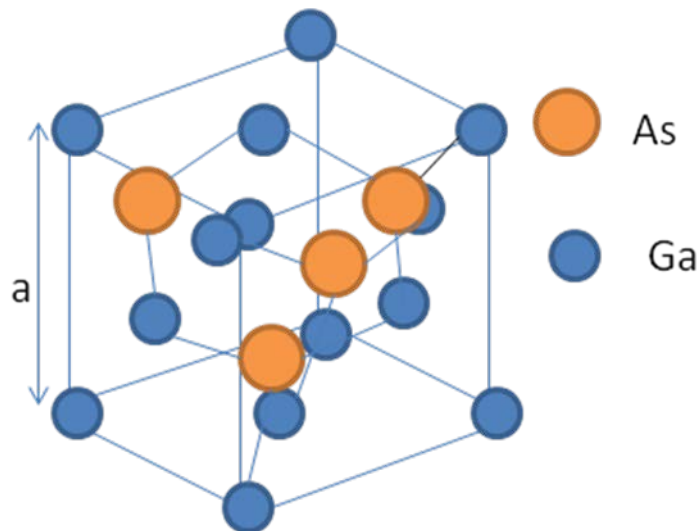
Fig.1.3 Zinc Blende crystal structure consists of two interpenetrating FCC lattices, one displaced from the other by a distance (a/4,a/4,a/4) along the body diagonal. The position of two atoms is (000) and (a/4,a/4,a/4).

More importantly, band gap as a function of lattice parameter has been achieved with change in composition of ternary alloy as shown in Fig.1.4. Observed lattice constants for GaAs and InP at room temperature are a = 5.653 Å and 5.868 Å, respectively.
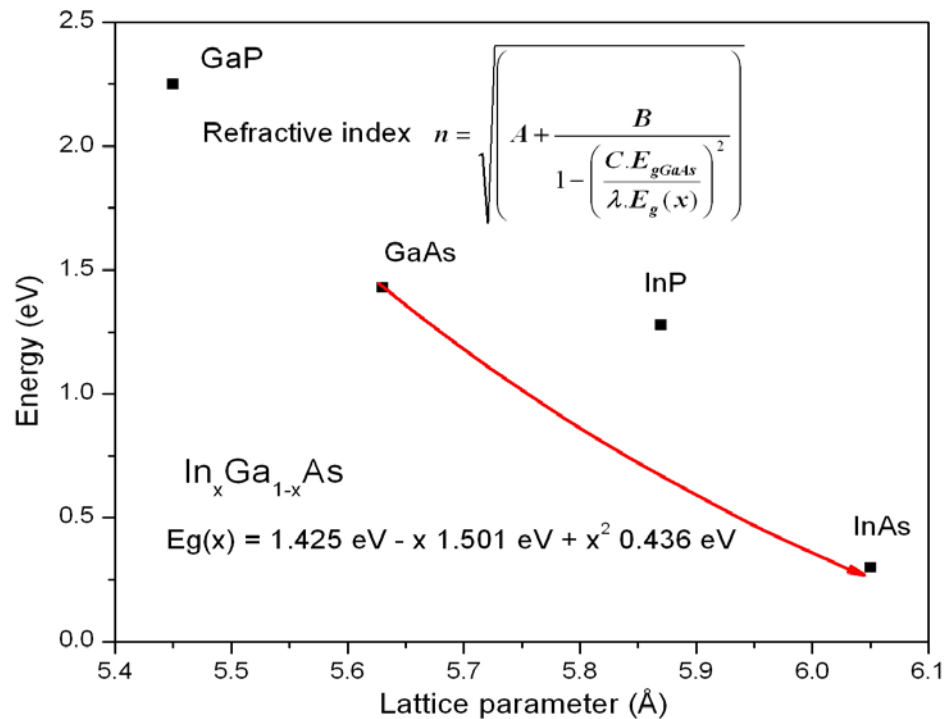
Fig.1.4: Bandgap as a function of lattice parameter for the most common III-V ternary alloys

1.4.2 III-Nitrides

III- nitrides (GaN, AlGaN and AlInN) have attracted many researchers due to their technological applications. Currently, these materials are being used for light emitting diodes (LED), laser diodes, UV detectors and ultra high power switches despite being highly defective. Some of the unique properties of III nitrides, essential for opto-electronic device applications, are discussed below.

Family of III- nitrides are wide direct band gap semiconductors, crystallizes either in hexagonal closed packed (hcp) or cubic zinc blende structures. Generally, the wurtzite structure is found to be most stable than the cubic zinc blende structure. The wurtzite structure consists of two inter penetrating hcp sub lattices, each with one type of atom, offset along the c-axis by 5/8 of the cell height (5c/8). The wurtzite and zinc blende

structures are somewhat similar and yet different. The differences between these structures are stacking sequence of closest packed diatomic planes and bond angles of second nearest neighbors. The primitive cell of wurtzite has $a_1=a_2$ with an included angle of 120° as shown in Fig 1.5. The c axis is normal to the plane of a_1 and a_2. Here, one atom of the basis is at the origin (0,0,0); the other Ga atom is at (2/3,1/3,1/2) and nitrogen at (0,0,3/8) and(2/3,1/3,7/8) of unit cell.
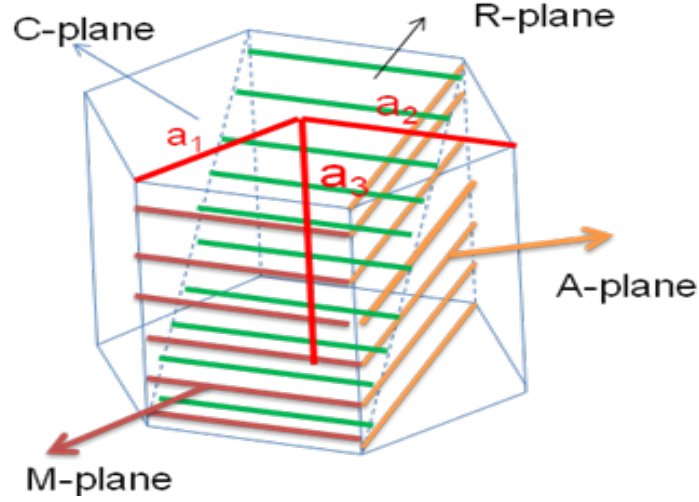
Fig 1.5 Wurtzite structures with polar and non polar planes

Observed lattice constants for GaN at room temperature are c = 3.189 Å and a = 5.185 Å [33]. For zinc blende structure, lattice constant is observed to lie between 4.49- 4.55 Å [34,35]. These materials exhibit partly covalent and partly ionic due to difference in their electro negativity values. Most importantly, different atoms occupy on different planes with deviation of c/a from ideal values of hcp structures. The hcp structure lacks space inversion symmetry as a result spontaneous polarization (P_{SP}) is observed [36]. The P_{SP} values and their corresponding c/a values for AlN, GaN and InN are given in Table 1.2. Besides P_{SP}, these materials also show piezo-electric polarization (P_{PE}) due to lattice and thermal mismatch between substrate and epi layers. P_{PE} dependence on strain is given by

$$P_{PE} = 2\left(\frac{a_{sub} - a_{epi}}{a_{epi}}\right)\left(e_{31} - e_{33}\frac{C_{13}}{C_{33}}\right) \qquad (1.10)$$

where e is piezo electric coefficients, C is elastic coefficients; a_{sub} is substrate lattice constant and a_{epi} is epilayer lattice constant. Thus, a charge sheet at the interface of hetero structures is the cause of strain.

Table1.2 P_{sp} and c/a values for AlN, GaN and InN semiconductors

Material	AlN	GaN	InN
c/a	1.6	1.626	1.613
$P_{sp}(C/m^2)$	-0.081	-0.029	-0.032
Band gap (eV)	6.2 (D)	3.42 (D)	0.7 (D)
Lattice constants (Å)	a = 3.112 c = 4.979	a = 3.189 c = 5.185	a = 3.548 c = 5.760
Fractional Ionic character (FIC)	0.72	0.51	0.54
Thermal conductivity (W cm^{-1}K^{-1})	2.85	11.9	0.8

As such, polarization charge affects the device operation in all nitrides based devices, particularly heterojunction field effect transistors (HFETs), and thus must be taken into consideration before realizing device structures. Moreover, these polarizations eventually affect the band diagram of hetero structures. It is therefore imperative to consider strain effects in III – nitrides. Electronic energy-band structure of GaN shows direct band gap at Γ point in the Brillouin zone [37]. The lowest conduction band in GaN is non degenerate, but crystal field, the spin-orbit interactions and strain lift the degeneracy of heavy and light holes in valance band [38]. Strain in Wz-HS is imperative that affect the properties of hetero structures. The advantages of strain in electronic and optoelectronic devices of ZB crystals have been studied [39].
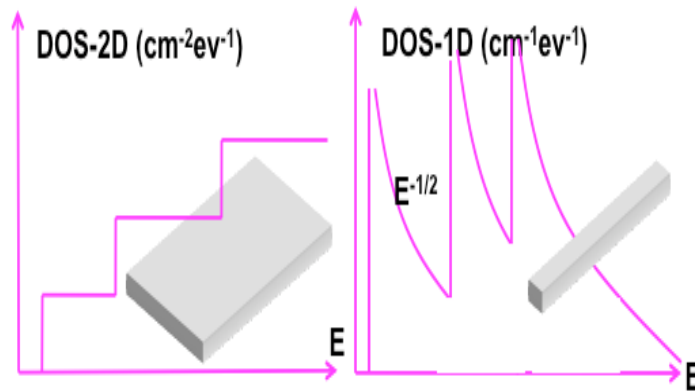
Fig1. 6 Density of states for 2D and 1D systems
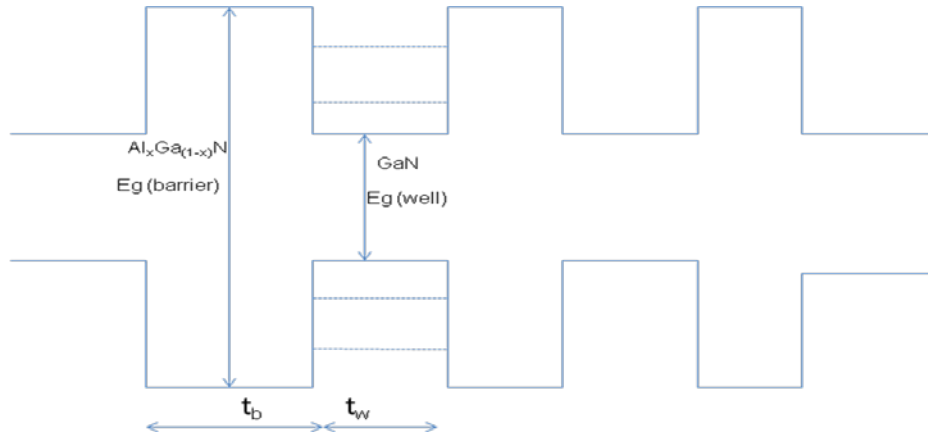
Fig 1.7 Schematic representation of AlGaN/GaN multi quantum well at gamma point

Advancement in growth techniques allows different structures with one, two and three dimensional confinements. In one dimensional confinement, the component of wave vector is quantized along the growth direction. In plane components of wave vectors are not quantized and usual energy momentum relation would apply.

Corresponding E-K diagram in two dimensional systems with confinement along Z-direction for quantum energy levels is shown in Fig 1.6. Due to confinement, density of states in both valance and conduction band are discretized. Quantum wells are those semiconductors having same crystal structure with low band gap material in between high band gap materials. Such sequence of quantum wells without and with strong overlap of wave functions corresponding to periodic quantum wells are called Multi quantum wells (MQWs) and Super lattices (SL) (see Fig 1.7), respectively.

Moreover, it is observed that quantum wells get deeper for compressive strain and shallower for tensile strain. The density of states at the valence band maximum gets smaller for compressive and larger for tensile strain. Ion beams are proven to be best tool in altering density of states, strain and band gap. Thus, critical understandings on lower dimensional structures are essential for solid state lasers and quantum infrared photo detectors.

1.5 Basics of characterization techniques

Following are some of the most suitable techniques for characterizing hetero structures and multi quantum wells are as follows

1. High resolution X-ray diffraction

2 . Raman Spectroscopy

3. Rutherford backscattering spectrometry

4. Atomic force microscopy

5. Transmission electron microscopy

6. Photoluminescence

We have used these techniques for characterizing our samples. Some basics of above techniques are discussed below.

1.5.1 High Resolution X-ray diffraction (HRXRD)

This technique is a non invasive technique and essentially used for structural investigations such as nature of strain, lattice parameters with high precision, tilt and twist angles and defect densities. When a monochromatic X-rays of suitable wavelength impinges on sample surface, it undergoes scattering from large number of atoms. In this process, energy is being transferred to an electron while traversing materials without letting loose of electrons from atoms. Finally, elastically scattered X-rays by electrons is observed as Thomson scattering. In this process the electron oscillates like a Hertz dipole at the frequency of the incoming beam and becomes a source of dipole radiation. Since atoms are arranged periodically on lattice points, the scattered rays then have definite phase relations between them. These phase relations are such that destructive interference occurs in most directions of scattering, but in a few directions constructive interference takes place and then diffraction spots are formed. The crystal acts as a diffraction grating and array of diffraction maxima can be investigated. Diffraction spot positions and shapes are inversely related to the inter planar spacing and size of the crystals (mosaic blocks). Thus, the crystal planes are associated with real space and the diffraction spots with reciprocal space.

The Bragg law is derived based on the following geometrical facts

(1) The incident beam, surface normal, and the diffracted beam are always coplanar.

(2) The diffraction angle should be always 2θ which is an angle between diffracted and the transmitted beam.   It is this angle, rather than θ, which is usually measured experimentally.

Diffraction in general occurs (as shown in Fig 1.8) only when the wavelength of the wave motion is of the same order of magnitude as inter planar spacing, this requirements follows from Bragg equation,

$$2d_{hkl}\,Sin\,\theta = n\lambda \tag{1.11}$$

where d_{hkl} is inter planar spacing, θ is Bragg angle and λ is X-ray wavelength. For diffraction, the smallest value of n is 1 and n =0 cannot be observed. Therefore the condition for diffraction at any observable angle 2θ is λ < 2 d_{hkl} . In particular, the measurement of the full width at half maximum (FWHM) of the rocking curve has been used for probing GaN epitaxial quality. In general, the broadening of the XRD curve is affected by the dislocation structure.
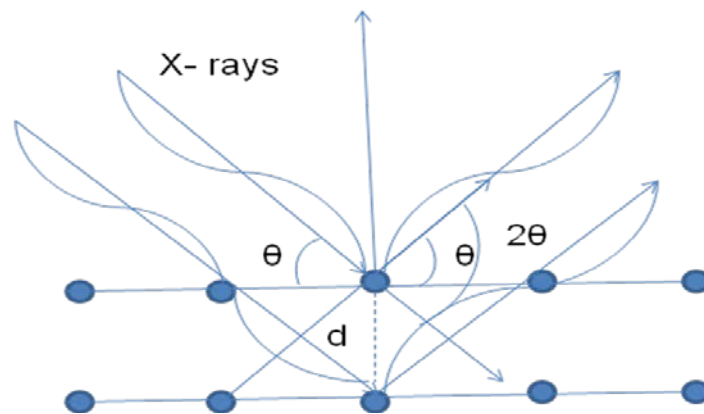
Fig 1.8 Visualization of the Bragg equation. Maximum scattered intensity is only observed when the phase shifts add to a multiple of the incident wavelength λ.

Moreover, other additional structural imperfections like heterogeneous strain, small correlation lengths, impurities and instrumental broadening   influence the diffraction pattern. The heterogeneous strain, the correlation lengths normal and parallel to the substrate surface and the degree of mosaicity are expressed by the tilt and twist angles

which are key issues in characterizing the quality of epitaxial films with a large lattice mismatch to the substrate.

The density of screw dislocations N $_{[0001]}$ can be obtained from the expression [40]

$$N_{[0001]} = \left(\frac{(\alpha)^2}{4.35 \times (b)^2} \right) \tag{1.12}$$

Where, α is the value of tilt angle and b is Burgers vector's magnitude (0.5185 nm). Thus, the defect densities are calculated using (1.12).

1.5.2 Raman Spectroscopy

It is a non destructive method used for determining the lattice dynamics, carrier concentration, structural disorder, composition and strain in III-V compound semiconductors. When a photon interacts with a molecule, the electric field induces a dipole moment; $\vec{P} = \overline{\overline{\alpha}}.\vec{E}$, where $\overline{\overline{\alpha}}$ is a polarizability tensor of the molecule and is a measure of the ease with which the electron cloud around a molecule can be distorted. The polarizability tensor has frequency dependent contributions at the molecular vibration frequencies; ($\omega - \omega_v$) is Stokes component and the ($\omega + \omega_v$) is anti-Stokes component where ω is incident frequency and ω_v is vibrational frequency. A vibrational mode is Raman active if the direct product contains the irreducible representation for symmetric final states. This is the basic selection rule for Raman activity. The process involves an electron–photon interaction to produce an excited state where an electron–phonon scattering event occurs by creating (Stokes process) or absorbing (anti-Stokes process) a phonon or emitting same incident radiation (Rayleigh scattering), and finally the scattered photon is emitted. Stokes scattering can always occurs because the intensity of stokes are high compared to anti-stokes.

GaN has a hexagonal wurtzite structure and belongs to C_{6v} space group. Group theory predicts that there are two A_1, two E_1, two E_2 and two B_2 modes. Among them one E_1, one A_1 and two E_2 modes are Raman active. An A_1 branch in which the phonon polarization is in the Z- direction (the c axis of the crystal is taken to be the Z- axis), an E_1 branch in which the phonon is polarized in the XY plane, and two E_2 branches. The E_1 branch is linearly polarized, but the two E_2 branches do not have a simple polarization behavior. A_1 and E_1 branches are polar with different energies for the longitudinal LO

and transverse TO components. In the backscattering geometry, with the c-axis normal to the surface, the TO branch of the A_1 mode and the TO and LO branches of the E_1 mode are forbidden. The LO branch of the A_1 mode and E_2 models are allowed. The $E_2(H)$ mode of GaN is very sensitive to biaxial strain in the c-plane and this mode gives the strongest signal in the spectra. Due to its non polar nature, E_2 mode is widely used to quantify stress in III- nitrides [41,42]. $A_1(LO)$ mode, in wurtzite GaN , are sensitive to lattice vibrations along the plane perpendicular to (0001). This mode depends not only on the residual stress in GaN film but also on the coupling to free carriers (plasmon) of LO mode [43]. Variation of line shape signifies the coupling of this mode with over damped plasmon.

1.5.3 Rutherford Backscattering Spectrometry (RBS)

It is a versatile technique to find the thickness and composition of composite materials. In RBS, a light ion of given energy incident on sample surface, lose energy by elastic collision with target atoms.The ions scattered in backward direction are detected to obtain elemental composition and thickness. The energy of the projectile after collision can be related to its energy before collision by means of kinematic factor. As the ion penetrates through the scattering medium, it loses energy which is directly proportional to the thickness of material, so a depth scale can be assigned directly and quantitatively to kinematic factor. If ions of mass M_1 and known energy E_0 are directed on sample containing an element of unkown mass M_2, by measuring the energy of ions scattered at an angle, the unknown mass can be determined as shown in Fig. 1.9.
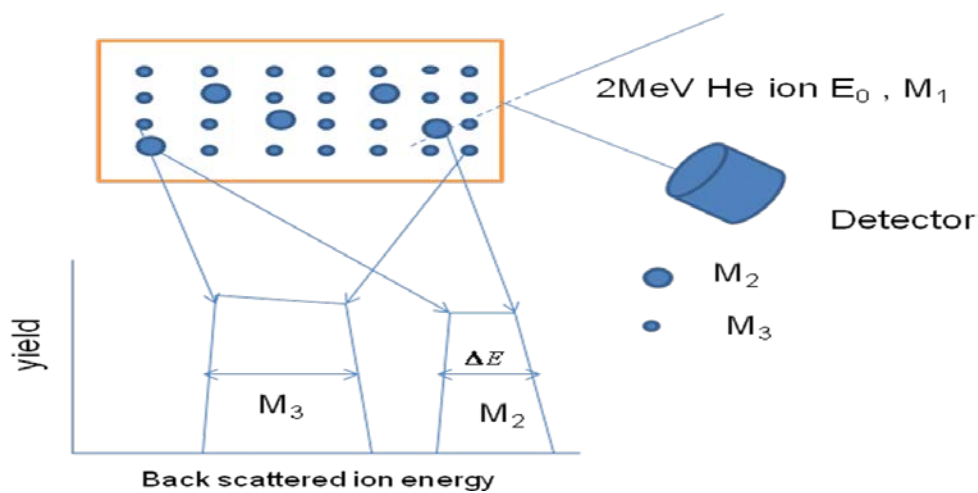
Fig.1.9 Schematic diagram of illustrating backscattering spectrum of Ions of mass M_1 impinging on a thin film containing different masses M_2 and M_3.

The yield of backscattered particles is proportional to the scattering cross-section so the composition depth profile can be found from knowledge of energy loss and cross sections. The significant functional dependencies of differential cross section are as follows.

1. It is proportional to Z_1^2 . The backscattering yield obtained from a given target atom with a He beam is four times as large as with proton beam.

2. It is proportional to Z_2^2 . For a given projectile, heavy target atoms are much more efficient scatterers than light atoms. Therefore, backscattering spectrometry is very sensitive to heavy elements

3. It is inversely proportional to square of projectile energy. Yield increases as energy decreases.

4. It is inversely proportional to fourth power of scattering angle. This gives rapidly increasing yields as the scattering angle is reduced.

1.5.4 Atomic Force Microscopy (AFM)

Atomic force microscopy is a technique for understanding surface morphology. AFM can be used to study insulators and semiconductors as well as electrical conductors. In atomic force microscopy, the most commonly associated force is an inter atomic force called the van der Waals force. As the tip of the cantilever approaches closer to the sample surface either cantilever bends or deflects. A detector measures the cantilever deflection as the tip is scanned over the sample, or the sample is scanned under the tip. The measured cantilever deflections allow a computer to generate a map of surface topography. As shown in Fig.1.10, The dependence of the van der Waals force upon the distance between the tip and sample gives two distinct modes: 1) the contact mode; and 2) the non-contact mode. In the contact mode, the cantilever is held less than a few angstroms from the sample surface, and an inter atomic force between the cantilever and the sample is repulsive. In the non-contact mode, the cantilever is held on the order of tens to hundreds

of angstroms from the sample surface, and an inter atomic force between the cantilever and sample is attractive (largely a result of the long-range van der Waals interactions). Mostly, for MOCVD grown semiconductors, contact mode is being used to investigate the surface morphology.
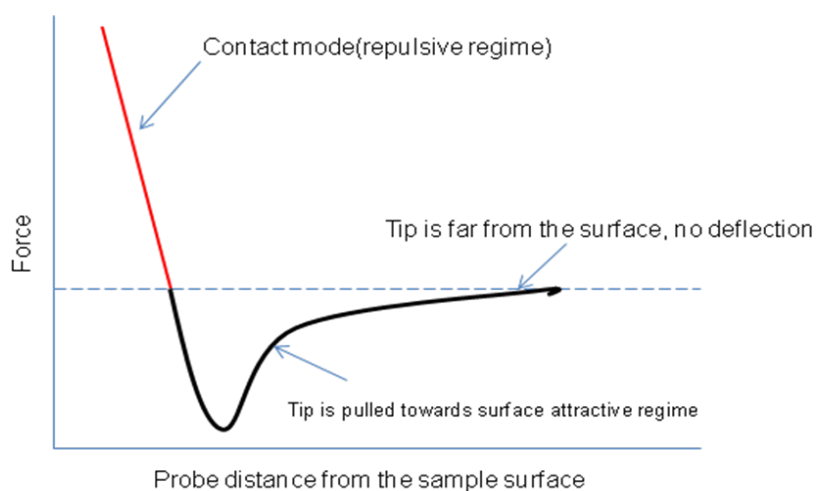
Fig.1.10 Force vs distance curve for different regimes used for AFM

1.5.5 Transmission Electron Microscopy (TEM)

The Transmission electron microscopy (TEM) allows imaging the crystal structure at atomic scale resolution. Samples for the TEM must be specially prepared to thicknesses that allow electrons to be transmitted through the sample. Since the wavelength of electrons is much smaller than that of light, the resolution attainable for TEM is many orders of magnitude higher than that of a light microscope. Thus, TEM can reveal the finest details of internal structure in some cases it can show as small as individual atoms. Under optimal conditions, atomic scale imaging along with chemical composition can be determined. Because of the high spatial resolution, TEM is always used for determining the detailed crystallography of thin film materials. In TEM there are two basically different techniques. Nature of crystal and their orientations are verified with selected area electron diffraction (SAED).

In conventional TEM, the specimen is illuminated by near parallel beam of electrons, and image is formed by sequence of lenses equivalent to optical microscope. In Scanning Transmission electron microscopy (STEM), a fine beam of electrons are focused and scanned across the specimen. Again STEM, offers two different imaging modes. Bright field imaging is based on the low angle scattered electrons, yielding images subject to

phase contrast in similar manner to conventional TEM. But, most conventional imaging mode for STEM is high angle annular dark field (HAADF). The great advantage of this imaging mode is that the incoherent scattering distribution can be understood directly in terms of atomic number. Therefore, HAADF mode is called Z-contrast imaging mode. In this mode defects appear bright due to static random displacements of electrons, and different types of defects are clearly distinguishable.

1.5.6 Photoluminescence (PL)

Photoluminescence (PL) is a result of incident photon absorption which results in the generation of an electron hole pair and emission of photon of different wavelength. Incident photons, when absorbed excite electrons usually from the valence band into conduction band through momentum conserving process. The electrons and holes thermalize to lowest energy states of their respective bands via phonon emission before recombining across the band gap and emit photons of corresponding energies. Effects of Irradiation on radaitive recombination centers are extensively studied using PL.

1.6 Conclusions

In this chapter, the motivation and advantages of current works have been elucidated. Much emphasis is given on the following points: (i) materials of interest (ii) basics of characterization techniques (iii) the consequent/ competing effects by ion beams for material modification. The next chapter describes the experimental facilities utilized for investigating various structural and optical properties.

1.7 References

1. S D Lester, F A Ponce, M G Craford and A Streigerwald, Appl. Phys. Lett. 66,1249 (1995)
2. V G Debuk and A V Vozny, Semiconductors. 39, 623 (2005)
3. S Y Karpov, N Podolskaya, I A Zhmakin, and A I Zhmakin, Phys. Rev. B 70, 235203 (2004)
4. M Ferhat and F Bechstedt, Phys. Rev. B 65, 075213 (2002)
5. R Butte, I F Carlin, E Feltin, M Gonschorek, S Nicolay, G Christmann, D Simeonov, A Catiglia, J Dorsaz, H J Buehlmann, , S. Christopoulos, G.B.H. von Hogersthal,

A.J.D. Grundy, M. Mosca, C Pinquier, M A Py, F Demangeot, J Frandon, P G Lagoudakis, J J Baumberg and N J Grandjean, J. Appl. Phys. D 40, 6328 (2007)

6. A Dadgar, F Schulze, J Blasing, A Diez, A krost, M Neuburger, E Kohn, I Daumiller, and M Kunze, Appl. Phys. Lett. 85, 5400 (2004)

7. W H Weber and R Merlin, Editors, *Raman Scattering in Materials Science*, Springer, Berlin (2000)

8. B D White, M Bataiev, L J Brillson, B K Choi, D M Fleetwood, R D Schrimpf, S T Pantelides, R W Dettmer, W J Schaff, J G Champlain and A K Mishra, IEEE Trans. Nucl. Sci., 49, 2695 (2002)

9. M Toulemonde, C Dufour, and E Paumier, Phys. Rev. B 46, 14362 (1992)

10. L Fleischer, P B Price, and R M Walker, J. Appl. Phys. 36, 3645 (1965)

11. A P Pathak, Radiation Effects, 61,1 (1982)

12. A Kamarou, W Wesch, E Wendler, and S Klaumünzer, Nucl. Inst. and Meth. B 225, 129 (2004)

13. W Wesch, A Kamarou, and E Wendler, Nucl. Inst. and Meth. B 225, 111 (2004)

14. S Dhamodaran, A P Pathak, A Turos, and B M Arora, Nucl. Inst. and Meth. B 266, 1908 (2008)

15. S O Kucheyev, J S Williams and C Jagadish, Vaccum, 73, 93 (2004)

16. E M Bringa and R E Johnson, Phys. Rev. Lett. 88, 165501 (2002)

17. G. Schiwietz, K. Czerski, M. Roth, F. Staufenbiel, and P. L. Grande, Nucl. Inst. and Meth. B 226, 683 (2004)

18. S Klaumünzer, *Ion Beam Science: Solved and Unsolved Problems*, The Royal Danish Academy of Sciences and Letters, Copenhagen, p. 293, (2006)

19. L Civale, A D Marwick, T K Worthington, M A Kirk, J R Thomson, L Krusin-Elbaum, Y Sun, J R Clem and F Holtzberg, Phys. Rev. Lett. 67, 648 (1991)

20. R L Fleischer, P B Price, R M Walker, J. Appl. Phys. 36, 4645 (1965)

21. H Trinkus, Mat. Sc. Forum 248-249, 3 (1997)

22. G S Virdi, B C Pathak, D K Avasthi, D Kanjilal, Nucl. Inst. and Meth. B 187,189 (2002)

23. U Fano, Ann. Rev. Nucl. Sci. 13, 67 (1963)

24. G Szenes, Phys. Rev. B 51, 8026 (1995)

25. R L Fleischer, P B Price, and R M Walker, J. Appl. Phys. 36, 3645 (1965); R. L. Fleischer et al., Phys. Rev. 156, 353 (1967)

26. R M Papaléo, L D de Oliveira, L S Farenzena, M A de Araújo, and R P Livi, Phys. Rev. B 62, 11 273 (2000)

27. R E Johnson and W L Brown, Nucl. Instrum. Methods Phys. Res. 198, 103 (1982)

28. P K Haff, Appl. Phys. Lett. 29, 443 (1976)

29. T Schenkel, A V Hamza, AV Barnes, D H Schneider, J C Banks, and B L Doyle, Phys. Rev. Lett. 81, 2590 (1998)

30. D Lesueur and A Dunlop, Radiat. Eff. Defects Solids 126, 123 (1993); 126, 163 (1993)

31. K Izui, J. Phys. Soc. Jpn. 20, 915 (1965)

32. F Seitz, Discuss. Faraday Soc. 5, 271 (1949)

33. H P Maruska and J Tietjen, Appl. Phys. Lett. 15, 327 (1969)

34. R C Powell, N E Lee, Y W Kim and J E Greene, J. Appl. Phys. 73, 189 (1993)

35. T Lei, M Francuilli, R J Molnar, T J Moustakas, R J Graham and J Scanlon, Appl. Phys. Lett. 59, 944 (1991)

36. K Smith R D, Vanderbilt D , Phys. Rev. B 47 ,1651(1993)

37. S Bloom, G Harbeke, E Meier and I B Ortenburger , Phys. Stat. Sol. (b), 66, 161 (1974)

38. B Monemar, J P Bergman and I A Buyanova, GaN and Related Materials, (Edited by Pearton, S. J.), pp. 85 – 140, Gordon and Breach, New York, (1997)

39. H Morkoc, B Sverdlov and G B Gao, Proceedings of IEEE, 81 , 492-556 (1993)

40. P Gay, P B Hirsch, A Kelly, Acta. Metall. 1, 315 (1953)

41. T Kitamura, S Nakashima, N Nakamura, K Furuta and H Okumura,   Phys. Stat. Sol. (c) 5, 6 ,1789 (2008)

42. V Yu Davydov, Yu E Kitaev, I N Goncharuk, A N Smirnov, J Graul, O Semchinova, D Uffmann, M. B Smirnov, A. P. Mirgorodsky and R. A. Evarestov Phys. Rev. B 58 ,12899(1998)

43. T Kozawa, T Kachi, H Kano, Y Taga, and M Hashimoto, N Koide and K Manabe , J. Appl. Phys. 75 , 1098 (1994)

Experimental Details

2.1 Experimental facilities

This chapter gives all the experimental details that have been used for growth, irradiation and subsequent characterization. Metal Organic Chemical Vapour Deposition (MOCVD) facility has been used for growing InGaAs/InP and AlGaN/GaN Multi Quantum Wells (MQWs) at Institute of Electronic Materials Technology (ITME), Warsaw, Poland. AlInN/GaN heterostructures have been grown using MOCVD at Tata Institute of Fundamental Research (TIFR), India. High energy irradiation work has been carried out at Inter University Accelerator Center (IUAC), New Delhi. Pristine and subsequently irradiated samples are characterized by High Resolution X-ray Diffraction (HRXRD) and Photoluminescence (PL) at TIFR, India. Similarly in-house facilities instituted at University of Hyderabad, such as HRXRD, Micro-Raman and Atomic Force Microscopy (AFM) facilities have also been extensively used. Rutherford Backscattering Spectrometry (RBS) technique has been carried out at Indira Gandhi Centre for Atomic Research (IGCAR), Kalpakkam, Centre for Ion Beam Applications (CIBA), National University of Singapore (NUS), Singapore and National Centre for Compositional Characterization of Materials (NCCCM), Hyderabad. Some of the Photoluminescence (PL) measurements have also been carried out at Coordinamento Interuniversitario Veneto per le Nanotecnologie (CIVEN) & Nanofab Laboratories, Venice, Italy. The aberration corrected Transmission Electron microscopy (TEM) investigations are done at Institute for Nanotechnology, Karlsruhe Institute of Technology (KIT), Germany.

The details of materials investigated are given in Table 2.1. These materials have been irradiated to understand the ion beam induced interface mixing and subsequent effects on structural and optical properties.

2.2 Accelerator facilities

2.2.1 Pelletron details:

High energy irradiation work has been carried out using 15MV tandem accelerator facility at IUAC [1]. This pelletron is a heavy ion tandem type of electrostatic accelerator.

In this, Ion source produces negative ions which are pre-accelerated to ~300 keV and then injected into an accelerator tank filled in with SF_6 (insulating gas).

Table.2. 1: Sample specifications with growth details

S.No	Sample specifications	Deposition technique	Source of samples/ Collaboration
1	InGaAs/InP X15 MQWs /InP(substrate) with $In = 0.23$	MOCVD	ITME, Warsaw, Poland
2	AlGaN/GaN X15 MQWs / Al_2O_3(substrate) MQWs with average $Al = 0.25$	MOCVD	ITME, Warsaw, Poland
3	GaN (5µm)/ Al_2O_3 (substrate)	MOCVD	Kyma technologies
4	AlInN/GaN(heterostructure) / Al_2O_3 (substrate) with $In = 0.12$	MOCVD	TIFR, Mumbai
5	AlInN/GaN (heterostructure) / Al_2O_3 (substrate) with $In = 0.21$	MOCVD	TIFR, Mumbai

At the centre of the tank, a terminal shell is maintained at a high voltage (~15 MV). Inside the terminal, a stripper uses a gas (usually N_2 or Ar) or a thin carbon which, upon collision removes electrons from the incoming negative ions. Then the positively charged ions experience a second boost of acceleration (hence the name "tandem" accelerator) as they exit the terminal and travel down the acceleration tube to ground at the high- energy end of the machine (Fig.2.1).

The primary benefits of the tandem configuration are:
a) The final beam energy is approximately (q + 1) times the terminal voltage, where q is the charge state to which the ions are stripped in the terminal.

b) On exiting from the tank, the ions are bent into horizontal plane by analyzing magnet, which select a   particular type of beam. The switching magnet diverts the high energy ion beams into various beam lines into different experimental areas of the beam hall. The entire machine is computer controlled and is operated from a separate control room.
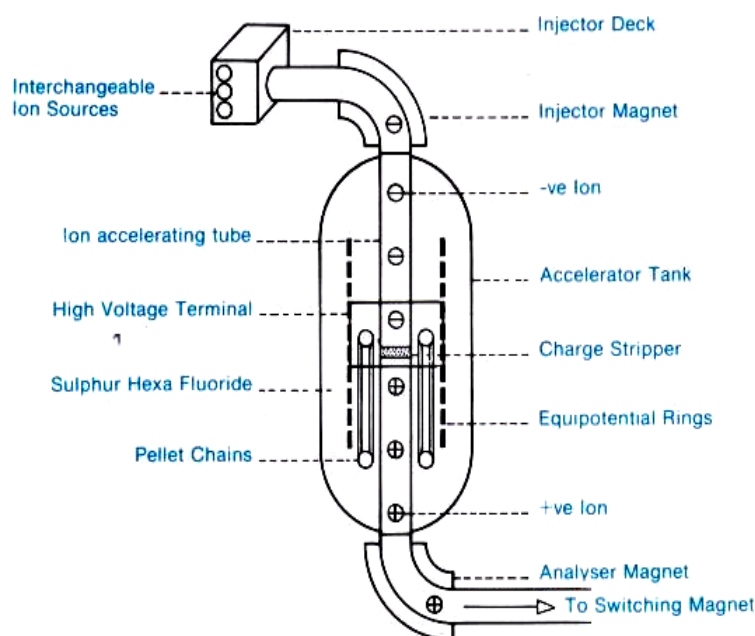
Fig.2.1: Schematic of 15MV pelletron accelerator

All the Irradiation experiments were performed in high vacuum irradiation chamber as shown in Fig.2.2. We have used 150 MeV Au, 100 MeV Au, 100 MeV Ag and 70 MeV Ni ions at varied fluences such as 1×10^{12}, 3×10^{12} and 1×10^{13} ions/cm^2. Necessary precautions were taken during irradiation to minimize heating of samples and channeling of ions by maintaining low beam currents and orienting samples to 5° with respect to beam axis, respectively.

Fig.2.2: Materials science high vacuum irradiation chamber

2.3 Rutherford Backscattering Spectrometry (RBS)

2.3.1 Tandem accelerator at IGCAR

Ion beam characterization work presented in this thesis has been carried out using the RBS facility at IGCAR, India. The tandem accelerator has dual source (i) Duoplasmatron (for H and He ions) and (ii) SNICS (Source of Negative Ions by Cesium Sputtering , for almost all other elements in the periodic table) with a terminal potential can be varied between 0.1 and 1.7MV (see Fig.2.3). The central feature of the Tandetron concept is a state of the art and SF_6 insulated parallel fed Cockroft-Walton type HV power supply characterized by high reliability, extreme low noise level, high voltage stability and low ripple. A high RF driving frequency, special RC-filtering and feedback circuits eliminate hum, drift and jitter and provide a high terminal voltage stability and low terminal voltage ripple without the need for slit stabilization. As the Tandetron HV power supply is a solid state power supply, it has the advantage of having no moving parts.
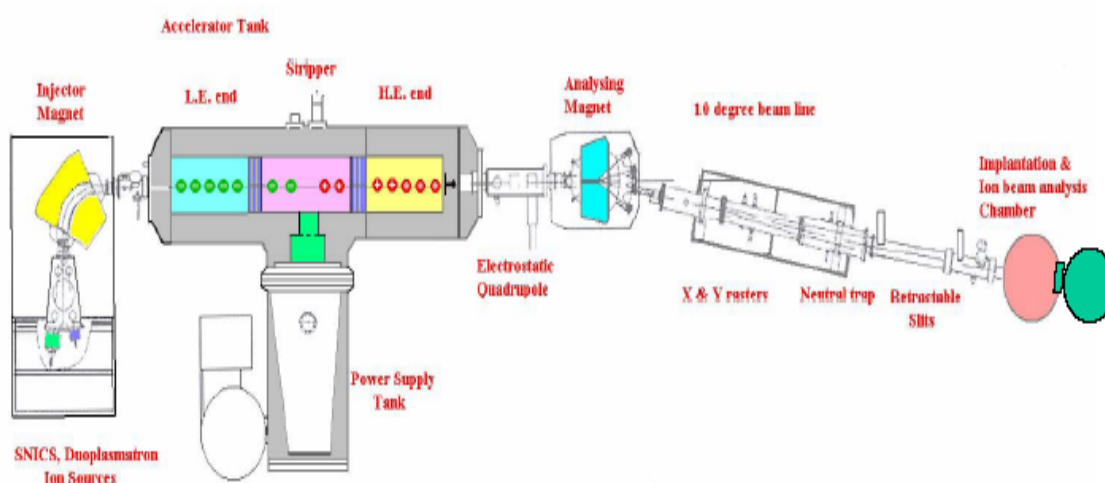
Fig.2.3: Schematic of 1.7MV tandetron accelerator

As a result there are no vibrations, which might result in terminal voltage fluctuations. Also, the ripple and stability values and dynamic behaviour are stable over many years of operation. A Generating Voltmeter (GVM) is used for measuring the terminal voltage. Stripper gas (N_2) at 7 kg/cm^2 is provided in the high voltage terminal by means of a plastic tube running through the column from outside the pressure tank to a metering valve feeding gas to the stripper canal. The plastic tube is of sufficient length to withstand the high voltage. It is kept as a coil mounted inside a teflon tube. A turbo molecular pump

33

is provided in the terminal to pump out and re-circulate the stripper gas so as to maintain a gas pressure of 50–100 microns in the stripper canal and 10^{-7} mbar in the accelerating tubes. The negative ions accelerated in the lower energy side are made positive by stripping of the electrons with N_2 gas. They are further accelerated by the high energy accelerating tube.

2.3.2 Duoplasmatron ion source

This source can provide H^+ and He^+ ions. Positive ion beam from the duoplasmatron ion source is accelerated by anode voltage of 100 V into a charge exchange canal. Lithium vapour introduced into the charge exchange canal converts 1-2% of the positive ions to negative ions. The negative ion beam is pre-accelerated by a gap lens to 10-20 keV and focused at the entrance of the 90^0 mass analyzing magnet.

2.3.3 Negative sputter ion source

This source (SNICS) can provide ions of almost all elements, which can form negative ions. The target material in solid form, necessary for producing the ion beam, is packed in a copper target holder and mounted in the source and 3 to 10 kV voltage is applied. Cesium ions, produced by thermal ionization of Cesium vapour sputter the target material. The sputtered atoms pass through a thin layer of Cesium on the target and negative ions are produced. They are pre-accelerated to 20 to 30 keV and focused at the entrance of the 90^0 mass analyzing magnet.

2.3.4 RBS/Channeling facility

The setup at IGCAR has some major parts which have been discussed elsewhere [2], The RBS/C facility has been automated using virtual instrument (V I) automation software. Corresponding RBS setup is shown in Fig.2.4. The dual axis Intelligent Motion controller (IMC) which accepts simple ASCII commands from the PC and controls the tilt angular rotation(u) to a resolution of 0.01° over 360° and the azimuthal angular rotation, (F) over 0 to 360° to a resolution of 0.001°.

In this RBS, the source generates a beam of collimated and monoenergetic particles of energy E_0. A typical case is a beam current 10 - 100 nA of 2 MeV He^+ ions in a 1-mm^2 area. Such ions impinge on the sample object to be analyzed. Almost all of the incident

34

particles come to rest within the sample. A very few ions scattered back from the sample, are detected using semiconductor detector which produces an analog signal proportional to the energy of backscattered particles. The output analog signal is processed by a multichannel analyzer, which subdivides its magnitude into series of equal increments. Each increment is numbered and referred to as a channel. An event whose magnitude falls within a particular channel is registered there as a count. At the end of the experiment each channel has registered a certain number of counts. The output of the multi channel analyzer is thus a series of counts contained in the various channels. The analog signal generated by the analyzer contains quantitative information on one particular parameter of the detected particle. Correspondingly, a spectrum obtained with such a detector is a backscattering energy spectrum.
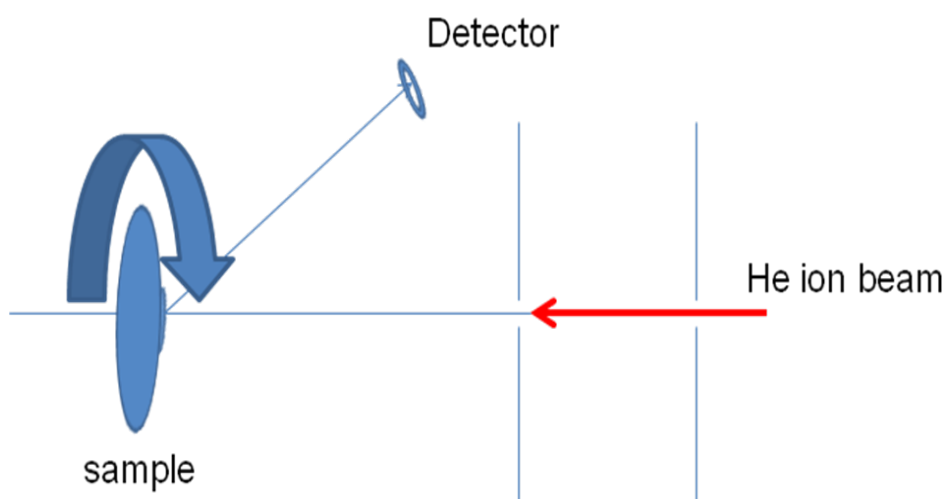
Fig.2.4: Schematic representation of RBS

2.4 High Resolution X-ray Diffraction (HRXRD):

HRXRD has been vital in finding out lattice parameters upto sensitivity of 10^{-5}. Essentially, the reasons for affecting lattice expansion or contraction are understood by HRXRD measurements and possible reasons are listed below:

(i) Electronically active defects in semiconductors can deform the conduction band [3], causing lattice parameters to increase with the increase in the electron concentration [4].

(ii) It depends on the size of dopant [5 ,6].

(iii)Residual strain is generally present even in supposedly strain-free samples [7]. The generation, redistribution and diffusion of point defects are thought to provide a strong contribution towards the residual strain [8]

2.4.1 X-ray generation and instrumentation

The electrons emitted from cathode are accelerated towards anode plate. The anode plate is typically made up of Copper (Cu) or Chromium (Cr) or Molybdenum (Mo). In these processes, bound electrons are first released and subsequently an electron from a higher energy level depletes to emptied state. Then the transition is associated with the emission of radiation that corresponds to the energy difference between the final and initial states. Thus, released energy depends upon the chemical nature of the emitting atom. According to different levels of transition leads to radiation as denoted by $K_{\alpha 1}$, $K_{\beta 2}$, L_{α}, etc. In most X-ray scattering experiments, only the characteristic emission lines are of interest. In the majority of cases, investigations are performed with K_{α} radiation, because of its higher intensity compared to K_{β}. The photon's wavelength and energy are given by the relationship

$$\lambda \ (\mu m) = 1.24 \ (eV\text{-}\mu m)/E \ (eV) \tag{2.1}$$

A closer look at the K_{α} radiation reveals its doublet nature. In such cases the weighted average of both lines is used as K_{α}. The K_{β} line may severely affect the diffraction pattern and to suppress it, a thin Nickel (Ni) foil edge filters are introduced into the incident beam path. Such suppressed K_{β} X-ray lines are then collimated and monochromatised using a Hybrid 4- bounce monochromator (multilayered mirror followed by a channel cut Ge crystal providing four bounces to X-ray beam). The output of the monochromator gives pure $K_{\alpha 1}$ line ($\lambda = 1.54056$ Å), which is then collimated to about 20 arcsec in the scattering plane. Hence, a primary monochromator has been used to eliminate unwanted wavelengths, $\Delta\lambda$, and to reduce δ (incident radiation divergence) to as low as 0.003°. Then at detector, a scintillation counter is used for detecting the scattered X-rays from sample. The 2θ value is defined accurately using a channel cut Ge crystal providing three reflections from (220) cut Ge crystals, generally referred to a triple axis attachment as shown in Fig.2.5. However, the triple axis attachment reduces the intensity considerably and is of use only for very high quality epitaxial layers or single crystals. Thus in our measurements, we have used different slits in front of the detector

besides using the triple axis geometry to improve resolution and to confirm the mosaic nature of crystals. The notation and details of experimental procedure are as follows:

ω – angle between incident beam and sample surface

2θ – angle between incident beam and detector

ψ – Sample tilt which allows 180° rotation of the sample about the intersection between the sample plane and the plane of X-rays

φ – in-plane sample rotation which allows 360° rotation about normal to the sample.

Before carrying out actual measurements, the following procedural steps have been undertaken to optimize the scattering geometry
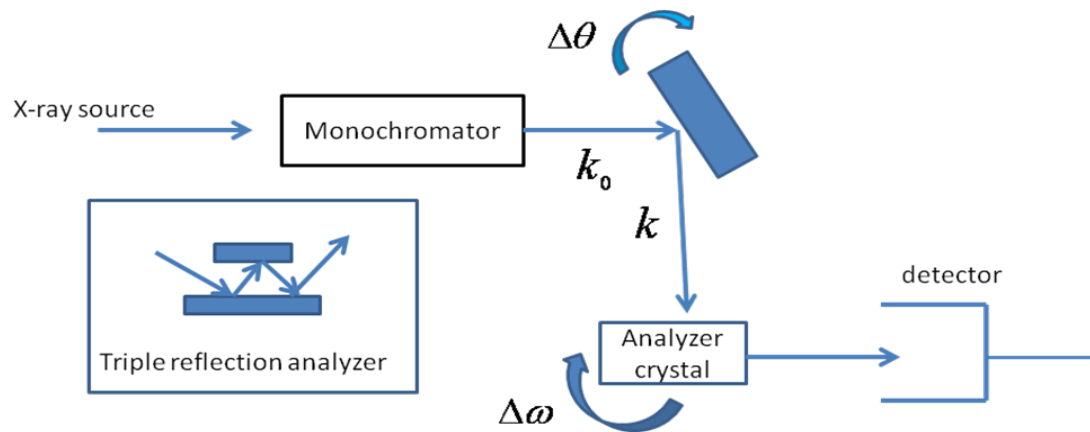
Fig.2.5: Schematic of HRXRD system in triple crystal diffractometer

1. The detector and incident beam were kept at 2θ = 0, and ω = 0. The detector slit was kept fully opened.

2. The sample was placed on the stage and it was raised such that X- ray intensity seen in the detector, falls off rapidly. The positioning of z-axis is done by selecting at half of its original intensity.

3. ω and 2θ are driven to the approximate angles for required Bragg peak.

4. ω-scan was performed for ~ ± 1° about the Bragg angle and fixed at the actual peak position for ω.

5. ψ scan was performed for ~ ± 5° and ψ was fixed at the actual peak position for ψ.

6. Step 4 was repeated and the value of ω was re-adjusted, if required.

7. φ scan was performed for ~ ± 5° and φ was fixed at the peak position for φ.

8. Step 4 was repeated and the value of ω was re-adjusted if required.

9. Steps 4 to 7 were repeated several times, until no change in peak positions were observed in these scans. The system is now aligned such that the collimated incident X-

ray beam satisfies the Bragg condition exactly for the epilayer/substrate. Under these conditions, open detector rocking curves were recorded.

10. 2θ scan was performed for ± 1° with small step size (~0.002°) and the detector was fixed at the peak position.

The above procedure results in the alignment of the instrument at the required Bragg peak with ψ and φ values optimized for the peak and ω offset is shown in Fig. 2.6 a). The ω, $\omega - 2\theta$ and φ scans were performed after these initial settings. In ω scan, the angle between incident X-rays and detector (2θ) remains constant at required Bragg condition ($2\theta = 2\theta_b$), and only incident angle changes as $\omega \pm \Delta\omega$ (Fig.2.6 b)).

Table 2.2 Factors affecting high angle $\omega - 2\theta$ diffraction scans of QWs and super- lattices

Factors	$\omega - 2\theta$
Composition of QWs and barriers	0th order and satellite peak positions and intensities
Repeat thickness	0th order and satellite peak positions and intensities
Decreasing number of repeats	Broadening of all peaks (except the substrate peak)
Thickness ratio	Positions of satellite minima
Total thickness	Fringe spacing
Rough or diffuse interfaces	Reduces observable higher order satellite peaks
Variation in MQW repeat thickness	Satellite broadening increases with increasing distance from the zero-order peak
Composition grading	Drop in intensity of higher –order satellite peaks
Crystalline defects	peak broadening

In ω-2θ scan, 2θ axis changes by twice the change in ω as shown in Fig.2.6 c). The value of ω and 2θ are related by, ω = 2θ/2 ± offset where offset is constant. Φ-scans were

performed by in-plane rotation of the sample after aligning the sample at the required Bragg peak as described above. Following effects of imperfections on the diffraction from a super lattices or MQW are summarized in Table 2.2.

The sample is mounted on a sample stage. The angles in the instrument are defined as follows:
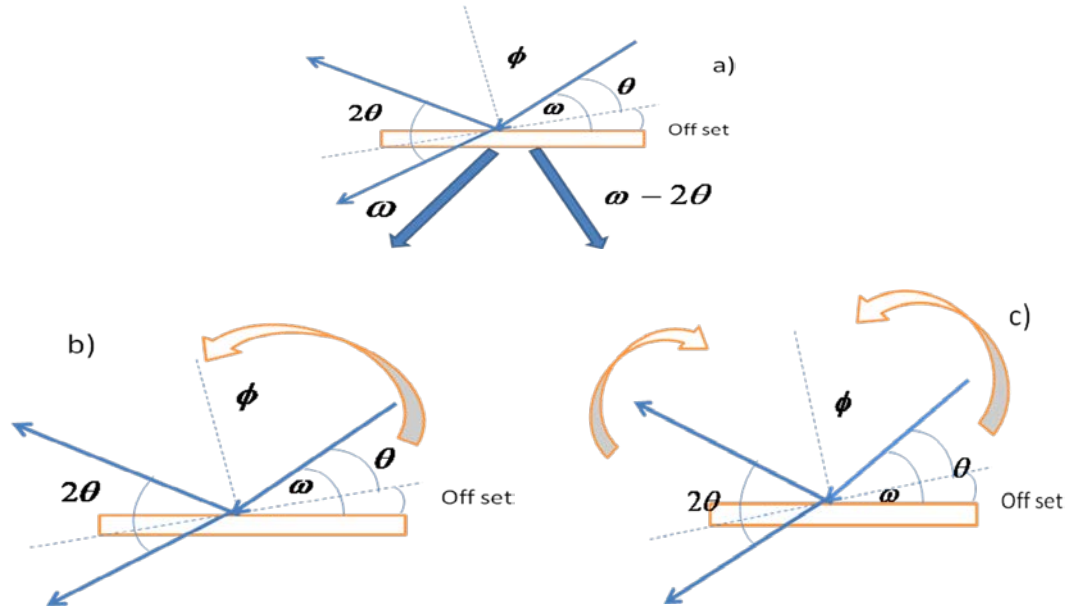
Fig.2.6: a) Scattering geometry of X- ray diffractometer after peak optimization   b) ω - scan geometry   c) $\omega - 2\theta$ scan geometry

2.5 Raman spectroscopy:
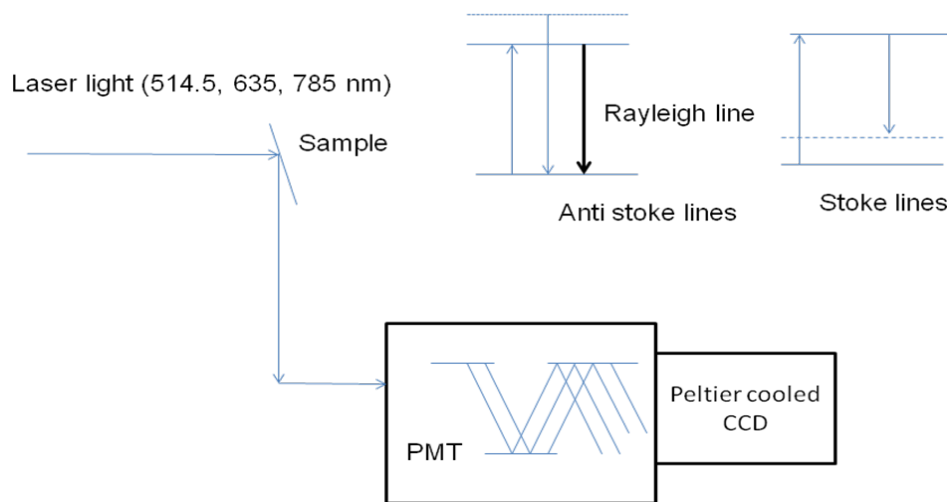
Fig.2.7: Schematic of micro Raman set up

In confocal microscopy, reflected light is collected with same objective and focused through multi mode fiber, which directs the beam to a spectrometer equipped with a Charge Coupled Device (CCD) camera. An enhancement of lateral resolution requires extremely small pinhole diameters. However, too small diameter of pinhole decreases the detection efficiency to a level usually unacceptable in the most experiments. Here the important number is numerical aperture, which determines the lateral resolution of the objective.

The maximum resolution of a classical microsope is given by the Rayleigh criterion

$$\Delta x = \frac{0.61 \times \lambda}{NA} \tag{2.2}$$

Where Δx is the smallest distance between two point objects that will appear separated in image plane, λ is the wavelength of excitation light and NA is the numerical aperture of the microscope objectives.

In this work, the Raman spectra have been recorded at room temperature using JOBIN YVON HORIBA HR-800 confocal micro-Raman spectrometer equipped with Ar+ laser (514.5 nm), at University of Hyderabad, Hyderabad. The laser power used was 18 mW and the resolution of instrument is 0.5 cm-1. The laser beam has been focused using different microscope objective lenses for different lateral spot size with different diameters (~ μm).

The scattered signals have been recorded in backscattering geometry as shown in Fig 2.7. The spectrograph is the box under the entrance optics of the instrument and forms a spectrum on the peltier cooled CCD detector. Raman spectra have also been collected using an Ocean Optics, Raman spectrometer (ISA Jobin-Yvon Spex HR-320, f/4.1). The spectra are recorded in spectral range of 200 to 2800 cm^{-1} by a thermoelectrically cooled CCD array detector with a 600 g/mm grating using NIR diode laser excitation of 785 nm.

2.6 Photoluminescence (PL):

Photoluminescence (PL) studies have been carried out at room temperature as well as at low temperatures. The low temperature has been achieved by Closed Cycle Refrigeration (CCR), as is normal for temperature requirements. The PL has been excited with 532 nm line and detected with a LN$_2$ cooled InAs detector after dispersing with 2/3m McPherson monochromator. On some samples, PL characterization techniques have been performed

using a Fluorolog-3 (Jobin-Yvon) spectro-fluorometer equipped with a Xenon lamp as excitation source and a monochromator with Photo Multiplier Tube (PMT) system for signal detection and spectral analysis. The PL has been excited with Xenon UV lamp (265nm) and detected with HAMAMATSU N2-cooled detector. These PL studies were carried out, on as grown and on irradiated samples at room temperature (295K). The Photoluminescence (PL) characterization has also been carried out at CIVEN & Nanofab Laboratories and the corresponding PL setup is shown in Fig. 2.8.
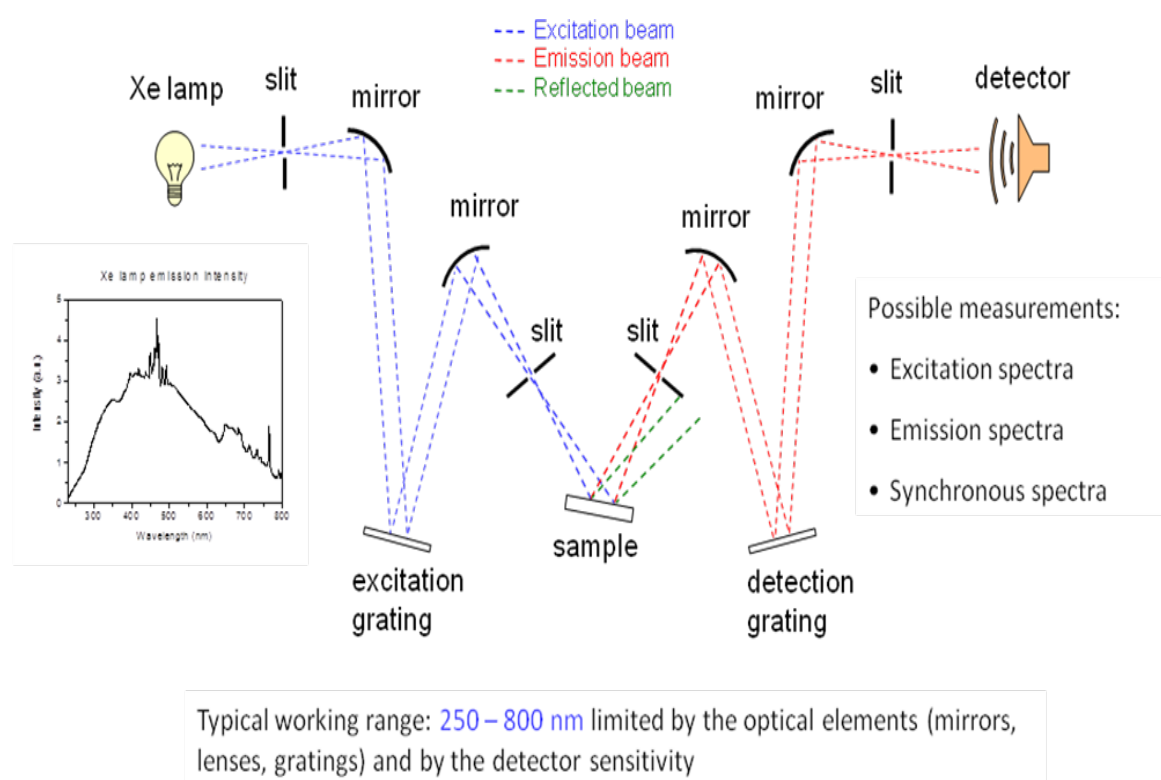
Fig.2.8: Schematic of Photoluminescence setup

The measurements have been performed with a Horiba Jobin Yvon Fluorolog-3 spectrofluorometer equipped with a 450W Xe lamp as excitation source, coupled to a double grating Czerny-Turner monochromator for wavelength selection. The detection system is constituted by a iHR300 single grating monochromator for spectral discrimination and a R928 Hamamatsu photomultiplier tube, sensitive in the 185-900 nm range, for signal collection and subsequent electronic conversion. The control of the whole apparatus and the storage of the data are provided by appropriate PC software.

41

2.7 Atomic Force Microscopy (AFM):
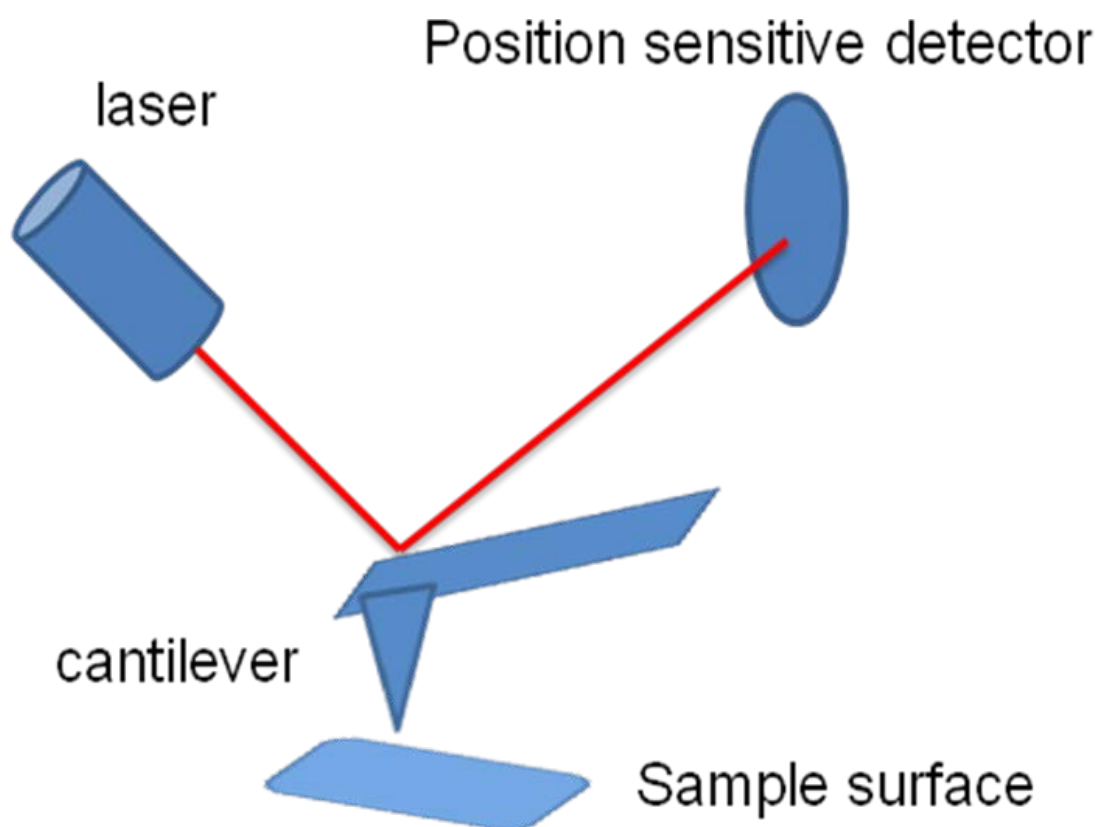
Fig.2.9: Schematic of AFM setup

Surface morphology of the samples has been characterized using SPA400, Seiko Instruments Inc. Schematic diagram of AFM is shown in Fig. 2.9. Images have been taken in contact mode using silicon nitride probe having spring constant of 0.58 N/m. A phase image, typically collected simultaneously with a topographical image, maps the local changes in material physical or mechanical properties [9]. Though phase images have been recorded but discussions are confined to the topographical images. In NC-AFM mode, the system monitors the resonant frequency or vibrational amplitude of the cantilever and keeps it constant with the aid of a feedback system that moves the scanner up and down. By keeping the resonant frequency or amplitude constant, the system also keeps the average tip-to-sample distance constant. As with contact AFM (in constant-force mode), the motion of the scanner is used to generate the data set. NC-AFM does not suffer from the tip or sample degradation effects that are sometimes observed after taking numerous scans with contact AFM. As mentioned above, NC-AFM is also preferable to

contact AFM for measuring soft samples. In the case of rigid samples, contact and non-contact images may look the same. However, if a few monolayers of condensed water are lying on the surface of a rigid sample, for instance, the images may look quite different.

2.8 Transmission Electron Microscopy (TEM):

An extensive microstructure analysis of films deposited on sapphire substrates has been carried out using Transmission Electron Microscopy (TEM) as shown in Fig.2.10. Electron diffraction patterns were used to identify the phase and structure of the films. The wavelength of electron depends on accelerating voltage. Thus, the de Broglie (particle–wave) relation $mv = \dfrac{h}{\lambda}$ and the kinetic energy of the electrons, $\dfrac{1}{2}mv^2 = eV$, are used to correct the inverse relationship between applied voltage and wavelength:

$$\lambda(nm) = \left(\frac{0.139 volts - nm^2}{V(volts)} \right)^{\frac{1}{2}} \qquad (2.3)$$

where V is the applied voltage in volts and wavelength λ in nm.

In electron diffraction, the wavelength of electron is small so is the Bragg angle (0.5°). Correspondingly Bragg's law establishes a relation between camera constant, inter atomic spacing and projection distance i.e

$$Rd_{hkl} = L\lambda \qquad (2.4)$$

where $L\lambda$. is known as the camera constant and R is the distance measured on the screen or photographic plate (e.g., mm or cm or m) and d_{hkl} (e.g., nm) is the interatomic spacing of the planes (*hkl*). The units of the camera constant are typically expressed in units of mm-nm or cm-nm or m-nm. The camera constant is a function of the lens settings. It is these lens settings that control the system's magnification, and the electron energy determines the value of the wavelength.

High Angle Annular Dark Field - Scanning Transmission Electron Microscopy (HAADF-STEM), high resolution TEM, and qualitative energy dispersive X-ray (EDX) nano analysis have been performed using a FEI Titan 80-300 equipped with an objective lens aberration corrector. The microscope was operated at 300 kV providing a resolution of

0.08 nm in TEM mode and 0.14 nm in STEM mode. The HAADF-STEM images are recorded with a camera length of 196 mm and a convergence angle of 9.5 mrad. All the HAADF-STEM and HRTEM images presented in this thesis are raw images only adjusted for contrast, brightness and intensity.

Sample preparation for TEM analysis: Ultrasonic disc cutter was used for cutting circular 3mm disk. Such disk was transferred on to cylinder and fixed with wax by facing sample upside-down. Then disc grinder was used to grind sample thickness down to 300 nm. Subsequently, dimpling was done to 120 nm and latter shifted to argon ion milling PIPS system, where it was aimed for making electron transparent. Specimens for cross-sectional TEM analysis were prepared by mechanical polishing, followed by argon ion milling using a Gatan PIPS system at an angle of 3° and a voltage of 5 kV or using a FEI Strata 400 S Dual Beam Focused Ion Beam (FIB) with in-situ lift-out.
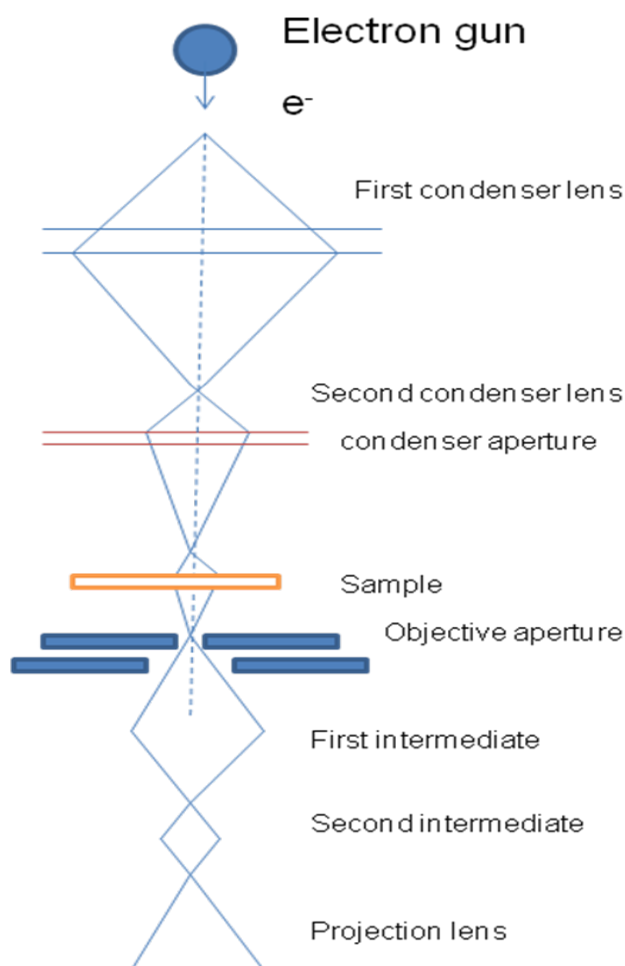
Fig.2.10: Diagram displaying the cross section of a transmission electron microscope and the path of the electron beam down the column of the TEM.

2.9 Rapid Thermal Annealing (RTA):

Thermal annealing is necessary for ion implanted samples to anneal out lattice damages. However, swift heavy ions predominantly loose energy to target electrons leading to dislodging of atoms through electron- phonon coupling. Thus, such created point defects have detrimental effects on luminescence properties. Subsequently, samples are then subjected to Rapid Thermal Annealing (RTA) to minimize the irradiation induced damages. RTA on these samples have been carried out at different annealing temperatures such as 700 °C and 900 °C for 60 sec in Nitrogen atmosphere with a flow rate of 1000 Standard Cubic CM (SCCM) using RXV6 Rapid Thermal Processor (RTP) system (AET Thermal, Inc). The surface of these samples were capped with a layer of silicon nitride (Si_3N_4), deposited by plasma enhanced chemical vapour deposition (PECVD). The Si_3N_4 layer was subsequently removed using a buffered HF solution after annealing. The choice of the temperature and time is fixed from available literature values [10,11].

2.10 Conclusions:

This chapter describes all the experimental facilities that have been utilized for work reported in this thesis. These include the Swift Heavy ion irradiation (SHI) facilities, and those used for characterizing the pristine and irradiated samples. Further details of the relevant facilities have been discussed in the following chapters wherever required.

References:

1. D Kanjilal, S Chopra, M M Narayanan, I S Iyer, V Jha, R Joshi and S K Datta, Nucl. Instr. and Meth. A 238, 97 (1993)

2. K Suresh, B Sundaravel, B K Panigrahi, K G M Nair and B Viswanathan, Rev. Sci. Instrum. 75, 4891 (2004)

3. S Burkner, M Baeumler, J Wagner, E C Larkins, W Rothemund, and J D Ralston, J. Appl. Phys. 79, 6818 (1996)

4. N Yamada, G Roos, and J S Harris Jr, Appl. Phys. Lett. 59, 1040 (1991)

5. M Leszczynski, H Teisseyre, T Suski, I Grzegory, M Bockowski, J Jun, S Porowski, K Pakula, J M Baranowski, C T Foxon and T S Cheng, Appl. Phys. Lett. 69, 73 (1996)

6. M Krysko, M Sarzynski, J Domagala, I Grzegory, B Lucznik, G Kamler, S Porowski and M Leszcsynski, J. Alloys Compounds 401 , 261 (2005)

7. C G Van de Walle, Phys. Rev. B 68, 165209 (2003)

8. S Porowski, J. Cryst. Growth 189/190 , 153 (1998)

9. S N Magonov, V Elings and M -H Whangbo, Sur. Sci. Lett. 375, L385 (1997)

10. V Darakchieva, T Paskova, P P Paskov, B Monemar, N Ashkenov and M Schubert, J. Appl. Phys. 97 , 013517 (2005)

11. T Paskova, D Hommel, P P Paskov, V Darakchieva, B Monemar, M Nockowski, T Suski, I Grzegory, F Tuomisto, K Saarinen, N Ashkenov and M Schubert, Appl. Phys. Lett. 88 , 141909 (2006)

Chapter-III

Ion beam modification studies in InGaAs/InP MQWs

3.1 Introduction

InGaAs/InP Multi Quantum Wells (MQWs) have numerous applications in optoelectronics such as high speed and low dark current p-i-n photodetectors for long wavelength optical communications [1,2]. These heterostructures are also model systems for understanding semiconductor growth processes where mixed group of III-V interfaces are involved. Quantum well inter diffusion technology has become increasingly important in the drive towards fabrication of photonic integrated circuits due to its versatile band gap tuning process. These structures were realized with advent in growth techniques like Metal Organic Chemical Vapour Deposition (MOCVD) [3]. Growth of hetero structures on lattice mismatched substrates with uniform strain in the over-layer, results in additional advantages. Such strain lifts the degeneracy of light hole and heavy hole at the valence band maxima, which is crucial for high speed device applications [4,5]. Lattice mismatched hetero structures are useful in tuning the band gap of III-V compound semiconductors [6, 7]. In strained hetero-structures, epilayer thickness is an important parameter. Beyond a certain critical thickness, the strain gets relieved by generating misfit dislocations which eventually deteriorate the device performance. Such studies on tensile strain relief beyond critical thickness have been carried out by many researchers [8-9].

Interfacial properties of InGaAs/InP lattice matched MQWs [10] and their diffusion co-efficient in InGaAs/InP MQWs by Rapid Thermal Annealing (RTA) [11] have been studied. Difference in intermixing effects in InGaAs/InP heterostructures by high temperature annealing [12] and swift heavy ion bombardment have been investigated [13,14]. Thermal stability of InGaAs/InP quantum wells is important which has been thoroughly studied [15]. On the other hand, quantum well intermixing at the interfaces have been demonstrated by impurity induced inter-diffusion [16], impurity free disorder using various dielectric cap layers [17], ion implantation [18] and focused ion-beam induced intermixing [19]. Among these, damage formation owing to nuclear stopping has been understood in greater detail [20, 21]. Despite the very similar electronic energy loss in InP and GaP, the number of displaced atoms leading to damage formation is very significant in InP [22]. Thus, a detailed and clearer understanding of ion-solid interactions by passage of SHIs through matter is required [23-26]. Moreover, It has been reported

band gap can be tailored with interface mixing using swift heavy ion irradiation in lattice matched InGaAs/InP hetero-structures [27]. Recently we have demonstrated that SHI modifies strain in both lattice matched heterostructures and relaxed MQWs [28,29]. Swift heavy ions deposit energy via electronic energy loss mechanism and create defects into the quantum well active region, which allows atomic diffusion to takes place between the quantum wells and barriers. Swift heavy ion irradiation induced intermixing has already been observed in metal/semiconductor interfaces. In the present work, much emphasis has been given to swift heavy ion induced mixing and consequent effects on band gap modification of InGaAs/InP multi quantum wells.

Here we have studied swift heavy ion irradiation and followed by annealing effects on InGaAs/InP MQWs. High Resolution X-ray Diffraction, Photoluminescence and Atomic Force Microscope characterization techniques have been used for structural, optical and surface properties.

3.2 Experimental details

InGaAs/InP MQWs were grown on semi-insulating InP substrate by MOCVD at IEMT Warsaw, Poland. MQWs growth had been carried in computer controlled horizontal LP-MOVPE Axitron, model 200R&D,on 2inches InP(100) oriented substrates. Trymethyl gallium (TMGa), Trymethylindium (TMIn) and 100% arsine (AsH_3) and Phosphine (PH_3) were used as source gases. The operating pressure in the reactor was maintained at 100mbar, III/V ration at 200 and substrate temperature was at 650-700 °C. The irradiation was performed at room temperature. The samples were irradiated with 100 MeV Au^{8+} ions at varied fluence from $5x10^{12}$ to $1x10^{13}$ ions/cm^2 by scanning over 1x1cm^2 from IUAC, New Delhi 15MV Pelletron accelerator. During irradiation necessary precautions were taken to avoid heating of sample and channeling of ions into the sample by adjusting to low beam currents and orienting the sample at angle of about 5° with respect to beam axis respectively. The irradiated samples were then subjected to RTA in order to anneal out the irradiation induced damages in the samples .The annealing was done at 700°C for 60 sec in Nitrogen atmosphere with a flow rate of 1000 SCCM using RXV6 Rapid Thermal Processor (RTP) system (AET Thermal, Inc.). The surface of these samples were capped with a layer of silicon nitride (Si_3N_4), deposited by plasma enhanced chemical vapour deposition (PECVD). The Si_3N_4 layer was subsequently removed using buffered HF solution after annealing. Pristine, irradiated and annealed samples were studied by

HRXRD, PL and AFM characterization techniques. The HRXRD experiments had been performed using Philip X'pert system with $K_{\alpha 1}$ line (λ = 1.54056 Å). Profiles of (004) symmetric scans were recorded in ω –2θ scan by optimizing tilt and azimuthal angles. Photoluminescence studies were carried out at room temperature (295K) as well as at low temperature (18K). PL was excited with YAG laser (532nm) and detected with a LN_2 cooled InAs detector after dispersing with 2/3m McPherson monochoromator. Surface morphology of samples was characterized by AFM (in Dynamic Force Microscopy mode) using SPA 400, Seiko Instruments Inc.

3.3 Results and Discussion

3.3.1 High Resolution X- ray Diffraction (HRXRD)

As grown and swift heavy ions irradiated InGaAs/InP MQWs have been investigated by HRXRD measurements. The average composition peak (0th order peak) is well resolved from the substrate peak ($\Delta\theta$ = 0.0468); this indicates a tensile strain in the layer.

The mean super lattice (SL) period (combined thickness of one InP and one InGaAs layer) is calculated from the measured angular separation between the satellite peaks and is given by,

$$2\Lambda\left(\sin\theta_n - \sin\theta_0\right) = \pm n\lambda \tag{3.1}$$

where θ_n is the diffraction angle of the order n, θ_0 is the angle of zeroth order peak, λ is the Cu K_α X-ray wavelength of 1.5406 Å, Λ is the mean super lattice period. The estimated Λ from (004) scan was found to be 25 nm for M-U samples which is close to the nominal one.

The difference in the lattice parameter between the $In_{0.23}Ga_{0.77}As$ and InP layers results in a tensile strain in the InGaAs layer. The calculated tensile strain is approximately 0.366% in the layer. Simulations have been used for fitting the measured experimental HRXRD spectrum using the dynamical theory based Philip's Xpert Epitaxy software. The composition and thickness of the layers have been optimized by a trial and error method starting from nominal values until a satisfactory fit is observed. The simulated scan matches reasonably well with the experimental data for nominal thickness and composition of the layers as shown in Fig.3.1.

Table.1: Sample IDs and details

S. No	Sample ID	Details	Strain (%)
1	MQW-U	As-grown $In_{0.23}Ga_{0.77}As$ (5nm)/InP(20nm) MQW of 15 periods	0.366
2	MQW-I1	100 MeV Au ion irradiated with a fluence of 5×10^{12} ions/cm^2	0.0368 w.r.t to Pristine
3	MQW-I2	100 MeV Au ion irradiated with a fluence of 1×10^{13} ions/cm^2	All the peaks have disappeared
4	MQW-I1-A	MQW-I1 sample rapid thermal annealed at 700 ^{0}C for 60 sec in N_2 atmosphere.	0.079 w.r.t to Pristine
5	MQW-I2-A	MQW-I2 sample rapid thermal annealed at700 ^{0}C for 60 sec in N_2 atmosphere.	0.0560 w.r.t to Pristine

As a function of ion fluence, the interface mixing induced disorder is observed from the vanishing of satellite peaks. Subsequently, these samples were subjected to Rapid thermal annealing to anneal out the defects introduced by irradiation. Annealing at 700°C for 60 s was performed on MQW-I1 and MQW-I2 samples. Necessary proximity capping layer has been deposited before annealing to arrest the out-diffusion of arsenic during annealing process. Irradiated and subsequently annealed samples show that there is a shift in zeorth order peak. Initially tensile strained MQWs have been further strained by the ion bombardment. These measurements yield strain values as given in Table.1.

Fig.3.2 shows the comparison of MQW-U, MQW-I1 and subsequently annealed samples where the peak shifts are clearly visible, indicating strain is induced into layers. The average tensile strain of 0.0360% in MQW-I1 increased to 0.079% upon annealing. Rapid thermal annealing causes intermixing of quantum wells by indium and gallium diffusion. The decrease in *In* composition has resulted in a shift of satellite peaks to the higher angles which confirms the reduction of epilayer lattice constant. As a result, strain into the epilayers further increases and causes a change in the band gap.
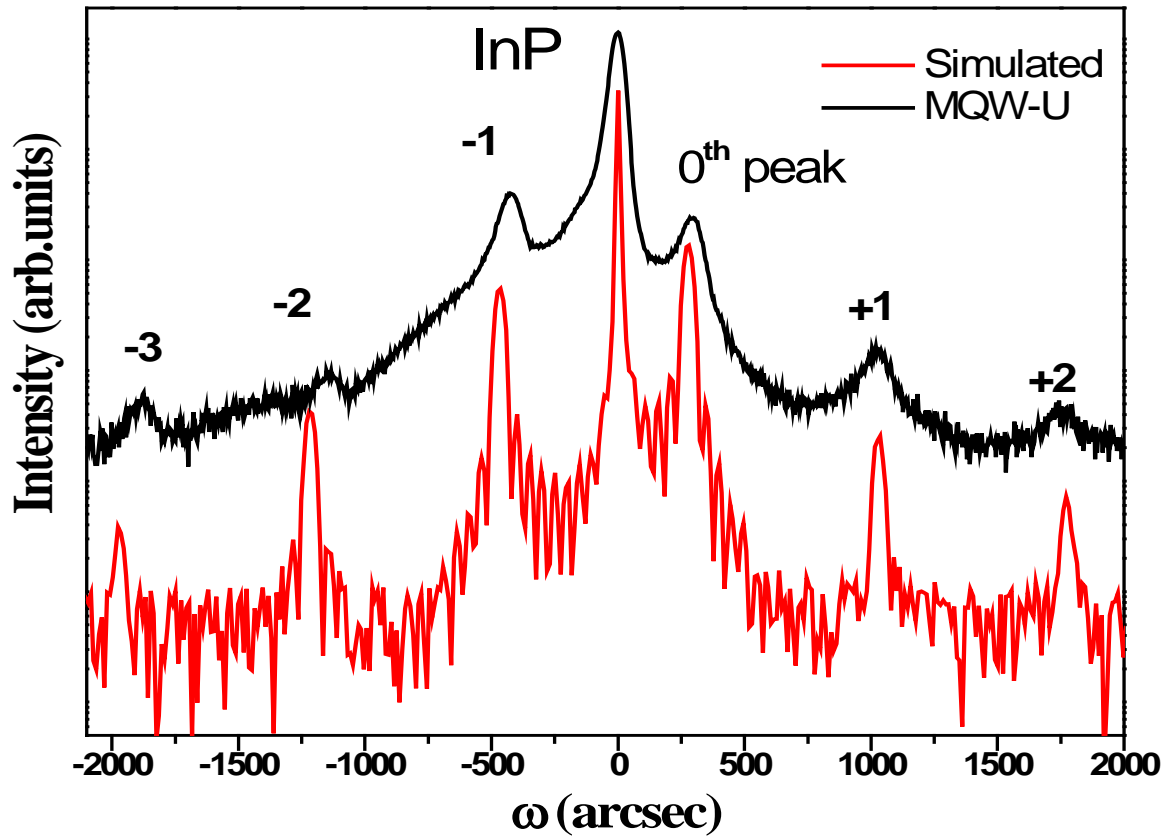
Fig.3.1:   HRXRD (004) scans of MQW-U and simulation fit.

Fig.3.3 depicts that all the abrupt interfaces of MQWs have been drastically affected due to bombardment at higher fluence. Upon annealing, the irradiated MQWs have significantly recovered with improved intensity of satellite peaks as shown in Fig.3.3.

3.3.2 Photoluminescence (PL)

The irradiated MQWs do not show any PL due to defect induced non-radiative recombination centers. However, LT-PL spectra have been measured from MQW-U, MQW-I1-A and MQW-I2-A samples as shown in Fig.3.4. Change in the band gap as a function of ion fluence has been noticed. The sample MQW-I1-A has good PL intensity and a better peak width compared to MQW-U. The MQW-I2-A has two Gaussian profiles indicating that there are residual defects. Finally, the PL peak shifts by 45 nm and 82 nm for MQW-I1-A and MQW-I2-A have been observed, respectively. This study reveals that the desired band gap can be tailored by irradiation followed by optimized annealing conditions.
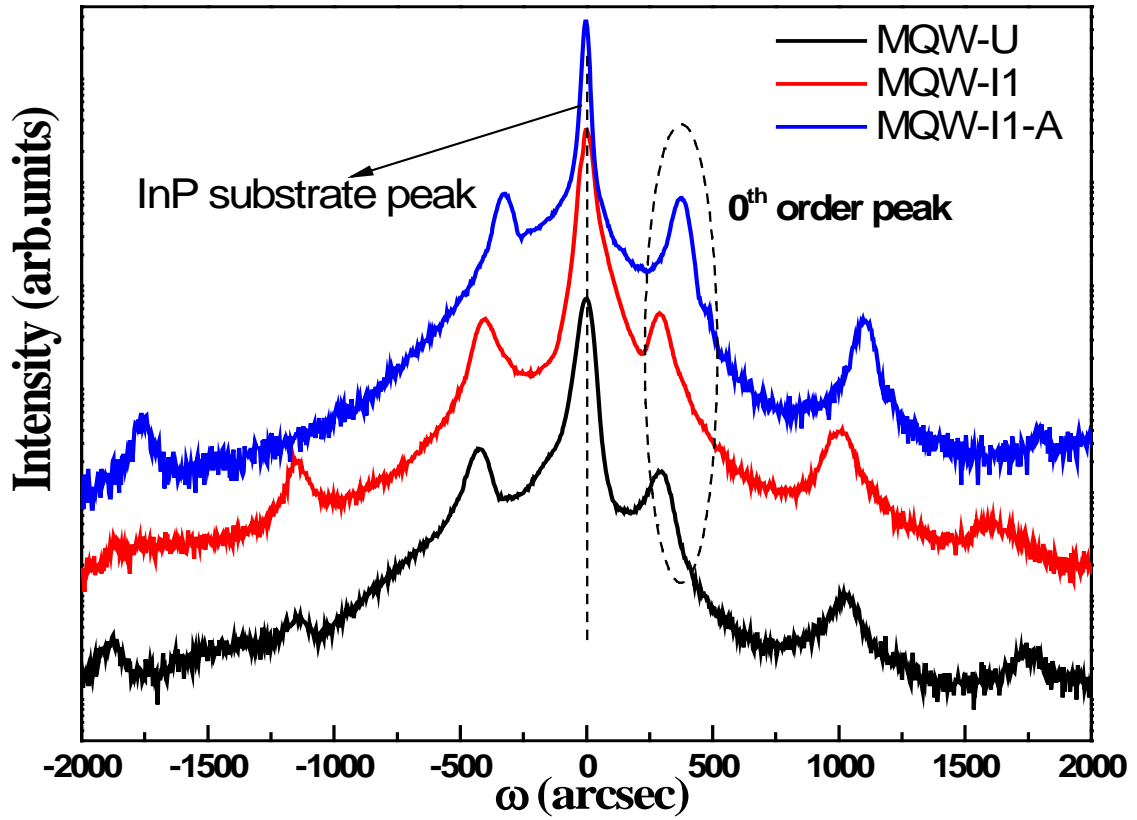
Fig.3.2: HRXRD (004) scans of MQW-I1 and MQW-I1-A.

Band gap engineering in similar samples using low energy ion irradiation and/or annealing have been demonstrated by some investigators [26–29]. In the present study, band gap engineering by as high as 82 nm has been achieved by swift heavy ions. The band gap engineering using low energy ions is normally due to introduction of point defects into the active region, which allows atomic diffusion to take place between the layers. However, swift heavy ions induce the atomic diffusion to take place that affected electronic energy band gap which may be attributed solely to the electronic energy loss (~15keV/nm). Such studies are useful for spatial band gap engineering of optoelectronic devices in a controlled manner.

3.3.3 Atomic Force Microscopy (AFM)

Fig.3.5 shows the surface morphology of samples and we notice that the irradiation increases the roughness from 0.15 nm to 0.45 nm. Increased roughness is not noticed very much from the RMS values. Hence, the ion irradiated MQWs do not show any detrimental surface effects. The surface of the irradiated sample show hillocks as

observed in earlier works [30]. Also the number of hillocks is not matching with the ion fluence indicating a collective damage of the incident ions at the surface.
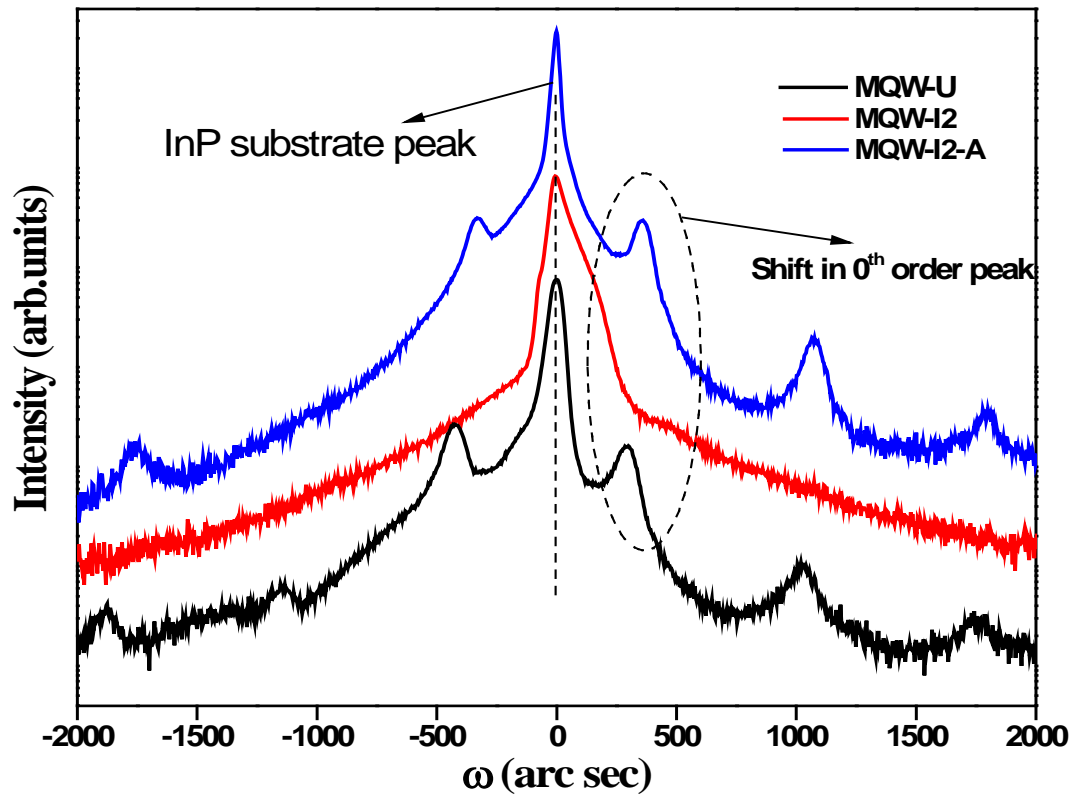
Fig.3.3: HRXRD (004) scans of MQW-I2 and MQW-I2-A.
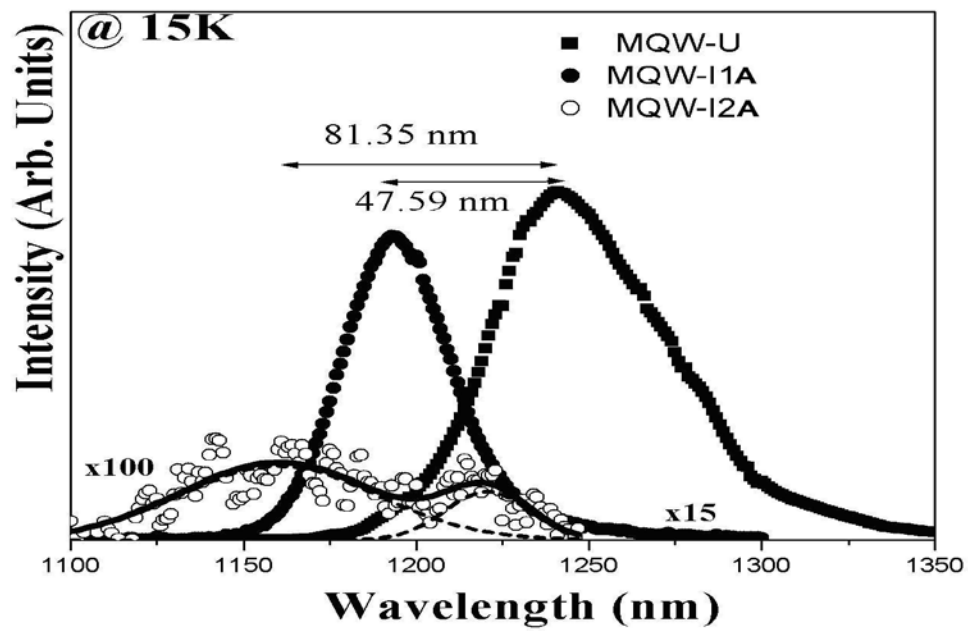
Fig.3.4: LT-PL spectra of MQW-U, MQW-I1-A and MQW-I2-A samples.
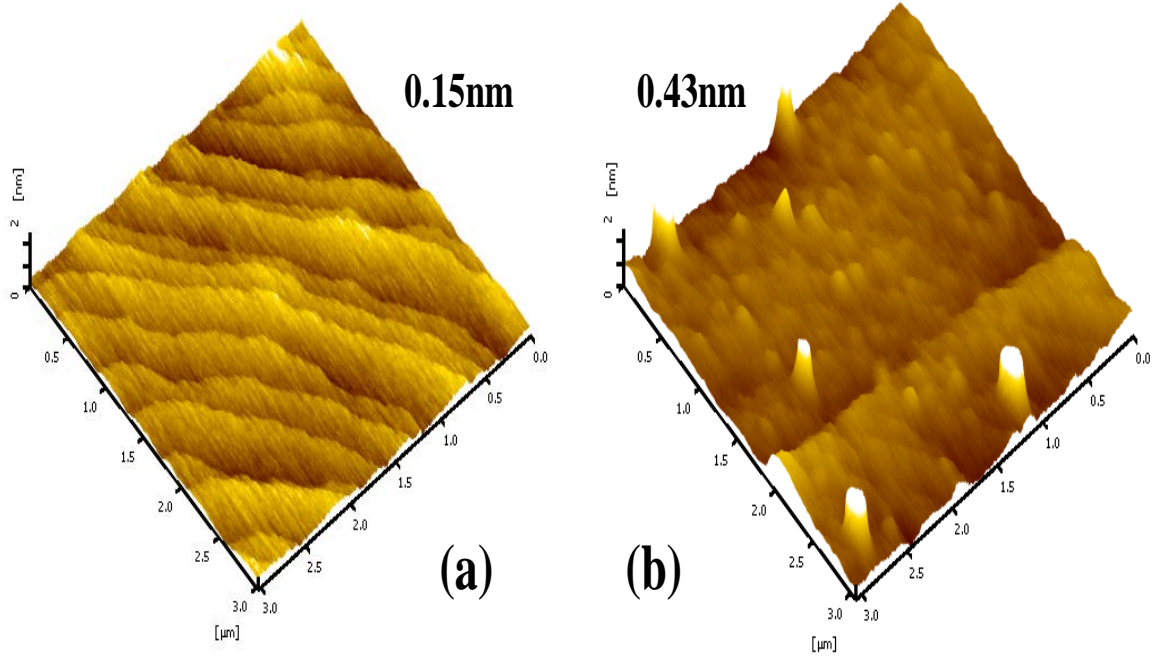
Fig.3.5: Surface morphology of samples MQW-U and MQW-I2

3.4 Conclusions

The present work demonstrates the swift heavy ion induced effects on strain and band gap. HRXRD, PL and AFM have been utilized to understand respectively, the interface, optical and surface modifications upon irradiation. Irradiation changes the strain but after annealing the interface quality improves as evident from HRXRD measurements. Photoluminescence has not been observed on irradiated MQWs due to non-radaitive recombination centers. However, change in band gap as a function of ion fluence has been noticed. The sample MQW-I1-A has good PL intensity and a better peak width compared to MQW-U. The MQW-I2-A has two Gaussian profiles indicating that there are residual defects. Finally, the PL peak shifts by 45 nm and 82 nm for MQW-I1-A and MQW-I2-A respectively, have been observed. The AFM images show that roughness does not increase much after irradiation which can be useful in many applications. Finally, it is observed that higher fluence lead to rupturing of bonds at the interfaces which upon annealing are retrieved that led to interfaces intact. Finally, it is concluded that the interfacial mixing induced strain is the main cause of band gap modifications. Desired band gap can be achieved if and only if irradiation and annealing process are optimized.

3.5 References

1. J C Campbell, in "Optoelectronic Technology and Lightwave Communication Systems" (Chinlon Lin ed.) p-363 Van Nostrand Reinhold, New York (1989).

2. Y G Wey, D L Crawford, K Giboney, J E Bowers, M J Rodwell, P Silvestre, M J Hafich and G Y Robinson, Appl. Phys. Lett. 58, 2156 (1991).

3. I C Bassignana, C J Miner and N Puetz, J. Appl. Phys. 65, 4299 (1989)

4. E P O'Reilly, Semicond. Sci. Technol. 4, 121 (1989)

5. N G Einspruch, W R Frensely (Eds.), Heterostructures and Qunatum Devices, Academic Press, San Diego, 1994

6. T P Pearseal (Ed.), Semiconductors and Semimetals, Vol. 33, Academics Press, New York,1991

7. G C Osbourn, Phys. Rev. B 27, 5126 (1983)

8. M Gendry, V Drouot, C Santinelli and G Hollinger, Appl. Phys. Lett. 60, 2249 (1992)

9. P Maigne, M Gendry, T Venet, Y.Tahri, and G Hollinger, Appl. Phys. Lett. 69, 5 (1996)

10. D M Cornet, R R Lapierrea, D Comedi and Y A Pusep, J. Appl. Phys. 100, 43518 (2006)

11. S W Ryu,B D Choe and W G Jeong, Appl. Phys. Lett. 71, 1670 (1997)

12. F Bollet, W P Gillin, M Hopkinson and R Gwilliam, J. Appl. Phys. 93, 3881 (2003)

13. A Krost, J Bohrer, H Roehle and G Bauer, Appl. Phys. Lett. 64, 469 (1994)

14. J M Vandenberg, A T Macrander,R A Hamm and M B Panish, Phys. Rev. B 44, 3991 (1991)

15. H Peyre, F Alsina ,J Camassel,J Pascual and R W Glew, J. Appl. Phys. 73, 8 (1993)

16. D G Deppe and N Holonyak, J. Appl. Phys. 64 , R93 (1988)

17. H H Tan, J S Williams, C Jagadish, P T Burke and M Gal, Mater. Res. Soc. Symp. Proc. 396 , 823 (1996)

18. J D Ralston, A L Moretti, R K Jain and F A Chambers, Appl. Phys. Lett. 50, 1817 (1987)

19. J P Reithmaier and A Forchel, IEEE. J. Quant. Elec. 4 , 595 (1998)

20. E Wendler, T Opfermann, and P I Gaiduk, J. Appl. Phys. 82, 5965 (1997)

21. E Wendler, B Breeger, C Schubert, and W Wesch, Nucl. Inst. and Meth. B 147, 155 (1999)

22. O Herre, W Wesch, E Wendler, P I Gaiduk, F F Komarov, S Klaumünzer, and P Meier, Phys. Rev. B 58, 4832 (1998)

23. E M Bringa and R E Johnson, Phys. Rev. Lett. 88, 165501 (2002)

24. G Schiwietz, K Czerski, M Roth, F Staufenbiel, and P L Grande, Nucl. Inst. and Meth. B 226, 683 (2004)

25. S Klaumünzer, *Ion Beam Science: Solved and Unsolved Problems*, The Royal Danish Academy of Sciences and Letters, Copenhagen, 2006, p. 293

26. C. S. Schnohr, P. Kluth, R. Giulian, and D. J. Llewellyn, A. P. Byrne, D. J. Cookson and M. C. Ridgway**,** Phys. Rev. B 81, 075201 (2010)

27. S Dhamodaran, A P Pathak, A Turos, G Sai Saravanan, S A Khan, D K Avasthi and B M Arora, Nucl. Inst. and Meth. B 266, 583 (2008)

28. S V S Nageswara Rao ,A P Pathak, A M Siddiqui, D K Avasthi, C Muntele, D Ila, B N Dev, R Muralidharan, F Eichhorn, R Groetzschel and A Turos, Nucl. Inst. and Meth. B 212, 442 (2003)

29. S Dhamodaran, A P Pathak, A Turos, R Kesavamoorthy, B Sundaravel, K G M Nair and B M Arora, Nucl. Inst. and Meth. B 266, 1908 (2008)

30. M A G Halliwell, M H Lyons, M J Hill, J. Cryst. Growth. 68, 523 (1984)

Chapter-IV

Electronic energy loss dependence studies in MOCVD grown GaN

4.1 Introduction

III-V compound semiconductors have numerous applications in optoelectronic devices and in particular III-Nitride compound semiconductors (GaN,InN and AlN) are extensively used in high frequency and high power applications. III-Nitrides show good luminescence properties in spite of huge defect densities arising from lattice and thermal mismatch with the underlying substrates. Subsequently, AlN and GaN as a buffer layers have been used between substrate and epilayer which improves structural and optical properties. However, there is an inbuilt strain at the interfaces which significantly affects structural as well as optical properties. The effect of strain in hetero epitaxial GaN is an important parameter for improving its device performance and to change the band structure. Thus, it is important to characterize the substrate-induced strain. This biaxial residual strain has been determined by X-ray diffraction [1, 2] and their consequent strain effects on optical properties have been investigated using photoluminescence (PL) [2, 3] and Raman spectroscopy [2, 4–6]. It is known that residual strain greatly changes electrical properties of two-dimensional electron gas (2DEG) [7]. Recent studies by Aziz et. al [8] have shown that change of strain by etching the substrate increases the electron sheet density and mobility by 25% and 20%, respectively.

Owing to their technological importance in space applications, more understanding is required about the influence of external radiation in general and ion beam interactions on III- V compound semiconductors, in particular. Ion-irradiation-induced amorphization of III-V semiconductors has been extensively studied in the nuclear stopping regime for several decades. Damage production and annihilation by electronic energy deposition are not yet clear. However, it is known that irradiation of high-energy particles, such as neutrons and electrons, can induce structural defects in semiconductors. There have been attempts to address such issues pertaining to charged particle bombardments in GaN with high energy electrons [9- 12], low energy electrons [13] and heavy ions [14]. Similarly, some studies [15,16,17,18] have also been reported about the effects of neutron irradiation on the micro structural and optical properties of GaN thin films. In the last

decade, there have been many reports discussing the irradiation-Induced defects in silicon [19], GaAs [20-22], GaP [23], InP [24,25] and GaN [26]. Experimental observations revealed that higher band gap materials are more susceptible to SHI irradiation than lower band gap materials [24]. It has been noticed that $Ga_{0.50}In_{0.50}P$ is heavily damaged while InP is almost amorphized for nearly identical ion-energy loss. However, damage in GaP and GaAs remain almost insignificant [24] but $Ga_{0.47}In_{0.53}As$ exhibits intermediate behavior between InAs and GaAs [23]. Many researchers have used ion irradiation to investigate GaN [27,28,29,30,31], not only to understand the ion- solid interaction mechanism but also as a useful tool for tailoring the strain, which in turn triggers structural and electrical properties in a selective and controlled manner. On the other hand, SHI irradiation also has been used to anneal out pre-existing defects by electronic excitation in InP and GaAs [32]. Effects of ion beams on optical and structural properties of semiconductors like GaN and related materials have also been discussed [33-37].

When a swift heavy ion passes thorough the materials, it deposits energy to target atoms via electron-phonon coupling by electronic excitation or ionization of target electrons. This eventually leads to high pressure and high temperature conditions in the target material, not otherwise possible under thermal equilibrium conditions. Due to the rapid energy transfer variety of effects can occur in materials, like defects creation, defects annealing, crystallization, amorphization [38]. Most of the high-energy irradiation results are normally understood based on some explanations about planar defects, de-lamination, and tracks propagation [39-40].

In the present study, Irradiation-induced defects and their effects on luminescence using Raman scattering and Photoluminescence (PL) techniques have been discussed. We have also discussed the effects of ion beam induced strains on frequency shifts of A_1 (LO) and E_2 (high) phonon modes which are parallel and perpendicular to the layer surface. By comparing the frequency shifts of these two phonon modes, we investigated the differences in the effects of ion beam induced strains on these modes. The effects of irradiation and subsequent annealing processes on optical luminescence in GaN films have also been investigated using Photoluminescence (PL) and Photoluminescence excitation (PLE) spectroscopy.

4.2 Experimental details

5 µm thick GaN was grown on sapphire along (0001) oriented substrate by MOCVD technique. AlN as a buffer layer was used between substrate and epilayer to improve structural properties. The GaN sample (2 inch diameter) was cut into small pieces of dimensions about $1 \times 1 cm^2$ for room temperature irradiation. The samples were then mounted on a Cu ladder with a conductive silver paste, and a low beam current of 1 pna for Ag and 1.5 pna for Ni ions was maintained during irradiation to avoid heating effects. Samples were oriented to 7° with respect to the beam axis to avoid any channeling of ions and then irradiated with 80 MeV Ni^{6+} and 100 MeV Ag^{7+} ions at a fixed fluence of 1×10^{13} ions/cm^2 by scanning over $1 \times 1 cm^2$ area using 15 MV Pelletron accelerator at IUAC, New Delhi. From the stopping range of ions in matter (SRIM) code, the range of the ions and electronic energy losses (S_e) for 80 MeV Ni^{6+} and 100 MeV Ag^{7+} were calculated. The corresponding S_e and projected range of ions in GaN for Ni 14 keV/nm and 9.6 µm, and for Ag ions are 22 keV/nm and 8.9 µm, respectively. The projected ion range is larger than thickness of GaN film. Hence, these ions predominantly lose their energy in the electronic stopping power regime, while the ion end-of-range region is deep inside the sapphire substrate. Subsequently, Ni ions irradiated samples were subjected to RTA at 700 °C for 60 sec in Nitrogen atmosphere with a flow rate of 1000 SCCM using RXV6 Rapid Thermal Processor (RTP) system (AET Thermal, Inc) to anneal out non-radiative recombination centers in the samples. Photoluminescence and Photoluminescence excitation characterization techniques have been performed using a Fluorolog-3 (Jobin-Yvon) spectro-fluorometer equipped with a Xenon lamp as excitation source and a monochromator with Photo Multiplier Tube (PMT) system for signal detection and spectral analysis. After ion irradiation, samples were characterized by High Resolution X-ray Diffraction (HRXRD) with Cu K_α radiation (λ = 1.5406 Å) using Bruker D8 DISCOVER. Several symmetric ω and ω –2θ rocking scans were recorded and FWHM extracted. Tilt and defect densities (Screw type) were extracted from Williamson-Hall (W-H) method. Raman scattering measurements were carried out using LabRAM HR800 of Horiba Jobin Yvon. The power of the laser was about 6 mW, and the focused laser spot was about a 3 µm diameter. The spectra were recorded at room temperature in back-scattering geometry with 514.5 nm Argon-ion laser as an excitation source. The scattered light was analyzed by monochromator, equipped with a double notch filter system, and the signal was detected by a Peltier-cooled charge coupled device array.

4.3 Results and discussion

4.3.1 High resolution x- ray diffraction (HRXRD)

(0002) symmetric rocking curves of as deposited GaN (AD GaN) and irradiated GaN are compared in Fig.4. 1. It is observed that irradiation influences the Bragg reflection position of as deposited GaN. Moreover, the shift in Bragg angle is larger for Ag than for Ni ions irradiation, which means lattice parameter increases with increase of electronic stopping power. The lattice parameter c is obtained from the following equation

$$\frac{1}{d_{hkl}^2} = \left(\frac{4(h^2 + k^2 + hk)}{3a^2} + \frac{l^2}{c^2} \right) \tag{4.1}$$

where d_{hkl} is an inter-planar spacing for the corresponding h, k, l miller indices and a, c are lattice parameters of hexagonal crystal.
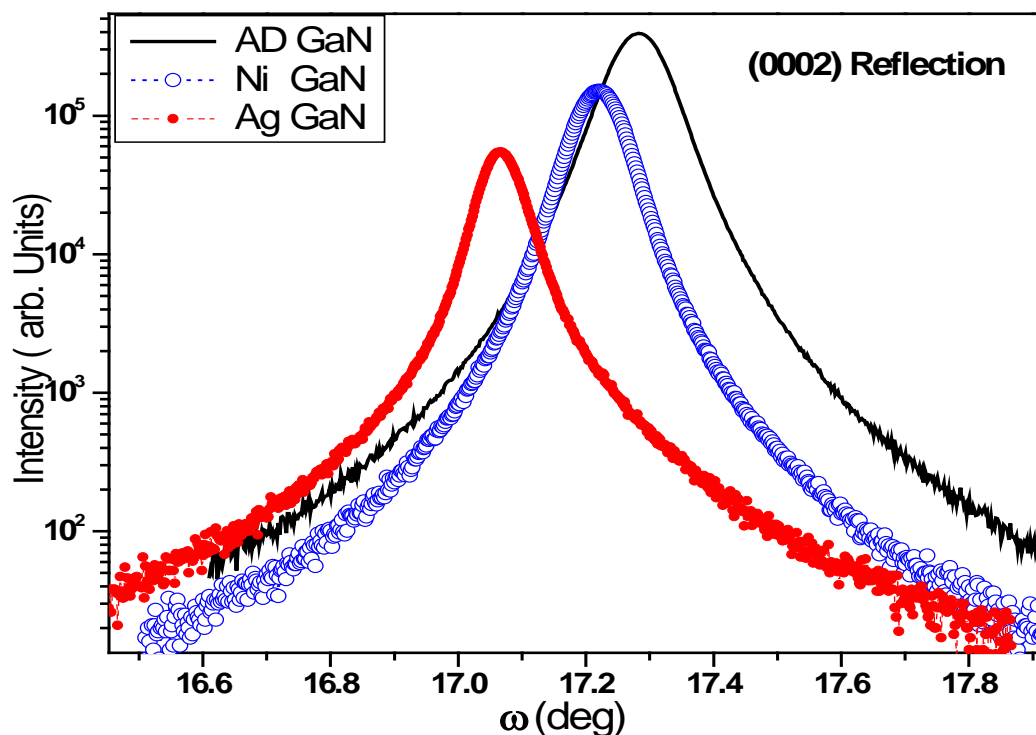
Fig.4.1: ω-scan (rocking curve) of AD GaN and subsequent Ni and Ag ions irradiated GaN .

Using (4.1) lattice parameter 'c' from AD GaN, Ni and Ag ions irradiated GaN have been obtained. Increase in lattice parameter with the irradiation has been noticed which has been attributed to ion induced compressive strain in GaN. The Full width at half maximum (FWHM) of the rocking curves for AD GaN and subsequently for irradiated

GaN with Ni and Ag ions are about 318, 269 and 235 (±10) arc sec, respectively. This shows that irradiation improves structural quality but induces compressive strain into the GaN. This occurs due to intense fast electronic excitations resulting in atomic displacements. This has led to bond-breaking in GaN , which is then followed by certain collective atomic rearrangements due to a transient rise of the lattice temperature to very high values in a very short interval of time.
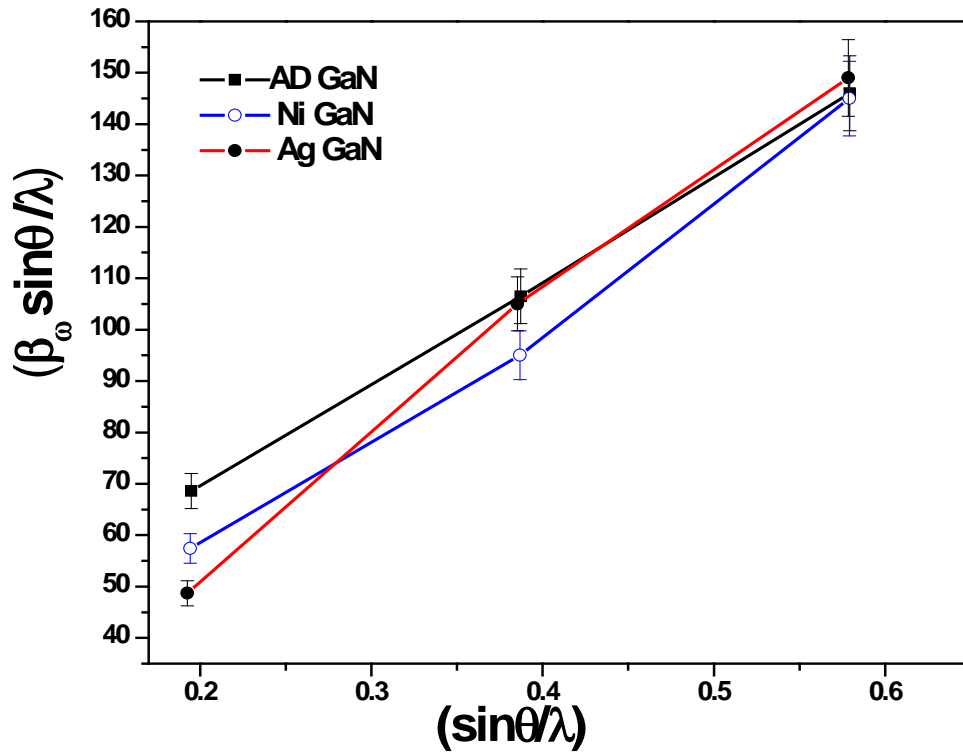
Fig.4.2: Williamson Hall plots for as deposited and subsequent Ni and Ag ions irradiated GaN.

The resulting change of tilt angle with respect to epitaxial crystal generates screw type dislocations. Broadening of angular scan or ω-scan of symmetric reflections (0002), (0004) and (0006) of GaN grown on sapphire are influenced by tilt angle (mis-orientation) [41,42,43].

Further, irradiation induced effects on tilt angles are discussed using Williamson-Hall plots. As shown in Fig .4.2, these are drawn for $\dfrac{\beta_\omega \sin\theta}{\lambda}$ vs $\dfrac{\sin\theta}{\lambda}$ for AD GaN, Ni and Ag ions irradiated GaN samples. Here β is integral line width of measured profile, λ

is X-ray wavelength (0.15406 nm) and 2θ is scattering angle. A linear fit has been performed for set of symmetric reflections in extracting the tilt angle (α) from the slope. The (0002) scan monitors the tilt component of the crystalline structure which strongly associates with dislocations having a screw component, with burger vector b = [0001]. The density of screw dislocations N $_{[0001]}$ can be obtained from the expression [44]

$$N_{[0001]} = \left(\frac{(\alpha)^2}{4.35 \times (b)^2} \right)$$
(4.2)

Where, α is the value of tilt angle and b is Burgers vector's magnitude (0.5185 nm). Thus, the defect densities are calculated using (4.2).

Defect densities for AD GaN, Ni and Ag ion irradiated GaN are found to be 9×10^7, 1.2×10^8 and 1.5×10^8 defects/cm^2, respectively. It is observed that there is a slight increase in defect density upon irradiation.

4.3.2 Raman Spectroscopy

Micro-Raman measurements were performed to obtain a direct evidence of residual strain in GaN. The E_2 (H) mode of AD GaN, Ni and Ag ion irradiated GaN is collected from Raman scattering measurements (see Fig 4. 3). The Raman modes observed from AD GaN sample is in good agreement with the values already reported [45]. The E_2 (H) mode of GaN is very sensitive to biaxial strain in the c plane and this mode gives the strongest signal in the spectra. Due to its non polar nature, E_2 mode is widely used to quantify stress in III- nitrides. The E_2 mode of strain-free GaN is known to be at 567.6 cm^{-1} at room temperature [46, 47]. However, frequency shift can be well used to monitor residual stress [48, 49, 50, 51]. Its phonon frequency is observed at 567.6cm^{-1} and 568.5($\pm$0.05) cm^{-1}, respectively for Ni and Ag ions irradiated GaN. The frequency of E_2 phonon is blue shifted upon Ag irradiation, indicating compressive strain. The shift is attributed to the possibility of compression of c-plane lattice parameter due to irradiation. The width of the strongest mode E_2 (H) can be used to analyze lattice defects [51, 46]. Lattice damage accumulation increases with increase of electronic energy loss (S_e), as can be seen from increase of FWHM of E_2 mode from 5.0 ($\pm$0.1) to 6.21 ($\pm$0.2) cm^{-1}. The A_1(LO) mode depends not only on the residual stress in GaN film but also on the coupling to free carriers (plasmon) of LO mode [52,53]. A_1 (LO) mode, in wurtzite GaN , are sensitive to lattice vibrations along the plane perpendicular to (0001).
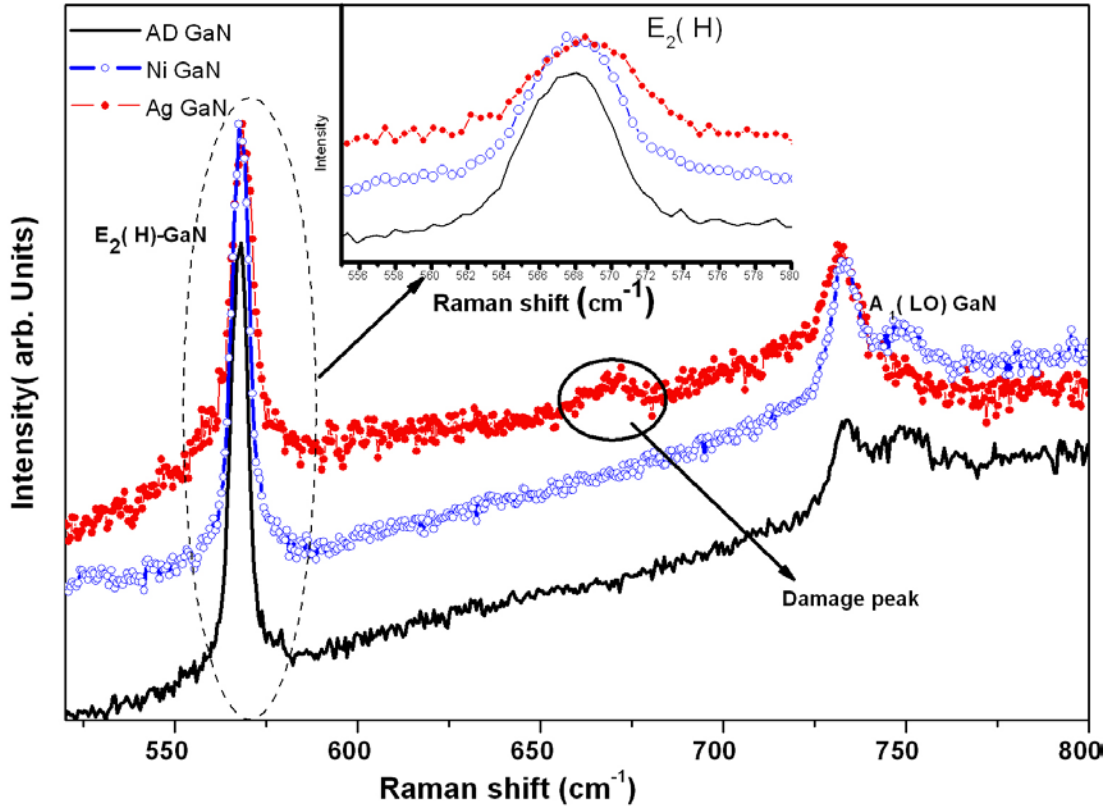
Fig.4.3: Room temperature Raman spectra of E_2 (High) and A_1 (LO) modes from as deposited and subsequent Ni and Ag ions irradiated GaN.

As shown in Fig.4.3, the shoulder peak around 734 cm^{-1} in spectra is not clearly separated from the sapphire peak at 750 cm^{-1}, but its intensity is strong enough so that we can correctly determine its peak position and full width at half maximum. Broadening of A_1(LO) modes can be seen with an increase of S_e.

Wang et. al [54] have shown that increase in FWHM of A_1(LO) mode decreases the carrier concentration with increase of neutron irradiation dosage. In the present case, the variation of the line shape of the A_1(LO) mode is attributed to coupling of this mode with an over damped plasmon [52]. Here, S_e increases this coupling of A_1(LO) mode with an over damped Plasmon. It is known that the plasma mode of a free electron gas can couple with longitudinal optical (LO) phonon lattice vibration mode giving rise to the so called coupled mode closely related to the electron density.
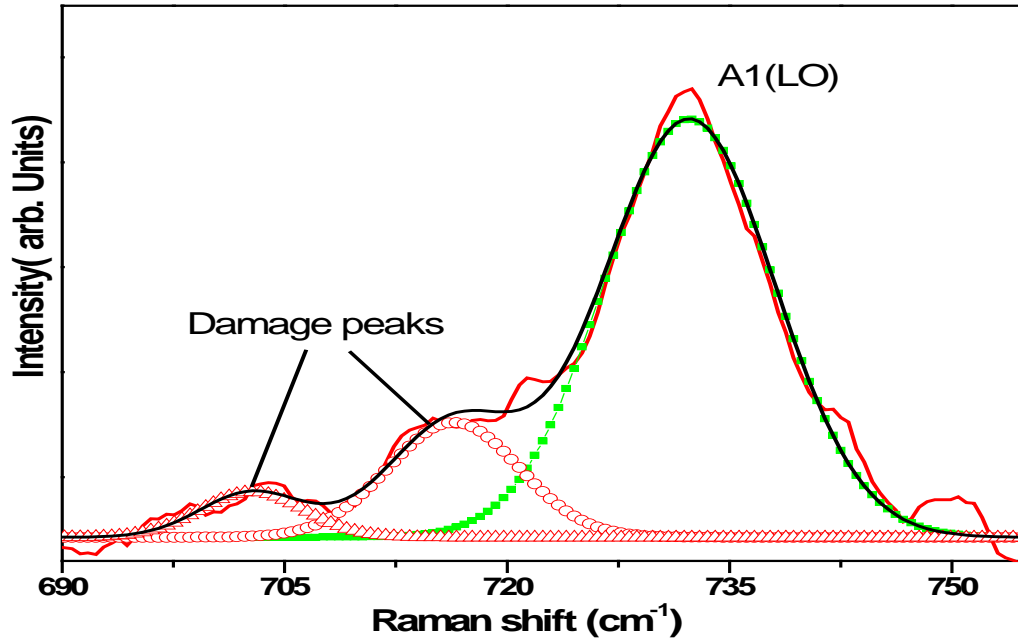
Fig.4.4: Room temperature Raman spectra of A_1 (LO) modes from Ag ion irradiated GaN.

The de-convoluted spectra show damage peaks at 716, and 702 cm^{-1}.The observed mode at 672 cm^{-1} (Fig.4.3) is assigned to local vibrational mode originating from the intrinsic defects such as V_N(nitrogen related defects), which is consistent with implantation of ionic species such as Ar+, Mg+, Ga+ and Cu+ [55]. Fig.4.4 shows de-convoluted Raman spectra of Ag irradiated GaN, which exhibits peaks at 716 and 702 cm^{-1}. These modes are could be due to either V_{Ga} or its complex.

4.3.3 Photoluminescence (PL) and Photoluminescence excitation (PLE) Spectroscopy

PL and PLE measurements have been carried out at room temperature. This study reveals how ion irradiation affects shallow and/or deep level defects in GaN. Observed luminescence by ion irradiation and followed by annealing have been discussed at a greater detail. Room temperature PL spectra of as deposited GaN sample in the ranges of 300-500 nm and 400-750 nm are shown in Fig.4.5 (a) and (b). These plots show the presence of a narrow featured peak at 362 nm and a wide band featured at around 580 nm.Peak at 362 nm is attributed to band to band excitonic recombination linked to GaN,

and the peak at 580 nm could have originated from recombination of distant donor acceptor pairs, which are generally present in GaN as yellow luminescence (YL).
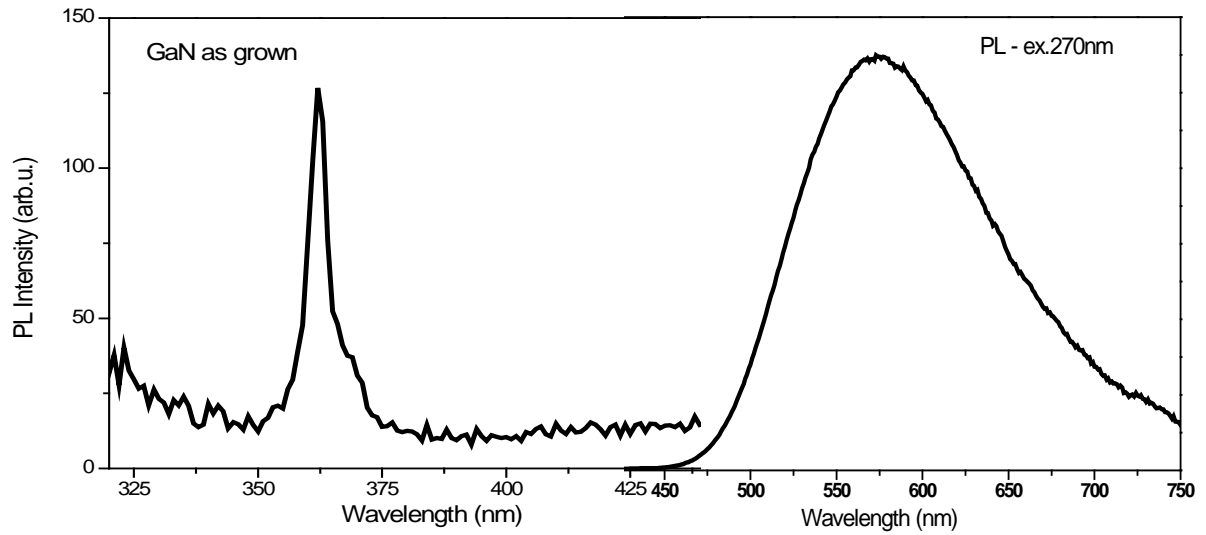
Fig.4.5.a)   Fig.4.5.b)
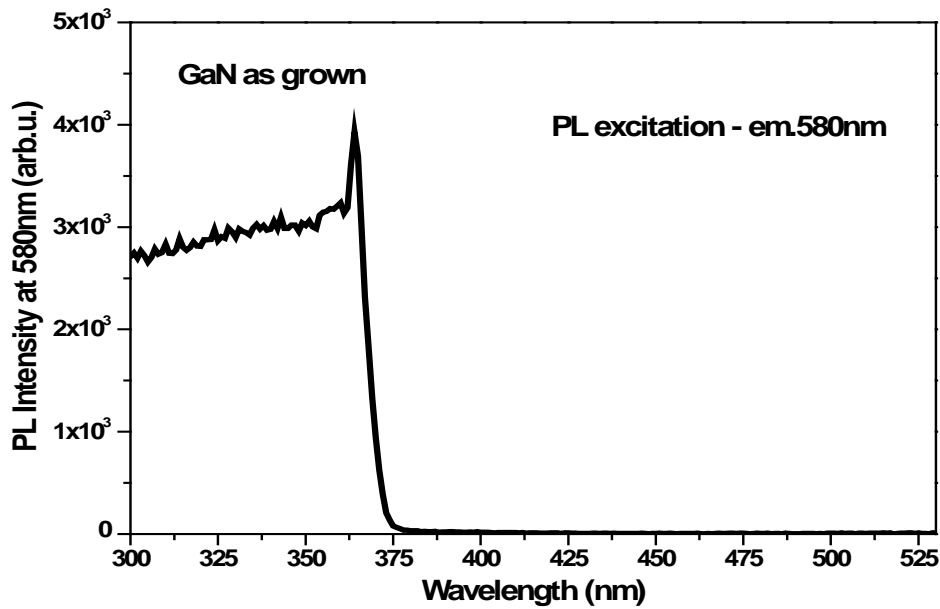
Fig.4.5.c)

Fig.4.5: Photoluminescence spectra collected with Fluorolog-3 (Jobin Yvon) spectro fluorometer with excitation wavelength of 270 nm evidences (a) GaN band to band transitions, (b) unwanted yellow luminescence in the range of 400- 750 nm and (c) PLE spectra with emission at 580 nm shows luminescence activation triggered by photon absorption.

Recent reports on the origin of emission of YL from GaN are attributed to transition from a shallow donor to a deep acceptor level [56], deep donor to shallow acceptor [57]. It is observed that the intensities of band edge and YL band are strongly related to the threading dislocation density of the GaN film [58]. Fig.4.5 (c) shows PLE spectra from pristine GaN , which evidences the presence of band edge around 360 nm (typical GaN energy gap), suggesting a mechanism based on luminescence activation triggered by photon absorption across the semiconductor gap. Fig.4.6 shows PLE spectra of Ni ions irradiated GaN with strong absorption at 450 nm and corresponding Blue luminescence being observed in PL spectra (see Fig. 4.8). This has been attributed to carbon related impurities for band gap ranging from 3 eV to 3.05 eV [59,60,61]. The BL band is also often observed in un-doped, Mg, Si and Zn-doped GaN with very similar shape and position. The reported values of the energy position of the BL band has varied from 2.7 to 3.0 eV. BL emissions were also observed in amorphous GaN nanoparticles embedded in polymer matrix [62]. In the present study, BL band could be attributed to nitrogen related defects.

It seems that a high concentration of radiation annealed gallium vacancies has resulted in quenching of YL band intensity, while the vacancy concentration of nitrogen favors BL band. The later has been evidenced from micro Raman measurements. These are consistent with the fact that an increase of S_e value increases the nitrogen related defect mode intensity. Decrease in YL intensity upon irradiation has been noticed which could be due to annihilation of defects. PL excitation spectra of Ni ions irradiated (and subsequently annealed) GaN are shown in Fig.4.7. This evidences the presence of band edge at around 358 nm (typical GaN energy gap), suggesting a mechanism based on luminescence activation triggered by photon absorption initiated due band to band radaitive transition.

It is evident that defects introduced by irradiation are not completely annealed out. As a result there is no strong evidence of B-B transitions in PL spectra of irradiated and subsequently annealed samples. Fig.4.9 shows YL spectra for as deposited, irradiated, and subsequently annealed GaN samples. PL measurements show the effective reduction in I_{YL} with irradiation and followed by thermal annealing. The schematic energy band diagram of GaN is shown in Fig. 4.10 which clearly shows YL and BL band energy

levels. Decrease in YL intensity has been noticed which can be attributed to substantial reduction in concentration of deep level defects [63] like Ga vacancies [64].
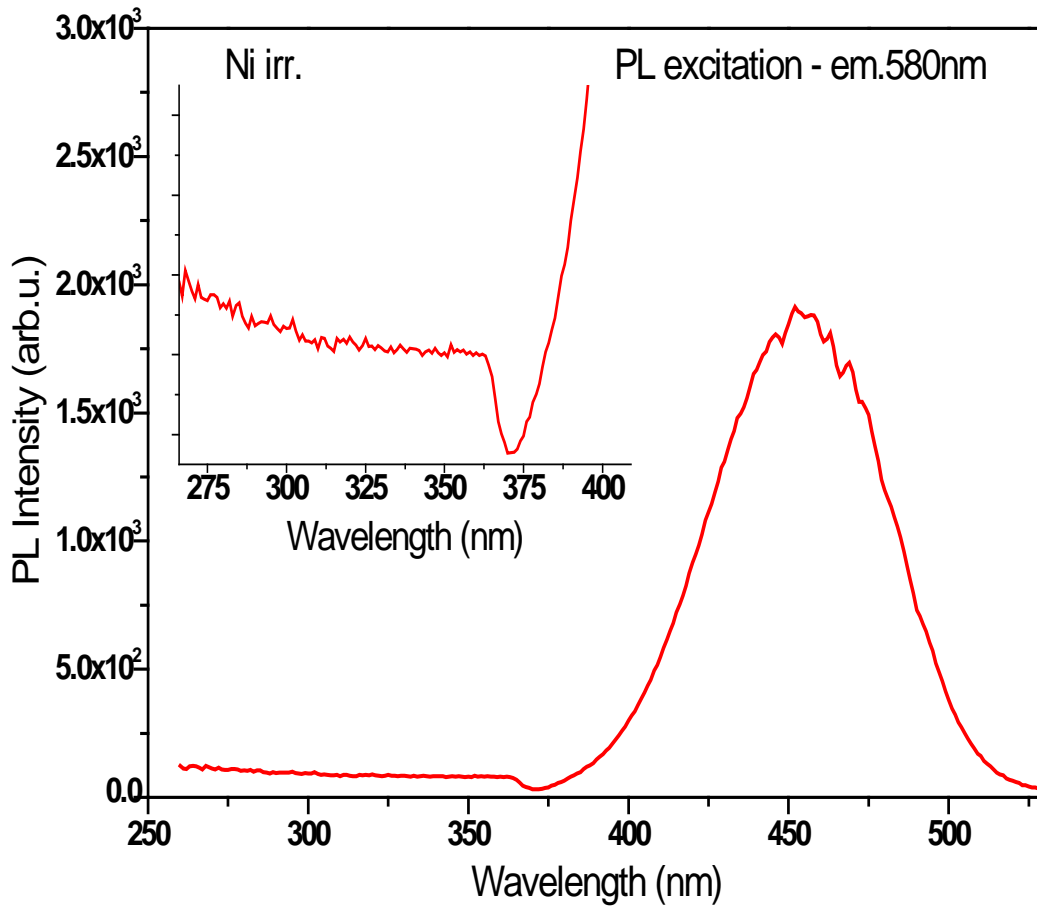
Fig. 4.6: PLE spectra of Ni irradiated GaN shows absorption at 2.8 eV

In the present study, we see that SHI lose energy predominantly to target electrons. As a consequence, the intrinsic point defects like V_{Ga} or their complex defects from dislocation core, are annealed out which perhaps strongly decreases intensity of YL emissions. Since annealing temperature is rather low hence it may be assumed that the defects introduced by irradiation are not totally annealed out. In such a case the non-radiative recombination rate is higher than that of pristine sample. As a result, the intensity of YL emission band decreases. Therefore, it is assumed that the BL and YL are associated with irradiation induced N defects, and native Ga vacancies.
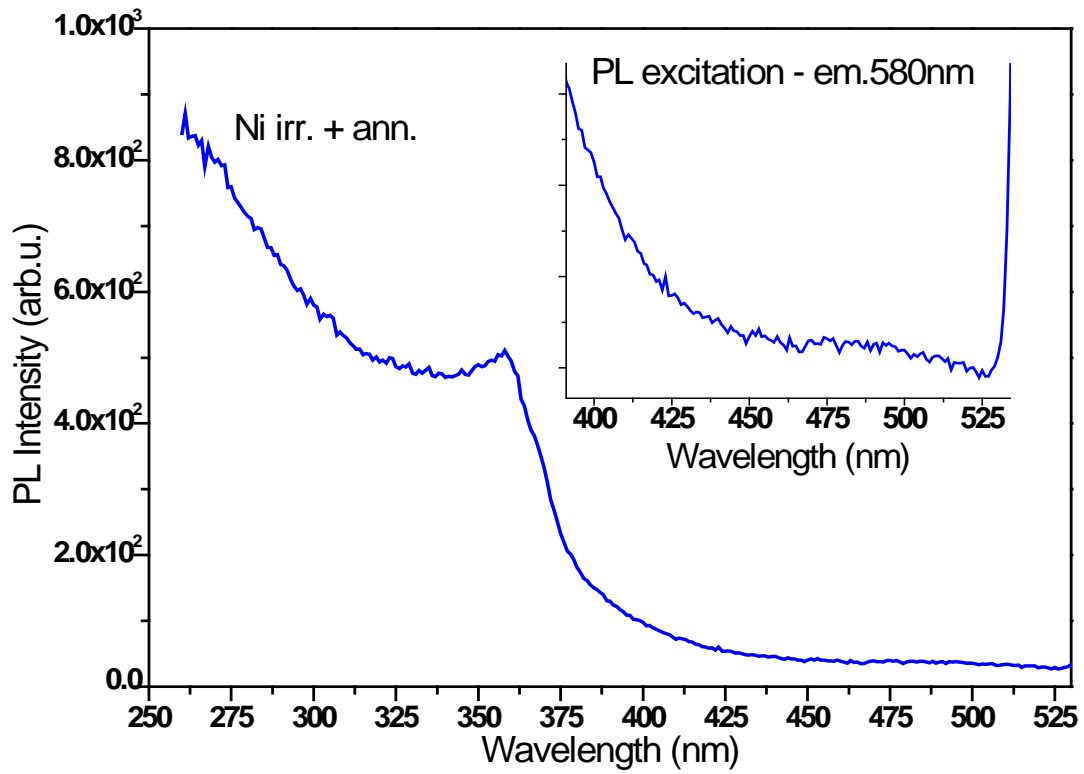
Fig.4.7: PLE spectra of Ni ions irradiated GaN and subsequently annealed at 700 °C in N_2 atmosphere for 60 sec has resulted no absorption but increased band to band transitions.
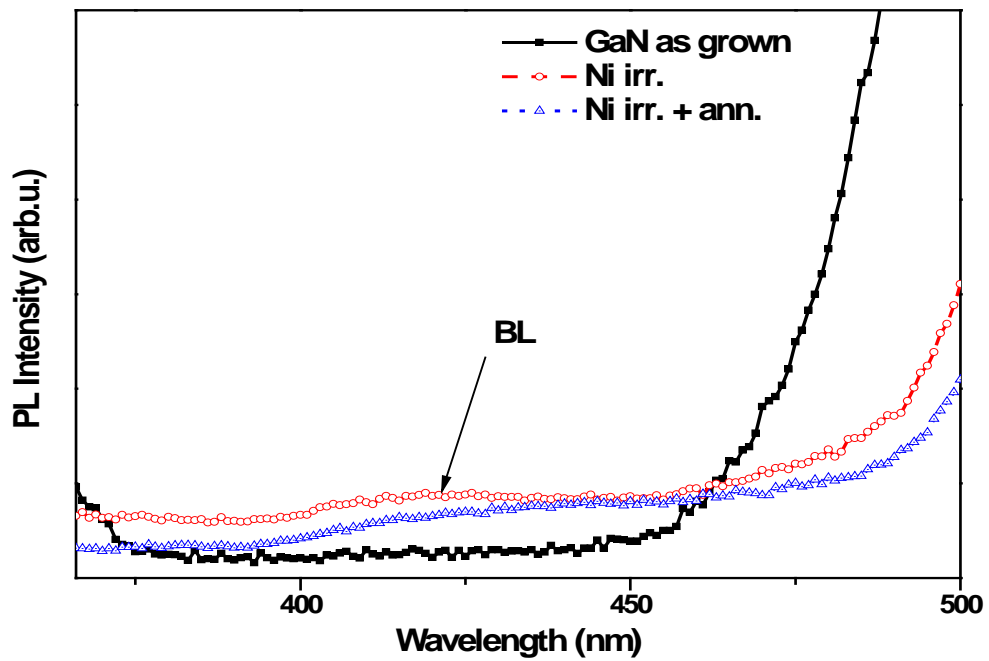
Fig.4.8: Photoluminescence spectra of Blue luminescence from pristine, Ni irradiated and subsequently annealed samples.
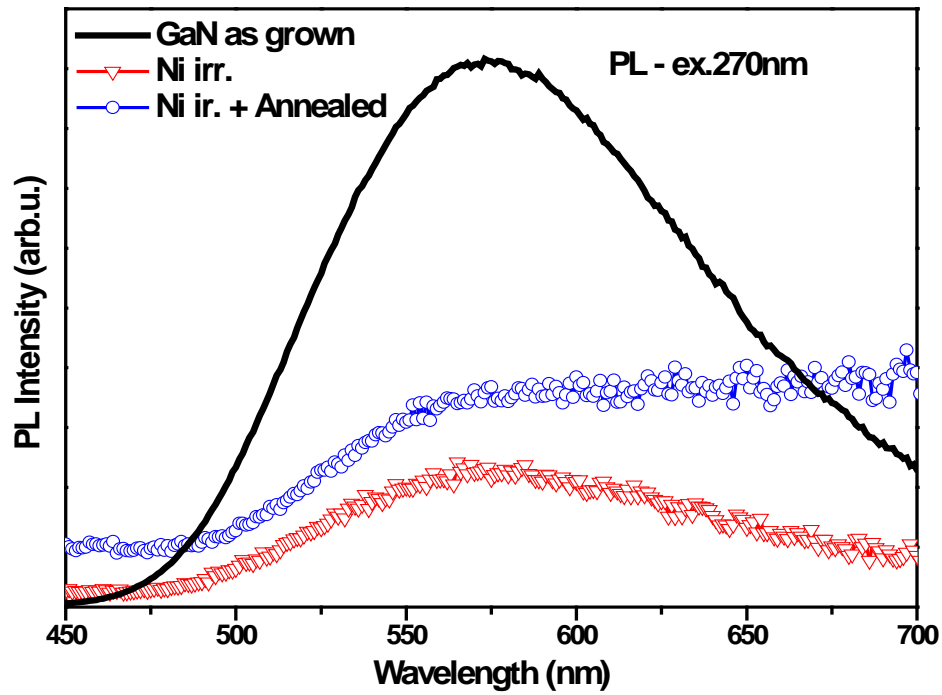
Fig.4.9: Room temperature PL spectra collected from the pristine, irradiated and subsequently annealed GaN samples show decrease in YL intensity around 2.2 eV.
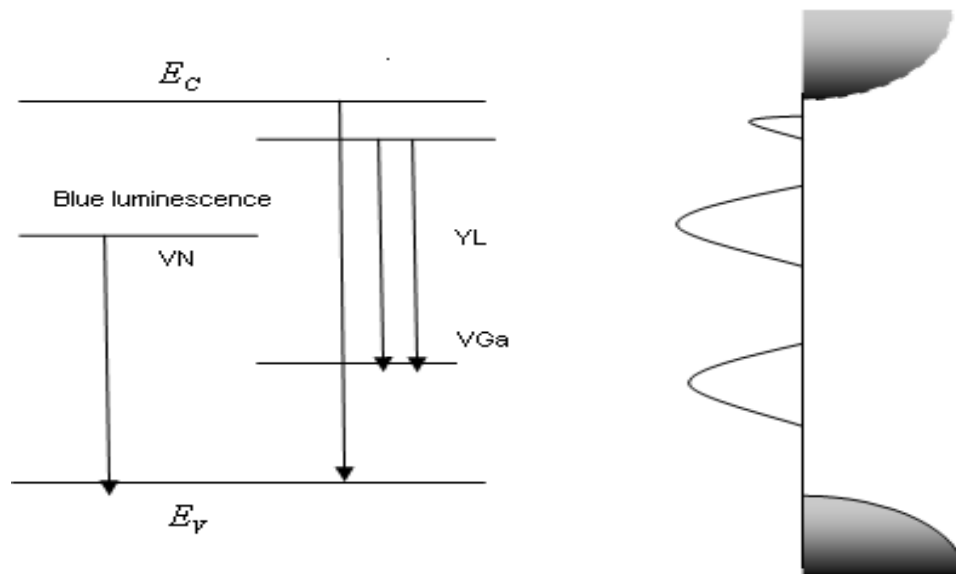
Fig.4.10: Schematic energy diagram of as deposited and irradiated GaN is depicted for corresponding transitions with possibility distribution given on the right side.

4.4. Conclusions

MOCVD grown GaN samples were irradiated with Ni and Ag ions at a fixed fluence. Structural and optical characterizations have been investigated as a function of electronic stopping power by HRXRD, micro-Raman and photoluminescence measurements. Increase in crystalline nature, and lattice swelling in growth direction upon irradiation has been noticed from decrease of FWHM and shift in Bragg's peak to lower angles. It is evident that the irradiation influences lattice parameters and consequently phonon modes. Defect densities are also calculated using W-H plots, which show that irradiation, leads to slight increase in defect densities. Raman studies yield E_2 modes that are sensitive to local strain and consequent blue shift in E_2 mode for higher S_e value is attributed to compressive strain which is consistent with observed HRXRD results. The variation of the line shape of the A_1(LO) mode of GaN with S_e is basically due to the coupling of A_1(LO) mode with an over damped plasmon. Therefore it was concluded that as S_e increases, coupling of A_1(LO) mode with an over damped Plasmon increases. This may be due to transient rise in lattice temperature by heavy ion bombardment to very high values in a very short interval of time, leading to certain collective atomic rearrangements.

PL and PLE studies have been carried out on as deposited, Ni ions irradiated and subsequently annealed GaN samples. Band to band transitions are noticed from pristine sample but there is no evidence of B-B on irradiated GaN. It shows BL band at 450 nm besides YL emissions from Ni ions irradiated GaN. It seems that a high concentration of radiation annealed gallium vacancies have a quenching effect on YL emission intensity while the vacancy concentration of nitrogen favors BL. In the present study, we can speculate that BL band is due to nitrogen related defects. Irradiated and subsequently annealed GaN shows existence of B-B transitions besides intra-gap defects' level transitions. PL measurements show the effective reduction in YL intensity with irradiation and subsequent thermal annealing. This can be considered as substantial reduction in concentration of deep level defects like Ga vacancies due to transfer of heavy ions energy to target electrons. As a consequence, intrinsic point defects like V_{Ga} or their

complexes are annealed out along the ion trajectory. Therefore, it is assumed that the BL and YL are associated with N and Ga vacancies, respectively.

4.5 References

1. H Amano, K Hiramatsu, and I Akasaki, Jpn. J. Appl. Phys. 27, 1384 (1988)

2. C Kisielowski, J Kr_ger, S Ruvimov, T Suski, J W Anger III, E Jones, Z Liliental-Weber, M Rubin, E R Weber, M D Bremser, and R F Davis, Phys. Rev. B 54, 17745 (1996)

3. I A Buyanova, J P Bergman, B Monemar, H Amano, and I Akasaki, Appl. Phys. Lett. 69, 1255 (1996)

4. V Yu Davydov, N S Averkiev, I N Goncharuk, D K Nelson, I P Nikitina, A S Polkovnikov, A N Smirnov, and M A Jacobson, J. Appl. Phys. 82, 5097 (1997)

5. T Kozawa, T Kachi, H Nagase, N Koide, and K Manabe, J. Appl. Phys. 77, 4389 (1995)

6. F Demangeot, J Frandon, M A Renucci, O Briot, B Gil and R L Aulombard, Solid State Commun. 100, 207 (1996)

7. N A Mahadik, S B Qadri, and M V Rao, Appl. Phys. Lett. 93, 222106 (2008)

8. M Aziz and T Palacios, J. Appl. Phys. 108, 023707 (2010)

9. M Linde, S J Uftring, G D Watkins, V Harle, and F Scholz, Phys. Rev. B 55, 10177 (1997)

10. I A Buyanova, Mt Wagner, W M Chen, B Monemar, J L Lindstrom, H Amano, and I Aksaki, Phys. Scr. T79, 72 (1999)

11. A Nakanishi, A Wakahara, H Okada, A Yoshida, T Ohshima, and H Itoh, Appl. Phys. Lett. 81, 1943 (2002)

12. I A Buyanova, Mt Wagner, W M Chen, B Monemar, J L Lindstrom, H Amano, and I Akasaki, Appl. Phys. Lett. 73, 2968 (1998)

13. N M Schmidt, P S Vergeles , E E Yakimov, and E B Yakimov, Solid State Commun. 151, 208 (2011)

14. P Premchander and K Baskar, J. Mater Sci, 45, 6799 (2010)

15. M Coeck, N Balcaen, T Van Hoecke, B Van Waeyenberge, D Segers, C Dauwe, and C Laermana, J. Appl. Phys. 87, 3674 (2000)

16. G Williams, J U Patel, A M Ougouag, and S Y Yang, J. Appl. Phys. 70, 4931 (1991)

17. G E Brehm and G L Pearson, J. Appl. Phys. 43, 568 (1972)

18. M Satoh, K Kuriyama, and T Kawakubo, J. Appl. Phys. 67, 3542 (1990)

19. M Palczewska, J Jasinski, K Korona, M Kaminska, E D Bourrent, and A G Elliot, J. Appl. Phys. 78, 3680 (1995)

20. B Mari, M A Hernandez-Fenollosa, and F J Navarro, J. Appl. Phys. 89, 7772 (2001)

21. O Herre, W Wesch, E Wendler, P I Gaiduk, F F Komarov, S Klaumünzer, and P Meier, Phys. Rev. B 58, 4832 (1998)

22. N Sathish, PhD thesis submitted to University of Hyderabad, India (2009)

23. C S Schnohr, P Kluth, R Giulian, and D J Llewellyn, A P Byrne, D J Cookson, M C Ridgway, Phy. Rev. B 81, 075201 (2010)

24. W Wesch, A Kamarou, E Wendler, and S Klaumünzer, Nucl. Instr. and Meth. B 242, 363 (2006)

25. K Kuriyama, T Tokumasu, J Takahashi, H Kondo, and M Okada, Appl. Phys. Lett. 80, 3328 (2002)

26. C W Wang, J. Vac. Sci. Technol. B 20, 1821 (2002)

27. S O Kucheyev, J S Williams and S Pearton, J Mat. Sci. Eng. R 33, 51 (2001)

28. S O Kucheyev, H J Timmers Zou, J S Williams, C Jagadish and G Li, J. Appl. Phys. 95, 5360 (2004)

29. W Jiang, W J Weber, M Wang and K Sun, Nucl. Instr. and Meth. B 218, 427 (2004)

30. V Suresh Kumar, J Kumar, D Kanjilal, K Asokan, T Mohanty, A Tripathi, Francisca Rossi, A Zappettini, and L Lazzarani, Nucl. Instr. and Meth. B 266, 1799 (2008)

31. N Sathish, S Dhamodaran, A P Pathak, M Ghanashyam Krishna, S A Khan, D K Avasthi, A Pandey, R Muralidharan, G Li, and C Jagadish, Nucl. Instr. and Meth. B 256, 281 (2008)

32. A Kamarou, W Wesch, E Wendler, and S Klaumünzer, Nucl. Instr. and Meth. B 225, 129 (2004)

33. D C Look, D C Reynolds, J W Hemsky, J R Sizelove, R L Jones, and R J Molnar, Phy. Rev. Lett. 79, 2273 (1997)

34. W H Sun, J C Zhang, L Dai, K M Chen, and G G Qin, J. Phys. Condens. Matter 13, 5931 (2001)

35. Z Q Fang, J W Hemsky, D C Look, and M P Mack, Appl. Phys. Lett. 72, 448 (1998)

36. I A Buyanova, Mt Wagner, W M Chen, B Monemar, J L Lindstrom, H Amano, and I Aksaki, Appl. Phys. Lett. 73, 2968 (1998)

37. F D Auret, S A Goodman, F K Koschnick, J M Spaeth, B Beaumont, and P Gibart, Appl. Phys. Lett. 74, 407 (1999)

38. W Wesch, A Kamarou, and E Wendler, Nucl. Instr. and Meth. B 225, 111 (2004)

39. H Boudinov, S O Kucheyev, J S Williams, C Jagadish, and G Li, Appl. Phys. Lett. 78, 943 (2001)

40. S O Kucheyev, J S Williams, J Zou, and C Jagadish, J. Appl. Phys. 95, 3048 (2004)

41. S R Lee, A M West, A A Allerman, K E Waldrip, D M Follstaedt, P P Provencio, D D Koleske and C R Abernathy, Appl. Phys. Lett. 86 ,241904(2005)

42. T Metzger, R Hopler, E Born, O Ambacher, M Stutzmann, R Stommer, M Schuster, H Gobel, S Christiansen, M Albrecht and H P Strunk, Phil. Mag. A 77, 1013 (1998)

43. M A Moram and M E Vickers, Rep. Prog. Phys. 72 ,036502 (2009)

44. P Gay, P B Hirsch, and A Kelly, Acta. Metall. 1, 315 (1953)

45. G H Li, W Zhang, H X Han, Z P Wang and S K Daun, J. Appl. Phys. 86, 2051 (1991)

46. T Kitamura, S Nakashima, N Nakamura, K Furuta and H Okumura, Phys. Stat. Sol. (c) 5, 6 , 1789(2008)

47. V Yu Davydov, Yu E Kitaev, I N Goncharuk, A N Smirnov, J Graul, O Semchinova, D Uffmann, M B Smirnov, A P Mirgorodsky and R A Evarestov, Phys. Rev. B 58, 12899 (1998)

48. T Inoue, Y Toda, K Hoshino, T Someya and Y Arakawa, Phys. Stat. Sol. (c) 0 No. 7 2428 (2003)

49. H J Park, C Park, S Yeo, S W Kang, M Mastro, O Kryliouk, and T J Anderson, Phys. Stat. Sol. (c) 2, No. 7, 2446 (2005)

50. C Kisielowski, J Kr ¨ uger, S Ruvimov, T Suski, III JW Ager, E Jones, Z Liliental-Weber, M Rubin, E R Weber, M D Bremser, R F Davis, Phys. Rev. B 54, 17745 (1996)

51. D Y Song, M Basavaraj S A, Nikishin, M Holtz, V Soukhoveev, A Usikov and V Dmitriev, J. Appl. Phys. 100, 113504 (2006)

52. T Kozawa, T Kachi, H Kano, Y Taga, and M Hashimoto, N Koide and K Manabe, J. Appl. Phys. 75 , 1098 (1994)

53. M Kuball, Surf. Interface Anal. 31 , 987–999(2001)

54. R X Wang, S J Xu, S Fung, C D Beling, K Wang, S Li, Z F Wei, T J Zhou, J D Zhang, Ying Huang, M Gong , Appl. Phys. Lett. 87, 031906 (2005)

55. W Limmer, W Ritter, R Sauer, B Mensching, C Liu, and B Rauschenbach, Appl. Phys. Lett. 72, 2589 (1998)

56. T Ogino and M Aoki, Jpn. J. Appl. Phys. 19, 2395 (1980)

57. E R Glaser, T A Kennedy, K Doverspike, L B Rowland, D K Gaskill, J A Freitas Jr., M Asif Kahn, D T Olson, J N Kuznia and D K Wickenden, Phys. Rev. B 51, 13326 (1995)

58. J Oila, J Kivioja, V Ranki, K Saarinen, D C Look, R J Molnar, S S Park, S K Lee, and J Y Han, Appl. Phys. Lett. 82, 3433 (2003)

59. M A Reshchikov and H Morkoç, J. Appl. Phys. 97 , 061301 (2005)

60. M A Reshchikov and R Y Korotkov, Phys. Rev. B 64, 115205 (2001)

61. A Y Polyakov, M Shin, J A Freitas, Jr., M Skowronski, D W Greve, and R G Wilson, J. Appl. Phys. 80, 6349 (1996)

62. Yi Yang, Valerie J. Leppert, Subhash H. Risbud, Brendan Twamley , Phillip P. Power Howard, and W. H. Lee, Appl. Phys. Lett. 74, 2262 (1999)

63. C B Soh, S J Chua, H F Lim, D Z Chi, S Tripathy, and W Liu, J. Appl. Phys. 96, 1341 (2004)

64. K Saarinen, T Laine, S Kuisma, J Nissilä, P Hautojärvi, L Dobrzynski, J M Baranowski, K Pakula, R Stepniewski, M Wojdak, A Wysmolek, T Suski, M Leszczynski, I Grzegory, and S Porowski, Phy. Rev. Lett. 79 , 3030 (1997)

Swift heavy ion induced effects in MOCVD grown AlGaN/GaN MQWs

5.1 Introduction

Multilayer hetero-structures are very important for several applications such as quantum-well lasers, tunneling devices, access-memory devices and high-electron mobility transistors. GaN based materials can withstand high temperatures and high pressures rendering GaN-based electronic materials ideal for space applications [1,2]. These materials have been realized with the advent of novel growth techniques like Molecular Beam Epitaxy (MBE) and Metal Organic Chemical Vapour Deposition (MOCVD) with nanoscale precision to reveal their quantum effects. Elastic strain at the interface due to the mismatch in actual structures can be altered with respect to relaxed mismatch, i.e. the one that would be measured if the substrate and the epilayers do not interact. Such a strain is an important parameter in altering the band gap of GaN based materials [3, 4]. There is a critical thickness beyond which the layers become progressively more reluctant to distort, and strain relaxes by creation of defects, which in turn degrade the device performance. This requires the epilayer to be less than critical layer thickness for effective performance of devices. Restrain on layer thickness and its consequent effects have been partially resolved by introducing AlN and GaN buffer layers between substrate and epilayers. Further, Nakamura et al [5] have observed the effects of GaN buffer layer on the growth of InGaN/GaN Multi Quantum Wells (MQWs) as active layers for blue laser diodes. Wei et al [6] observed good crystallinity of InGaN/GaN MQWs grown on partially relaxed GaN layer, irrespective of large lattice mismatch and thermal incompatibility with underlying substrate. Yoshida et al [7] have used AlN as a buffer layer between substrate and epilayer, and found an improvement in the optical properties. Eventually AlN as a buffer layer has a significant influence on the crystal quality, strain, interface and surface properties of AlGaN/GaN heterostructures [8]. In the present work, alternating band gap materials were grown on buffer layers (AlN and GaN) with sufficiently thick barrier layer such that the charges are confined only in wells. Owing to their extraterrestrial applications, there is a need to understand the device performance of these semiconductor materials under radiation treatment. In this direction, there is very limited amount of research effort in the published literature, but it has been established that high-energy ions can create carrier traps to compromise electrical and optical

properties [9, 10]. Moreover, a variety of effects can occur in the materials due to the rapid energy transfers [11]. Most of the high-energy irradiation results were understood by exploiting the concepts of defects [12,13] and phonon deformations. Under MeV ion bombardment, it is reported that ion beam induced intermixing can help to tailor the band gap of MQWs [14] which underlines the importance to investigate the effects of swift heavy ion irradiation on interfaces of multi layer systems.

In this study, 200 MeV Au ions at a fixed fluence of 5×10^{11} ions/cm^2 were used for bombardment. In this regime, dynamic annealing process has been reported due to intense ultra fast excitation of core and valence electrons occurring along the ion paths [15]. We have also investigated effects of electronic energy loss (80 MeV Ni and 120 MeV Au ions) at a fixed fluence of 1×10^{12} ions/cm^2 in Al$_x$Ga$_{(1-x)}$N/GaN MQWs on structural properties which includes interface quality, defects (creation or annihilation), composition and strain. These MQWs were imaged by High Angle Annular Dark Field - Scanning Transmission Electron Microscopy (HAADF-STEM) and the results were compared and verified by high resolution X-ray diffraction (HRXRD).Type of defects at various interfaces have been analyzed using micro diffraction images. Symmetric and asymmetric Reciprocal Space Mapping (RSM) using HRXRD, and Photoluminescence (PL) measurements were carried out for direct evaluation of local strain state as well as composition and band gap of MQWs. Micro-Raman measurements [16-18] were also carried out to understand irradiation effects on strain and free carrier concentration of GaN vibrational modes.

5.2 Experimental details

15 Periods of AlGaN/GaN MQWs (Sample ID as 1473_AD) were grown on C-sapphire using an MOCVD system equipped with a horizontal quartz reactor at ITME Warsaw, Poland. AlN and GaN were grown as nucleation layers with a thickness of 20 nm and 200 nm between substrate and epilayers. The samples were cut into 1x 1cm^2 pieces and mounted on a Cu ladder orienting these at an angle of 7° with respect to the beam axis to avoid channeling of ions. Subsequently, these samples were irradiated with 80 MeV Ni (Sample ID as 1473_Ni) and 120 MeV Au (Sample ID as 1473_Au) ions at a fixed fluence of 1×10^{12} ions/cm^2 by scanning over the 1x 1cm^2 area using the 15 MV Pelletron accelerator at IUAC, New Delhi. The stopping range of ions in matter (SRIM) code was

used to calculate the electronic energy loss (S_e) and nuclear energy loss (S_n) and projected range for 80 MeV Ni and 120 MeV Au ions in MQWs. In the present study, S_e and S_n for 120 MeV Au ions in MQWs are 25 keV/nm and 0.48 keV/nm, respectively. Similarly, S_e and S_n for 80 MeV Ni ions in MQWs are 13 keV/nm and 0.03 keV/nm, respectively. The pristine and the irradiated samples were characterized by Raman spectroscopy, HRXRD and HAADF-STEM for vibrational modes and interface quality. Raman spectra were recorded in backscattering geometry, with an excitation wavelength of 514.5 nm at a power of 40 mW by a Jobin-Yvon T64000 triple spectrometer equipped with a Peltier-cooled charged-coupled device (CCD) detector at room temperature. Specimens for cross-sectional transmission electron microscopy (TEM) analysis were prepared by mechanical polishing, followed by argon ion milling using a Gatan PIPS system at an angle of 3º and a voltage of 5 kV or using a FEI Strata 400 S DualBeam FIB with in-situ lift-out. HAADF-STEM, high resolution TEM, and qualitative energy dispersive X-ray (EDX) nano analysis were performed using a FEI Titan 80-300 equipped with an objective lens aberration corrector. The microscope was operated at 300 kV providing a resolution of 0.08 nm in TEM mode and 0.14 nm in STEM mode. The HAADF-STEM images were recorded with a camera length of 196 mm and a convergence angle of 9.5 mrad. All the HAADF-STEM and HRTEM images presented in this paper are raw images only adjusted for contrast, brightness and gamma. HRXRD measurements were done with Cu Kα radiation (λ = 1.5406 Å) using a Bruker D8 DISCOVER. Several symmetric ω and ω-2θ rocking scans were recorded for strain and compositional analysis.

5.3 Results and discussion

5.3.1 High resolution x- ray diffraction (HRXRD)

Fig.5.1 shows the experimental diffraction pattern (curve) for (0002) reflection of AlGaN/GaN MQWs with simulated curve based on dynamical theory. The measured curve exhibits five peaks indicating good layer periodicity. It is also evident from the Fig.5.1 that intensity integration is due to a wide open detector slit. Measured (0002) reflection with detector slit of $1/8^{\circ}$ has been compared with simulation based on dynamical theory based Philip's epitaxy software. As shown in Fig.5.1, the simulated scan matches reasonably well with measured ω-2θ scan by optimizing lattice relaxation, composition and thickness of the well and barrier by trial and error method.

Fig.5.1: Experimental high resolution XRD scan in $\omega - 2\theta$ configuration for the symmetrical (0002) reflection with detector slit of $1/8^0$

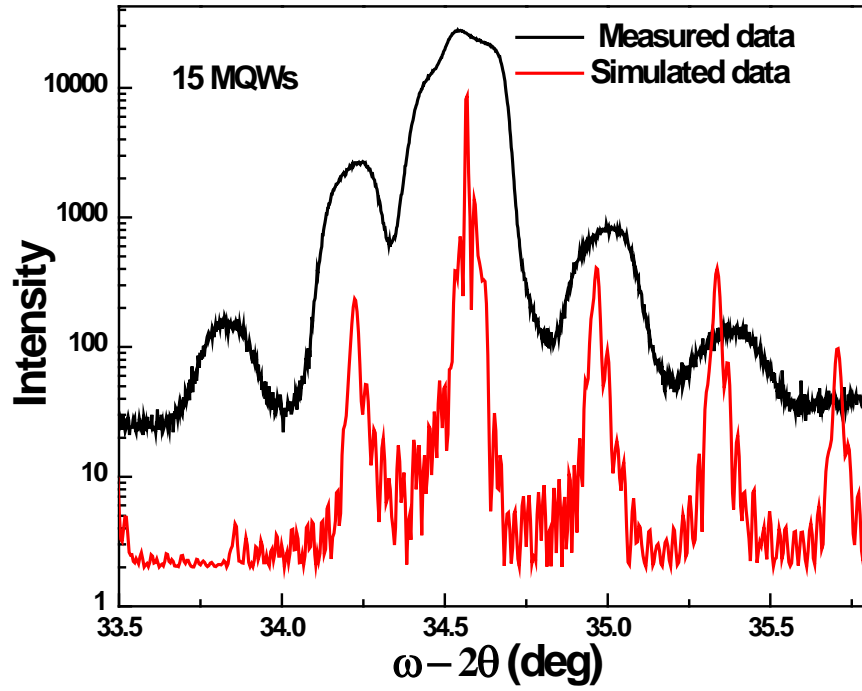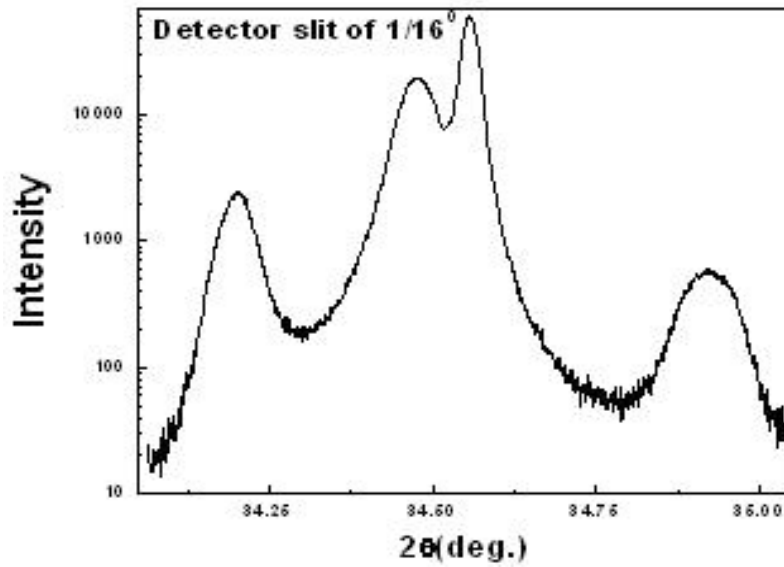**Fig.5.2:** Experimental high resolution XRD scan in $\omega - 2\theta$ configuration for symmetrical (0002) reflection with detector slit of $1/16^0$. This narrower detector has well resolved satellite peaks.

Different ω-2θ scans were measured as a function of different detector slits and measuring times to better resolve satellite peaks like the one shown in Fig. 5.2.

The angular positions of all the satellite peaks with respect to GaN reflection from symmetric and asymmetric reflections are measured. Such measured angular positions corresponding to different reflections from Fig.5.2 and Fig.5.3 are then substituted in Bragg's law to estimate strain,

$$\frac{\Delta d}{d} = -\cot\theta \cdot \Delta\theta \qquad (5.1)$$

where $\Delta\theta$ is angular separation between substrate peak and satellite peak. The estimated strain values have been compared to identify the 0th order peak [19] (the average lattice mismatch, $<\Delta d/d>$, has same value for all reflections). Since such measured strain values have remained unchanged for one of the satellite peaks for symmetric as well as asymmetric reflection, it has been possible to identify the 0th order satellite peak.
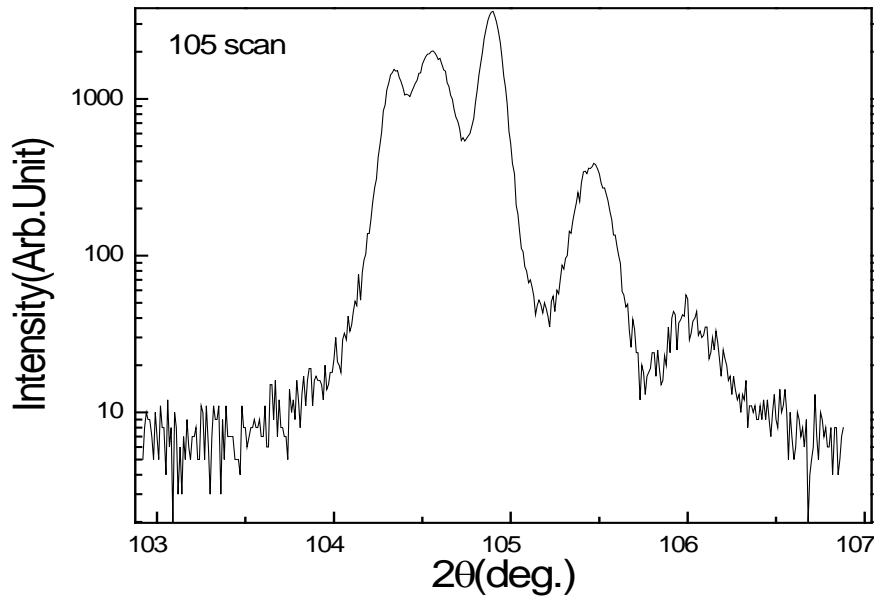
Fig.5.3: Experimental high resolutions XRD scan in $\omega - 2\theta$ configuration for asymmetrical (10-15) reflection.

Essentially, 0th order peak gives average strain in multi quantum wells [20]. The thickness of each period $(D = d_w + d_b)$ is measured using the formula

$$D = \frac{(L_i - L_j)\lambda}{2(\sin\theta_i - \sin\theta_j)} \qquad (5.2)$$

where L_i, L_j are diffraction order indices and θ_i and θ_j are corresponding peak postions and λ is wavelength of Cu $K_{\alpha 1}$ radiation (1.5406 Å). The extracted period, D, using

79

equation (5.2), is found to be 25 nm. The average chemical Aluminum composition <x>, estimated using Vegard's law, is found to be 0.25. Eventually, the obtained thickness of each well and barrier are consistent with simulations.

5.4 HRXRD and PL results of 200 MeV Au ions (5×10^{11} ions/cm^2) irradiated AlGaN/GaN multi quantum wells

High precision RSM measurements have been carried out for estimating and comparing strain for both as grown and irradiated samples.

Table.5.1: Relative mismatch and super lattice periods are extracted from Symmetrical Reciprocal Space Mappings

	As grown	Irradiated
$a_\perp$ (GaN)$= c_{\perp s}$	(5.1893 ± 0.0001) Å	(5.1894 ± 0.0001) Å
$a_\perp$ (MQW) $= c_{\perp l}$	(5.1777 ± 0.0001) Å	(5.1764 ± 0.0001) Å
Relative perpendicular mismatch: $\dfrac{c_{\perp L} - c_{\perp s}}{c_{\perp s}}$	-2.24×10^{-3}	-2.52×10^{-3}
MQW period	(0.02570 ± 0.003) µm	(0.0250 ± 0.001) µm

Figures 5.4 (a) and (b) and Figures 5.5 (a) and (b) show the reciprocal maps of the as grown and irradiated samples. The spread of diffraction intensity over a wider range is related to the orientation distribution and decrease in coherency of the scattering vector along the structure, indicating mosaic nature. The satellite peaks are aligned in the same direction relative to the GaN surface normal, confirming that the strained layers have grown essentially pseudomorphic to the GaN layer. Therefore, the MQW structure is almost fully strained.

The extracted details from the analysis of these data are given in Table.5.1. Irradiation has slightly increased the lattice mismatch by causing the decrease of epi-layer lattice parameter. It is also observed from maps that the intensity of satellite peaks increases

upon irradiation, which can be due to annihilation of defects. In addition, a reduction of the width of the satellite peaks as a consequence of the irradiation indicates that the irradiated sample has a more regular periodicity than the unirradiated samples.

Moreover, as shown in Fig.5.5.a and 5.5.b, the asymmetric maps show a slight relaxation after the irradiation. At the same time, the parallel separation in reciprocal space between the substrate peak and the 0th order peak passes from $5.1 \times 10^{-4} \text{Å}^{-1}$ to $10.3 \times 10^{-4} \text{Å}^{-1}$.
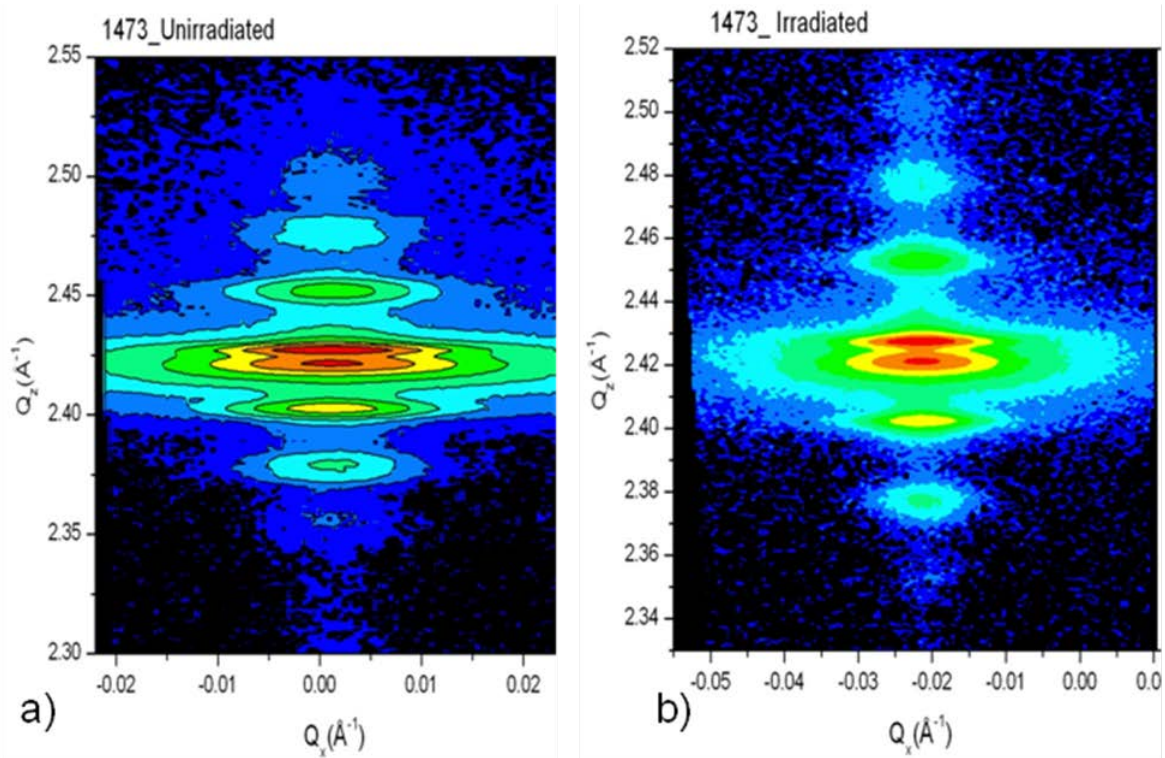
Fig.5.4: RSM taken along (0002) GaN reflection a) as grown and, b) irradiated sample.

Fig. 5.6 shows the low temperature photoluminescence spectra for GaN. Due to the lattice relaxation defect states are insensitive, PL emission at -251^{0}C have shown a good luminescence peak at 3.4 eV. RT-Photoluminescence spectrum of pristine MQWs exhibits no yellow luminescence, while the irradiated MQWs shows increase in yellow luminescence signal towards Infrared (IR) region. As shown in Fig. 5.7, the as grown PL spectrum is compared with irradiated MQWs spectrum. PL spectrum of irradiated sample depicts luminescence peaks for GaN and AlGaN at 3.4 and 3.78 eV respectively and it shows that the luminescence intensity has increased by one order of magnitude upon irradiation.
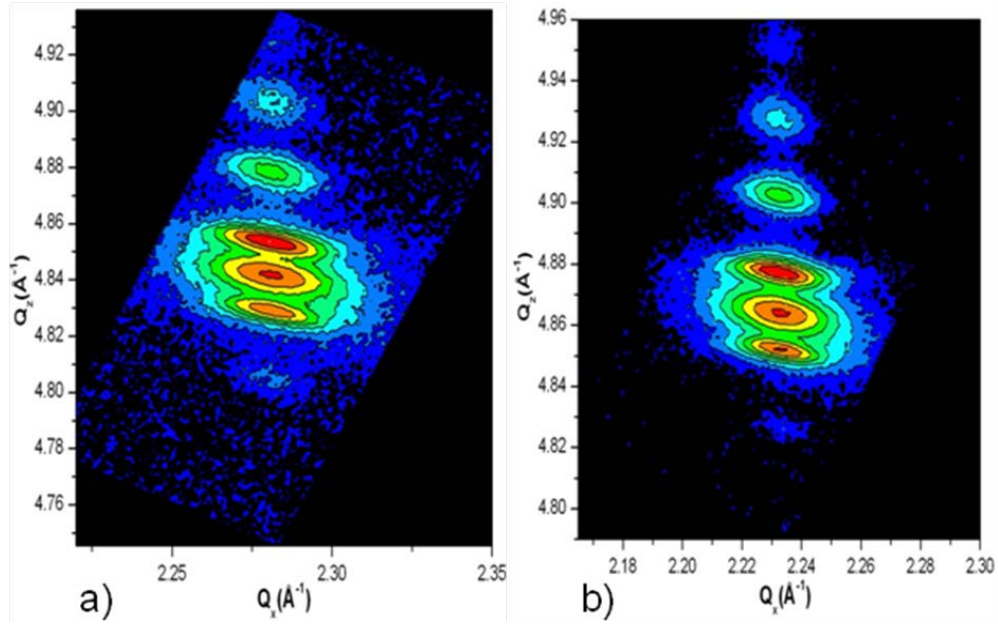
Fig.5.5: RSM taken along the asymmetrical (1 0 -1 4) GaN reflection a) as grown and, b) irradiated sample.
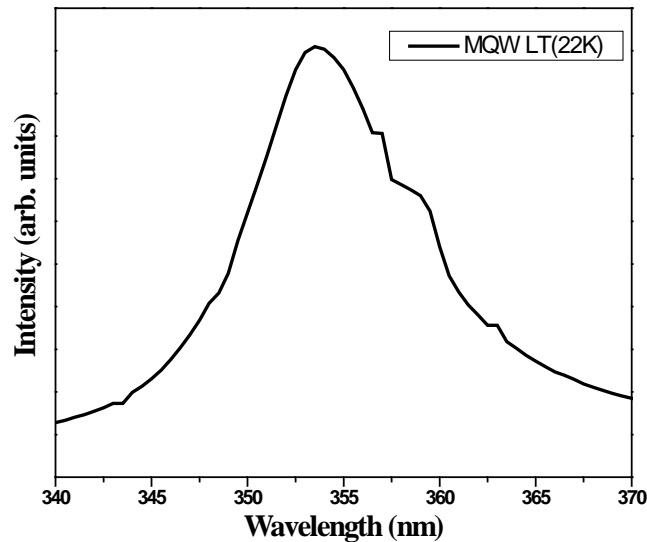
Fig. 5.6: Low Temperature - Photoluminescence spectra of AlGaN/GaN multi quantum wells.

As shown in Fig.5.8, irradiated sample shows intense yellow luminescence. The origin of the yellow luminescence band is still unknown. There are two models, which explain the recombination mechanism partially: First, Ogino et al. [21] proposed that the yellow emission is due to transition from a shallow donor to a deep acceptor level. Second, Glaser *et al.* [22] concluded recently, from optically detected magnetic resonance

experiments that the yellow transition involves a deep donor and, therefore, a shallow acceptor.
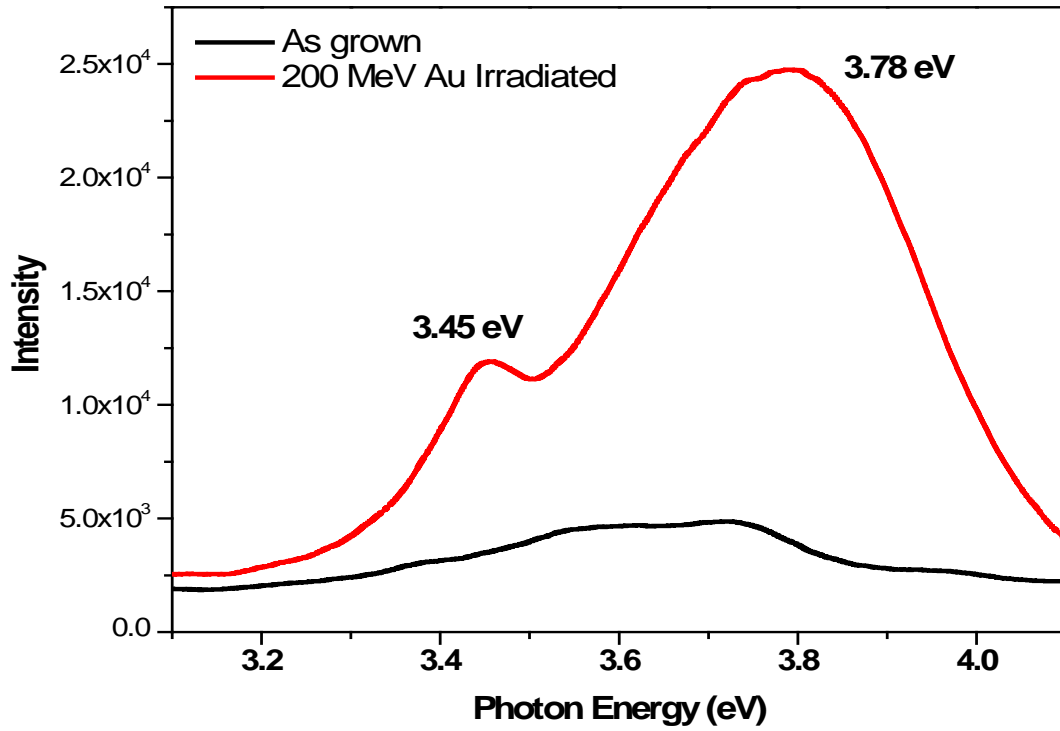
Fig. 5.7: Photoluminescence spectra of as grown and Au ions irradiated MQWs sample at room temperature.

Present study reveals from PL spectra that irradiated sample shows intense yellow luminescence peak at 2.21 eV which is due to recombination from ions induced distant donor acceptor pairs. Considering the Thermal Spike model, the susceptibility to damage formation is related to the efficiency of the energy transfer from the electronic system to the lattice which depends on electron-phonon coupling constant 'g'. Assuming that a higher fraction of S_e is transferred to the lattices lead to more pronounced damage formation and subsequent annihilation. This eventually isolates donor-acceptor atoms from its parent lattice site as shallow and deep levels between the conduction and valence band. Therefore, we can speculate the origin of intense yellow luminescence as a recombination of distant donor- acceptor pairs which were created due to ion bombardment. It may also be concluded that at higher S_e , low ion fluences have no detrimental effects on structural properties and optical properties.
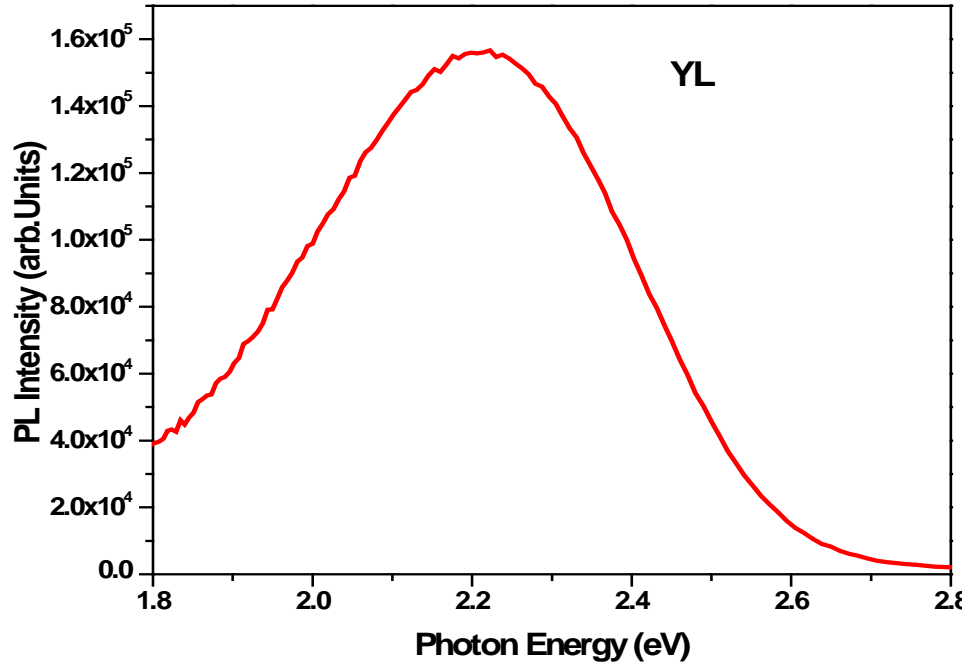
Fig.5.8: RT-Photoluminescence spectrum for irradiated MQWs shows yellow luminescence around 2.21 eV

5.5. 80 MeV Ni and 120 MeV Au ions at a fixed fluence of 1×10^{12} ions/cm^2

5.5.1. HAADF- STEM

Fig.5.9 shows a HAADF-STEM image of the as-grown AlGaN/GaN MQW structures with well resolved quantum wells and barriers. From the image, the thickness of the MQW period is estimated to be 25 nm with a well and barrier thickness of 17 nm and 8 nm respectively. These values are in good agreement with those extracted from the corresponding Philip's epitaxial simulation of experimental Omega-2theta scans obtained from HRXRD [23]. The intensity in HAADF-STEM imaging of perfect crystals is, to a first approximation, proportional to Zn (with n~1.7-2) [24, 25]. The substitutional change of Ga (Z=31) in GaN by Al (Z=13) leads to a lower average atomic number for the barrier, in comparison to the quantum well and, consequently, a reduced intensity is observed in the Z contrast images.
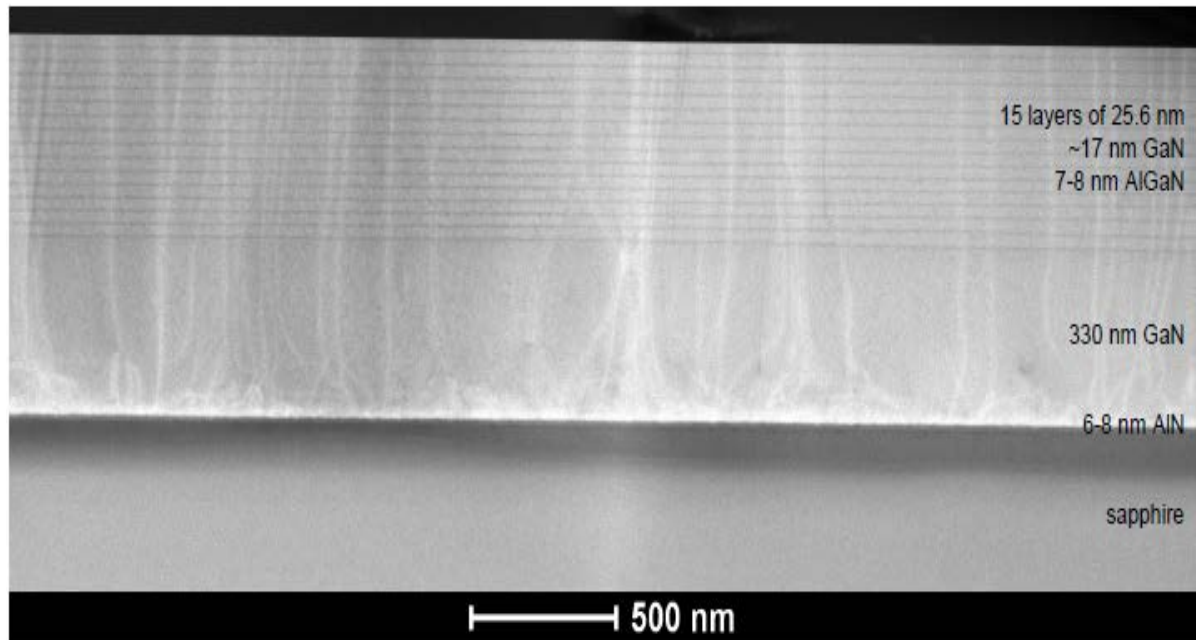
Fig.5.9: HAADF-STEM overview of the GaN/AlGaN MQWs structure: the 15 AlGaN/GaN layers of the MQW layers are clearly resolved. In addition, the strained sapphire/AlN/GaN interface is visible, which generates defects, which penetrate the multilayer structure.
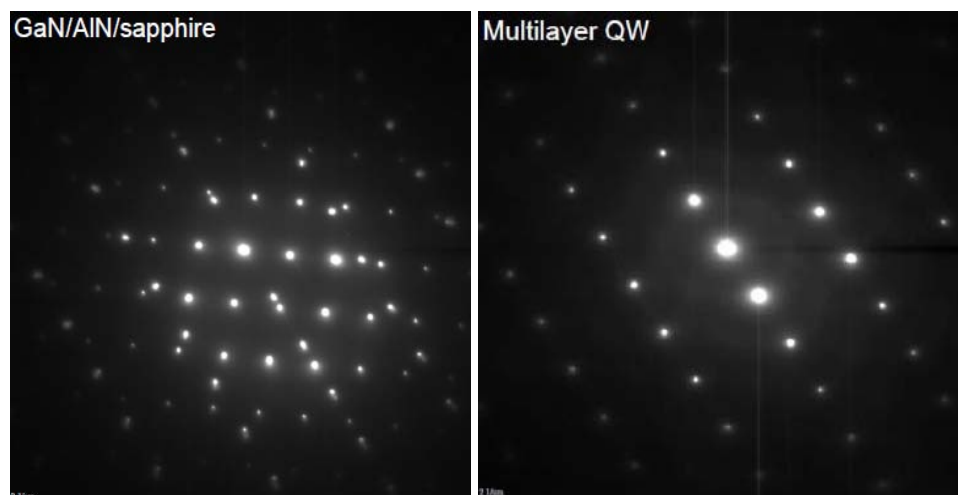
Fig.5.10: SEAD patterns taken across a) the sapphire/AlN/GaN and b) the MQWs

Threading dislocations appear as bright contours in the MQW matrix. These dislocations started at the interface of the sapphire-AlN buffer layer and at the AlN/GaN interface due to the large lattice and thermal mismatch. Nevertheless, selected area electron diffraction (Fig.5.10 a) of the interface area reveals a good epitaxial relationship between the AlN/GaN layer on the sapphire substrate.
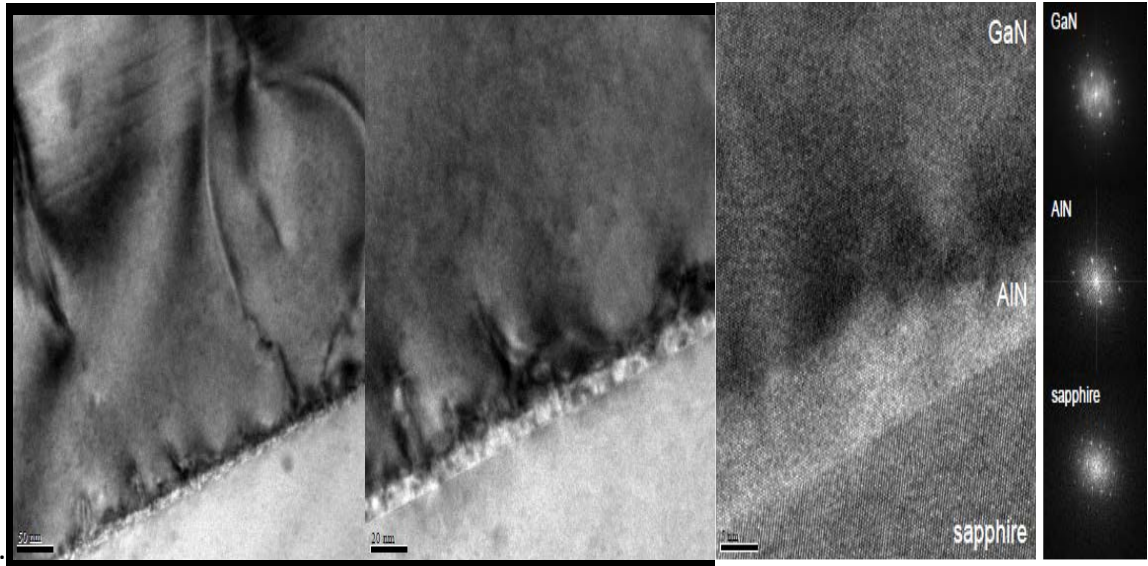
Fig.5.11: BF-TEM and HAADF-STEM images of the AlGaN/GaN MQWs film grown on sapphire template.
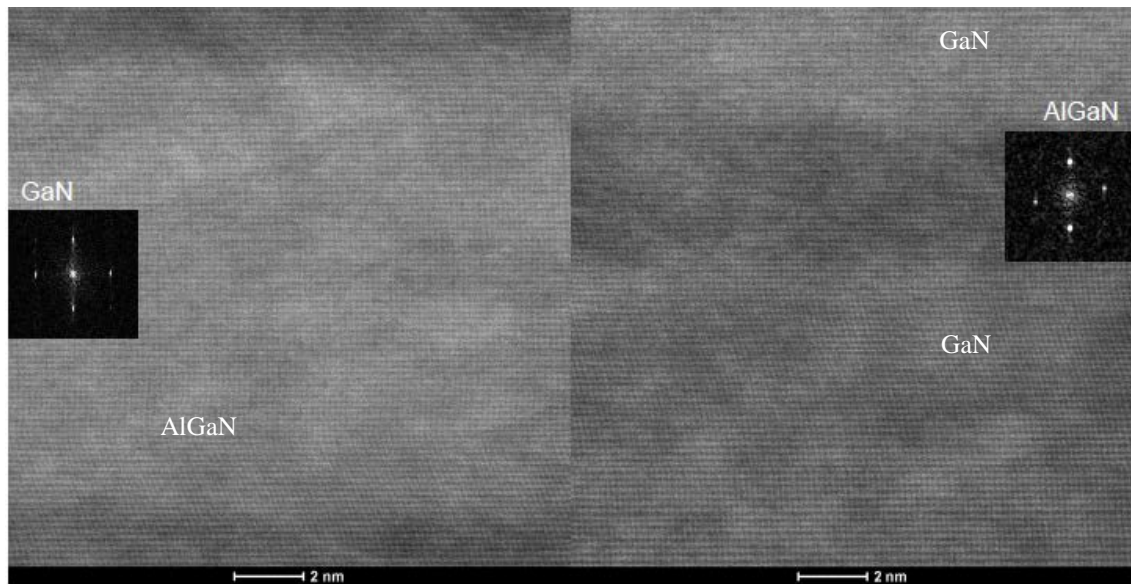
Fig.5.12: HRSTEM image of AlGaN barriers and GaN wells.

Some of the dislocations grew through the buffer layer into the epilayers, but the highest density of dislocations originates from the AlN/GaN interface and is observed within the first 50 nm from the AlN/GaN interface. The BF-TEM image is dominated by strain contrast contributions from the threading dislocations at the sapphire/AlN/GaN interface. The HAADF-STEM image reveals the roughness of the AlN/GaN interface. Further away from the interface, the defect density is significantly reduced resulting in a significant reduction of dislocations within AlGaN/GaN QW layers.

86
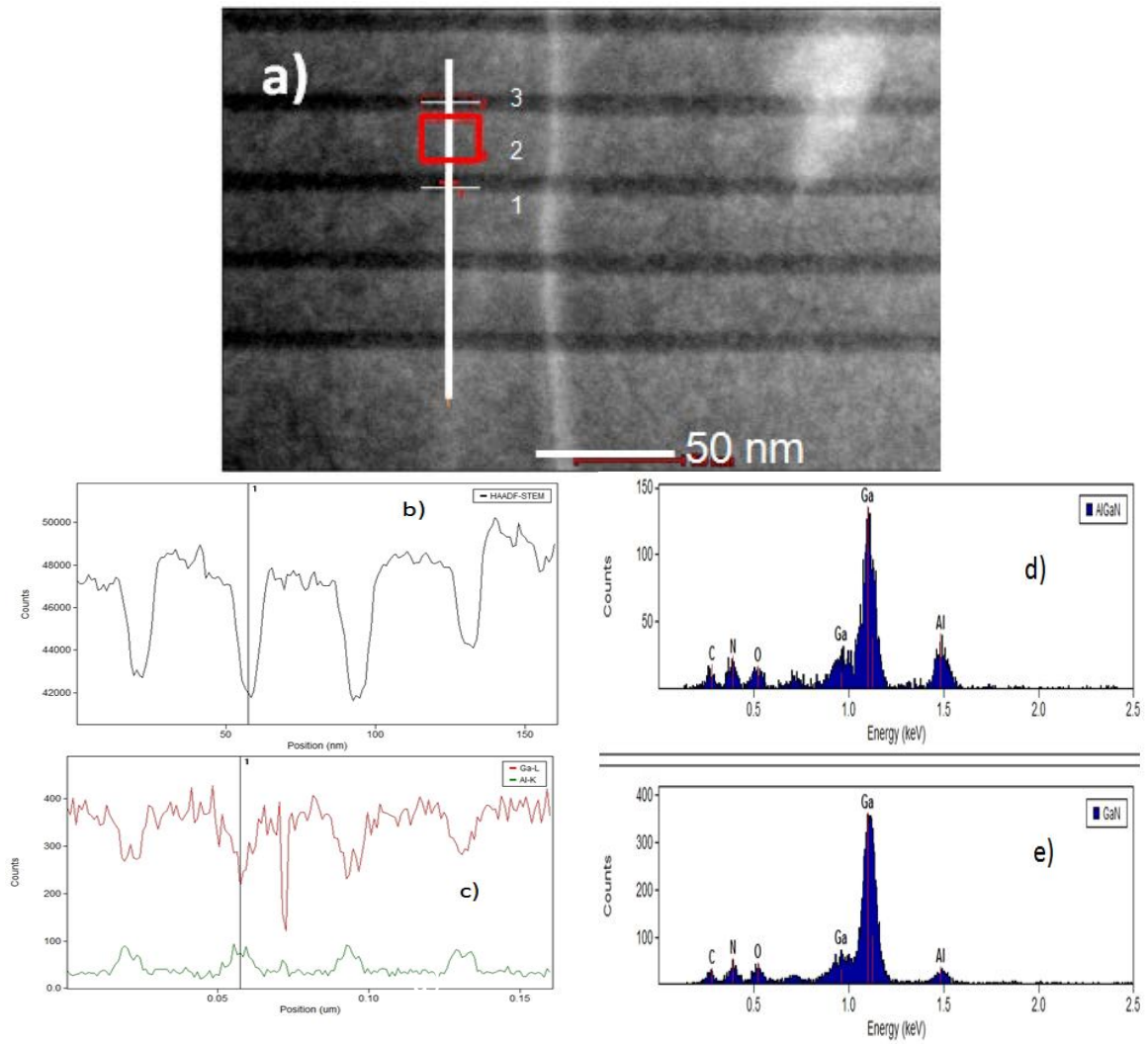
Fig.5.13: a) HAADF STEM overview image b) HAADF-STEM intensity profile recorded with the STEM-EDX line profile. c) Intensity profiles of Ga K_α and Al K_α measured by EDX along line shown in a), d) and e) Exemplary EDX spectra averaged over well and barrier.

A number of misfit dislocations from the AlN/GaN interface are seen to bend close to the interface and thread through the AlGaN layers. Our present results are consistent with those of Bai et al. and Egawa et al. [26, 27]. BF-TEM and HAADF-STEM images (Fig.5.11) of the sapphire/AlN/GaN interface show that the sapphire/AlN interface is smooth, whereas the AlN/GaN interface is quite rough.

Except for the threading dislocations from the substrate, the HAADF-STEM overview images (Fig.5.9) and the HRSTEM images of the MQWs in Fig.5.12 do not show any

87

formation of extensive defects in the GaN/AlGaN layers suggesting that the lattice mismatch in the MQWs is mainly compensated by strain fitting to the single crystal-like SAED pattern of the MQW area in Fig. 5.10.
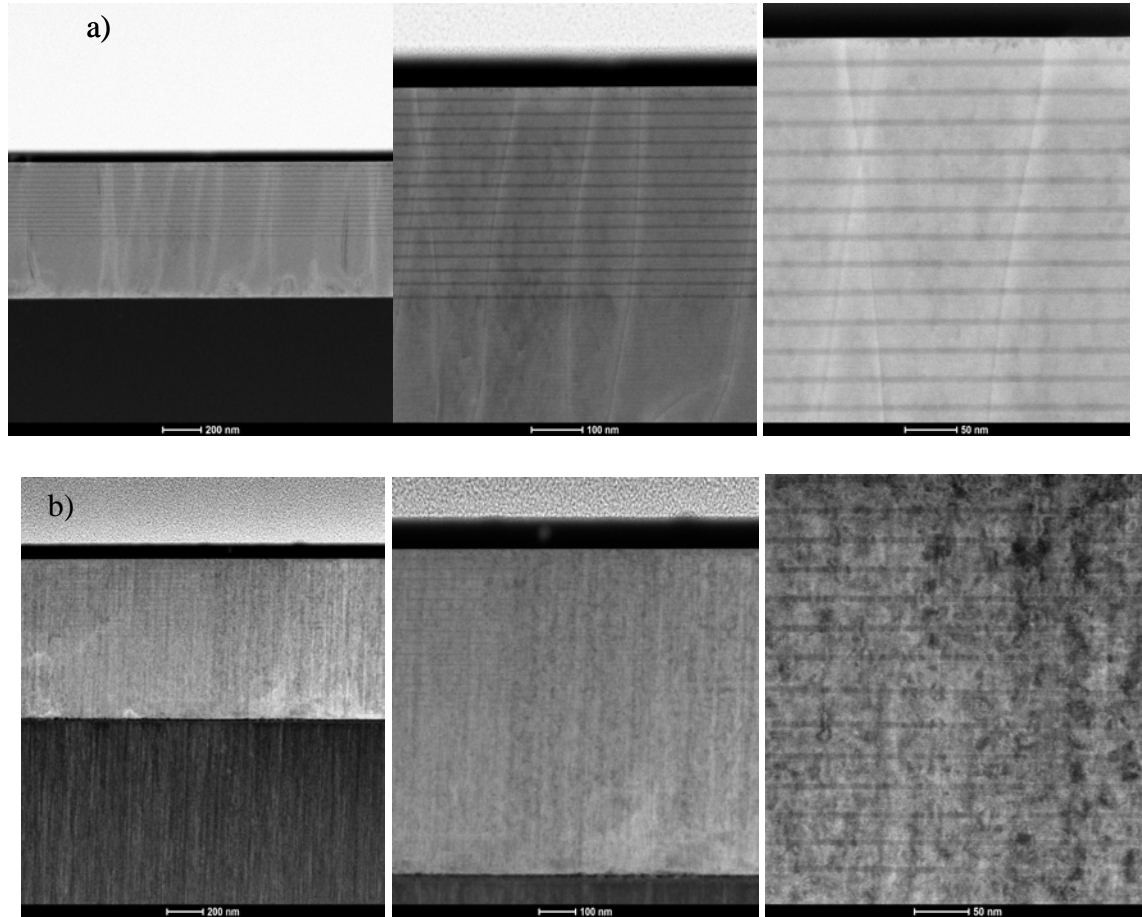
Fig. 5.14: HAADF-STEM images of the MQWs after irradiation a) 80MeV Ni, b) 120 MeV Au.

Fig.5.13 shows a HAADF STEM overview image and the corresponding HAADF-STEM signal with an EDX compositional Ga-Al line profile along the line shown in the STEM image. Exemplary EDX spectra averaged over a GaN well and an AlGaN barrier confirm the basic composition of the MQWs (in addition to some carbon contamination and some sapphire re-deposition from the substrate). After irradiation with 80 MeV Ni at a fluence of $1x10^{12}$ ions/cm^2, HAADF-STEM imaging of the MQWs (Fig.5.14) does not reveal any significantly different structure compared to the pristine sample. However, after 120 MeV Au ions irradiation, a drastic decrease in MQW quality is obvious in the HAADF-STEM images. In some areas, the multi layer structure is not recognizable anymore and the

HRSTEM image reveals a large number of defects in the MQW region.

5.5.2. Raman Spectroscopy

The $E_2(H)$ and A1(LO) phonon modes are generally used to monitor stress and free carrier concentrations in III- Nitrides. The $E_2(H)$ mode is observed in the pristine, the Ni and the Au irradiated samples and the sapphire mode (Eg) at 750 cm^{-1} is also observed for all samples.

Table.5.2. FWHM values of E_2 and A_1 modes, and perpendicular strain from pristine, 1473-Ni and 1473-Au samples.

Sample ID	E_2(high) (cm^{-1})	FWHM (cm^{-1})	A_1(LO) (cm^{-1})	FWHM (cm^{-1})	strain from (0002) HRXRD measurements
1473_AD	570	8.6	735	10	11×10^{-3}
1473_Ni	572, 568	6.5, 5.3	737	6.2	10.6×10^{-3}
1473_Au	570.4, 566 and 551	55,6.9 and 6.2	--	--	10.8×10^{-3}

A red shift in the $E_2(H)$ mode is evident for Ni and Au ion irradiated samples as shown in Fig.5.15 a). It is known that stress induces variations in the Raman shift [28] and a red shift can be easily understood according to the configurations of the phonon modes in which the atomic oscillations are in the c plane and therefore sensitive to the lattice strain [29]. We note a stronger configurational disorder as a result of the higher S_e values in the $Al_xGa_{(1-x)}N$ sample, which, in turn, result in an asymmetric Raman line shape of the E_2 phonons [30]. The spectra for the Ni and Au ion irradiated samples have been de-convoluted with multi Lorentzian peaks and the FWHM of the de-convoluted Raman modes as a function of Se are given in table 1. The $A_1(LO)$ phonon modes observed in pristine and Ni irradiated samples at 735 cm^{-1} and 737 cm^{-1} (Fig 5.15 b), are shifted to higher frequency than reported in the literature [31] and has a broader line shape.
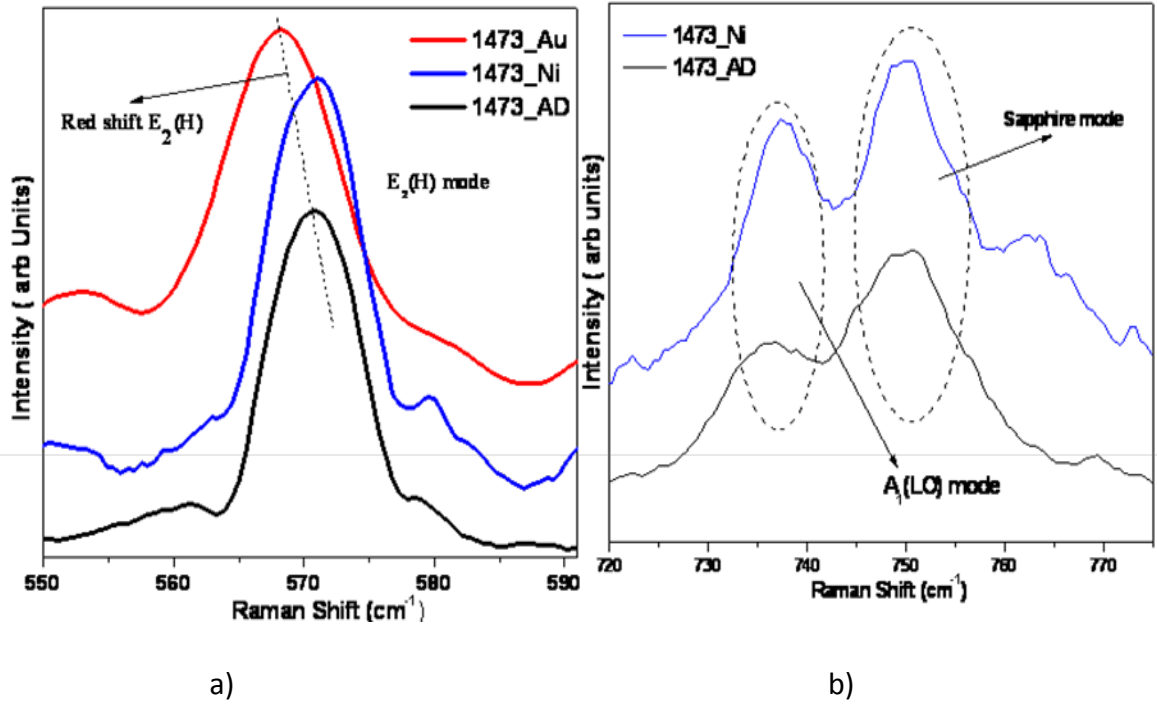
Fig.5.15: a) Raman spectra of 1473_AD, 1473_Ni and 1473_Au samples for the E_2(H) mode of GaN and b) Raman spectra corresponding to the A_1(LO) mode from 1473_AD and 1473_Ni samples.

An increase in intensity of the A_1(LO) mode can be seen for moderate S_e value irradiation. However, at higher S_e, there is no signature of the A_1(LO) mode visible. It is expected that the larger reduction of the free carrier concentration occurs at the position, where larger lattice damages are introduced by the high-energy irradiation.

5.5.3 High Resolution X- ray Diffraction (HRXRD)

Fig.5.16 shows ω-2θ scans of pristine and irradiated AlGaN/GaN MQWs samples. ω-2θ scans from pristine and moderate S_e irradiated AlGaN/GaN MQWs show well resolved satellite peaks next to the 0th order peak. Well resolved satellite peaks are due to a high periodicity of the multi layer structure which is consistent with the TEM results. An increase of S_e resulted in a shift in Bragg angle for the 0th order peak and also affected the satellite peaks.
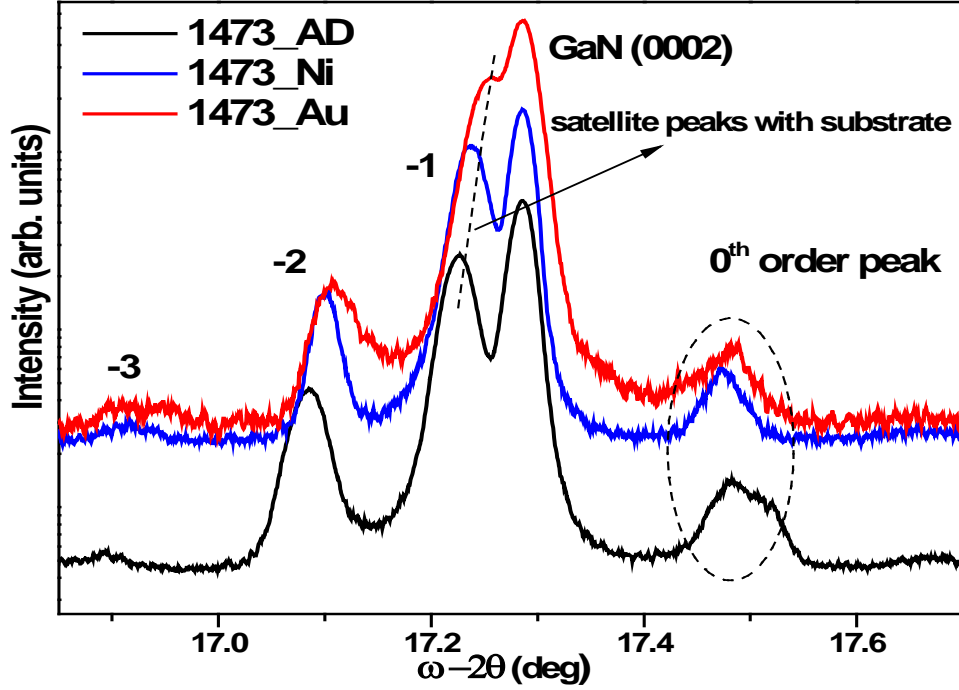
Fig.5.16: ω- 2θ scans from 1473_AD, 1473_Ni and 1473_Au samples.

Perpendicular strain has been estimated from GaN and 0th order peak which is found to be decreasing with Ni and Au ion irradiation as shown in Table.1. As S_e increases the intensity of the satellite peaks decreases due to degradation of interfaces. This implies that at higher S_e values, ions predominantly loose energy to lattices via electron phonon coupling, resulting in atomic diffusion at the interfaces of the multi layer structure.

5.6 Conclusions

MOCVD grown AlGaN/GaN MQWs have been irradiated with different heavy ions such as 200 MeV Au ions at a fixed fluence of $5x10^{11}$ ions/cm^2, 80 MeV Ni and 120 MeV Au ions at a fixed fluence of $1x10^{12}$ ions/cm^2. Several symmetric and asymmetric reflections were recorded to identify the 0th order peak. Essentially, these measurements have also been used to estimate out-of-plane and in-plane strains from pristine and irradiated samples. Irradiated AlGaN/GaN MQWs with 200 MeV Au ions at a fluence of $5x10^{11}$ ions/cm^2 have shown improved interfaces which is evident from improved intensity of satellite peaks. The measured strain values show that strain increases upon irradiation. Moreover, improved band to band transitions are also observed from enhanced intensity of PL emission. Increase in intensity of luminescence is attributed to ion beam induced dynamic annealing process. Therefore, we can conclude that the origin of intense yellow

luminescence is related to recombination of distant donor- acceptor pairs which are created due to ion bombardment.

HAAD-STEM has been used to understand the interfaces of MQWs and buffer layers. An improved interface quality and reduced defects along the c-axis have been observed in the MQW region due to the use of AlN and GaN buffer layers. A large number of misfit dislocations at the GaN/AlN interface are seen to bend through the interlayer and thread through the AlGaN/GaN layers. HAADF-STEM image from Ni ions irradiated MQWs does not reveal a significant difference in structure as compared to the pristine sample. However, after 120 MeV Au irradiation, a drastic decrease in MQW quality and significantly increase in defect density are observed from HAADF-STEM images. It is evident from the HRXRD results that moderate S_e irradiation has improved the quality of the interfaces compared to the pristine AlGaN/GaN MQW interfaces. HRXRD revealed that, after the initial improvement, the degradation of interfaces increases as Se value increases. At higher S_e there are two significant observations: a) a red shift and asymmetry in the E_2 (H) mode, which are attributed to ion beam induced intermixing b) a decrease in free carrier concentration where larger lattice damages are introduced. Finally, it is observed that ion beams for a given critical fluence and projectile energy do not show any detrimental effects in III- nitride compound semiconductors.

5.7 References

1. B Luo, J Kim, F Ren, J K Gillespie, R C Fitch, J Sewell, R Dettmer, G D Via, A Crespo, T J Jenkins, Appl. Phys. Lett. 82, 1428 (2003)

2. A Y Polyakov, N B Smirnov, A V Govorkov, A V Markov, S J Pearton, A M Dabiran, A M Wowchak, B Cui, A V Osinsky, P P Chow, N G Kolin, V M Boiko, and D I Merkurisov, Appl. Phys. Lett. 93, 152101 (2008)

3. T Takeuchi, H Takeuchi, S Sota, H Sakai, H Amano and I Akasaki, Jpn. J. Appl. Phys. 36, L177 (1997)

4. C Wetzel, T Takeuchi, S Yamaguchi, H Katoh, H Amano and I Akasaki, Appl. Phys. Lett. 73, 1994 (1998)

5. S Nakamura, Jpn. J. Appl. Phys. 30, L1705 (1991)

6. Wei Li, Appl. Phys. Lett. 69, 3390 (1996)

7. S Yoshida, S Misawa and S Gonda, Appl. Phys. Lett. 42, 427 (1983)

8. S ÇÖrekçi, M K Ozturk, B Akaoglu, M Cakmak and S Ozceliek, J. Appl. Phys. 101, 123502 (2007)

9. W H Weber and R Merlin, Editors, Raman Scattering in Materials Science, Springer, Berlin (2000)

10. B D White, M Bataiev, L J Brillson, B K Choi, D M Fleetwood, R D Schrimpf, S T Pantelides, R W Dettmer, W J Schaff, J G Champlain, and A K Mishra, IEEE Trans. Nucl. Sci. 49, 2695(2002)

11. W Wesch, AKamarou, and E Wendler, Nucl. Instr. and Meth. B 225, 111 (2004)

12. H Boudinov, S O Kucheyev, J S Williams, C Jagadish, G Li, Appl. Phys. Lett. 78, 943 (2001)

13. S O Kucheyev, J S Williams, J Zou, C Jagadish, J. Appl. Phys. 95, 3048 (2004)

14. S Dhamodaran, G Devaraju, A P Pathak, A Turos, D K Avasthi, R Kesavamoorthy, B M Arora, Nucl. Instr. and Meth. B 266, 1810 (2008) & 266, 3552 (2008)

15. S O Kucheyev, H Timmers, J Zou , J. Appl. Phys. 95, 5360 (2004)

16. T Kozawa, T Kachi, H Kano, Y Taga, M Hashimoto, N Koide, and K Manabe, J. Appl. Phys. 75, 1098 (1994)

17. M Yoon, I W Park, H Choi, S S Park, and E K Koh, Jpn. J. Appl. Phys. Part 1, 44, 828 (2005)

18. R X Wang, S J Xu, S Fung, C D Beling, K Wang, S Li, Z F Wei, T J Zhou, J D Zhang, Y Huang, and M Gong, Appl. Phys. Lett. 87, 031906 (2005)

19. R Zaus, J. Appl. Crst. 26, 801-811 (1993)

20. W Li , P Bergman , I Ivanov , Ni W-X, Amano H and I Akasa , Appl. Phys. Lett. 69, 3390 (1996)

21. T Ogino and M Aoki, Jpn. J. Appl. Phys. 19, 2395 (1980)

22. E R Glaser, T A Kennedy, K Doverspike, L B Rowland, D K Gaskill, J A Freitas, Jr M Asif Kahn, D T Olson, J N Kuznia, and D K Wickenden, Phys. Rev. B 51, 13326 (1995)

23. G Devaraju, N Sathish, A P Pathak, A Turos, M Bazzan, E Trave, P Mazzoldi, B M Arora, Nucl. Instr. and Meth. B 268, 3001 (2010)

24. M Takeguchi, M R McCartney, and D J Smith, Appl. Phys. Lett. 84, 2103(2004)

25. S J Pennycook, B Rafferty, and P D Nellist, Microsc. Microanal. 6, 343 (2000)

26. J Bai, T Wang, P Coming, P J Parbrook, J P R David, and A G Cullis, J. Appl. Phy. 99, 023513 (2006)

27. T Egawa, H Ohmura, H Ishikawa, and T Jimbo, Appl. Phys. Lett. 81, 291 (2002)

28. P Perlin, CJauberthie-Carillon, J P Itie, A S Miguel, I Grzegory and A Polian, Phys. Rev. B 45, 83 (1992)

29. J W Chen, Y F Chen, H Lu and W J Schaff, Appl. Phys. Lett. 87, 041907(2005)

30. L Bergman, M D Bremser, W G Perry, R F Davis, M Dutta, R J Nemanich, Appl. Phys. Lett. 71, 2157 (1997)

31. Anwar Hushur, Murli H. Manghnani and Jagdish Narayan, J. Appl. Phys. 106, 054317 (2009)

Structural changes induced by swift heavy ion beams in AlInN/GaN heterostructures

6.1 Introduction

The family of III- nitrides has numerous applications in optoelectronic, high power and high frequency devices. In particular, AlGaN and InGaN hetero structures (HS) have been investigated extensively compared to AlInN. On the other hand, high quality nearly lattice-matched AlInN/GaN heterostructures were reported by several research groups [1–7]. These structures have been used for realizing Bragg reflectors, microcavities and transistors [3, 6, 8, 9]. Furthermore, AlInN alloys cover extremely wide spectral range from deep UV to infrared. However, the growth of AlInN over the full compositional range is difficult due to large disparities in cation size (0.53 A˚ for Al^{3+} versus 0.76 A˚ for In^{3+}) [9] and thermal properties of the binary constituents [10–12]. Recently, it was demonstrated that biaxial strain (which depends on composition and thickness) is vital and influences miscibility gap [12]. Hence it is important to study the various factors that can influence the compositional gradients of these heterostructures.

Owing to their technological importance in satellite communications, there is a need to understand how the device performance degrades / improves under various kinds of irradiations including heavy ion bombardment. Thus, there is a great demand to understand the interface mixing and delimitation of HS under the influence of heavy ion irradiation. It is well known that when a fast moving ion passes through solid materials, it transfers large amounts of energy to the electronic subsystem through inelastic collisions by either electronic excitation or ionization of the target atoms [13]. At these velocities, ions in materials can create columnar defects [14], cylindrical tracks [15], amorphization [16] and recrystallizations [17]. Most of the high-energy irradiation results were understood by exploiting the concepts of planar defects, delamination, and tracks propagation [18–19].

In the recent past, it has been observed [20] that the electronic energy deposition beyond critical value can cause the movements of atoms leading to intermixing of multilayers. Swift Heavy Ion (SHI) induced mixing of various metal-semiconductor and semiconductor-semiconductor interfaces has been studied by several groups [20-26]. The

amount of mixing is found to be dependent on the amount of energy that is transferred to target electrons. It is observed that the intermixing is a result of diffusivity of atomic species during the transient molten phase in picoseconds range. However, similar effects in III-Nitrides have not been studied in any detail yet. Here, we study SHI induced mixing of both nearly lattice matched and tensile strained $Al_{(1-x)}In_xN$/GaN HS. Compositional profiles of as deposited and irradiated samples have been studied using Rutherford Backscattering Spectrometry (RBS) and High Resolution X-ray Diffraction (HRXRD) techniques. Subsequently, the surface morphology was studied by Atomic Force Microscopy (AFM). It is found that ion irradiation can obviously influence the surface morphology. (0002) symmetric ω-2θ scans are recorded and results are compared for pristine and irradiated samples. Consequently, strain from pristine and irradiated samples has been estimated and compared. Composition obtained from HRXRD for pristine sample has been compared with those obtained with RBS results. Inter diffusion of *Ga* and *In* elements across the $Al_{(1-x)}In_xN$/GaN interface and the consequent formation of a new mixed quaternary alloy ($Al_xGa_yIn_{1-x-y}N$) layer have been observed. The influence of electronic energy loss of SHI on intermixing effects has also been studied.

6.2 Experimental details

Tensile strained $Al_{(1-x)}In_xN$/GaN HS were grown on (0001) sapphire substrate by Metal organic chemical vapour deposition (MOCVD) technique. Then such samples were irradiated with 80 MeV Ni and 100 MeV Ag ions at different fluence (1×10^{12} and 3×10^{12} /cm^2). The corresponding average S_e and projected range of ions in AlInN for Ni ions are 10 keV/nm and 11 μm, and for Ag ions are 17 keV/nm and 10 μm, respectively.

Nearly lattice matched $Al_{(1-x)}In_xN$/GaN HS were grown on (0001) sapphire substrate by Metal organic chemical vapour deposition (MOCVD) technique. Pristine, 70 MeV Ni and 100 MeV Ag ions irradiated samples were named as T2A, T2B and T2C respectively. The purpose of this experiment is to study the influence of electronic energy loss of SHI on $Al_{(1-x)}In_xN$/GaN HS at a fixed fluence. Electronic energy loss (S_e) and nuclear energy loss (S_n) of 70 MeV Ni ions and 100 MeV Ag ions in HS were calculated using stopping and range of ions in matter code (SRIM 2003). Corresponding S_e and S_n for 70 MeV Ni and 100 MeV Ag are estimated to be 10 keV/nm , 0.02 keV/nm and 16 keV/nm, 0.08 keV/nm respectively. The projected range of these ions is found to be much larger than

the thickness of the film. Thus, ions predominantly deposit energy to target electrons uniformly throughout the film. Rutherford Backscattering Spectrometry (RBS) studies have been performed with a collimated beam of 2 MeV He$^+$ ions using a 2.5 MV model AN-2500 Van-de-Graaff accelerator (High Voltage Engineering) at National University of Singapore (NUS), Singapore. The backscattered He$^+$ ions have been detected at an angle of 170° using a silicon surface barrier detector with an energy resolution of 15 keV. We have used SIMNRA simulation code for fitting the measured RBS spectra. The structural properties of pristine and irradiated AlInN/GaN HS have also been characterized by High Resolution X-ray diffraction (HRXRD). These measurements around (0002) GaN reflection are carried out by a Bruker D8 DISCOVER, X- ray diffractometer with a Cu Kα source and four-bounce Ge (220) monochromator.

6.3 Tensile strained AlInN/GaN heterostructures

6.3.1 High resolution X-ray diffraction, RBS and AFM results

As shown in Fig.6.1, (0002) symmetric ω-2θ scan of pristine sample is carried out in triple axis geometry. Simulation of the HRXRD (Fig.6.1) has been carried out using the dynamical theory based Philips Epitaxy software [27]. Composition of the layer has been optimized by a trial and error method starting from some nominal values until a satisfactory fit is observed. The simulated scan matches reasonably well with the experimental one for nominal Indium composition of the layer as 12 %. Measured and simulated RBS spectra corresponding to $Al_{1-x}In_xN$/GaN HS experiments are shown in Fig.6.2. The elemental concentration has been determined by means of the SIMNRA simulation [28] and indium concentration is found to be 10 %. The arrows labeled In, Ga and Al indicate the energy of the backscattering He$^+$ ion from *In* and *Al* atoms at the surface and *Ga* atoms from GaN layer. The *In* signal is completely separated from the *Ga* signal and similarly, Al signal is clearly distinguishable from *Ga* in the spectrum. The window (between 560 -600 channels) shows gradient of *In* and *Ga* which is a result of diffusion of *In* and *Ga* from AlInN and GaN layers due to difference of ambient temperature during growth of AlInN and GaN layers.

As deposited, Ni and Ag ions irradiated ω-2θ rocking curves exhibited significant changes in AlInN (0002) peak positions. Effect of electronic energy loss (S$_e$) and fluence on Bragg angle can be seen in Fig.6.3. It is evident that Bragg angle for AlInN layer

increases with increase of fluence due to enhancement in strain values. This is attributed to point defects created by heavy ions affect lattice expansions or compressions (reduction) which in turn affected the strain. Interestingly at lower fluence, Ni and Ag ions irradiation has resulted in same strain values. However, higher S_e has resulted in further increase of strain as shown in Table.6. 1.
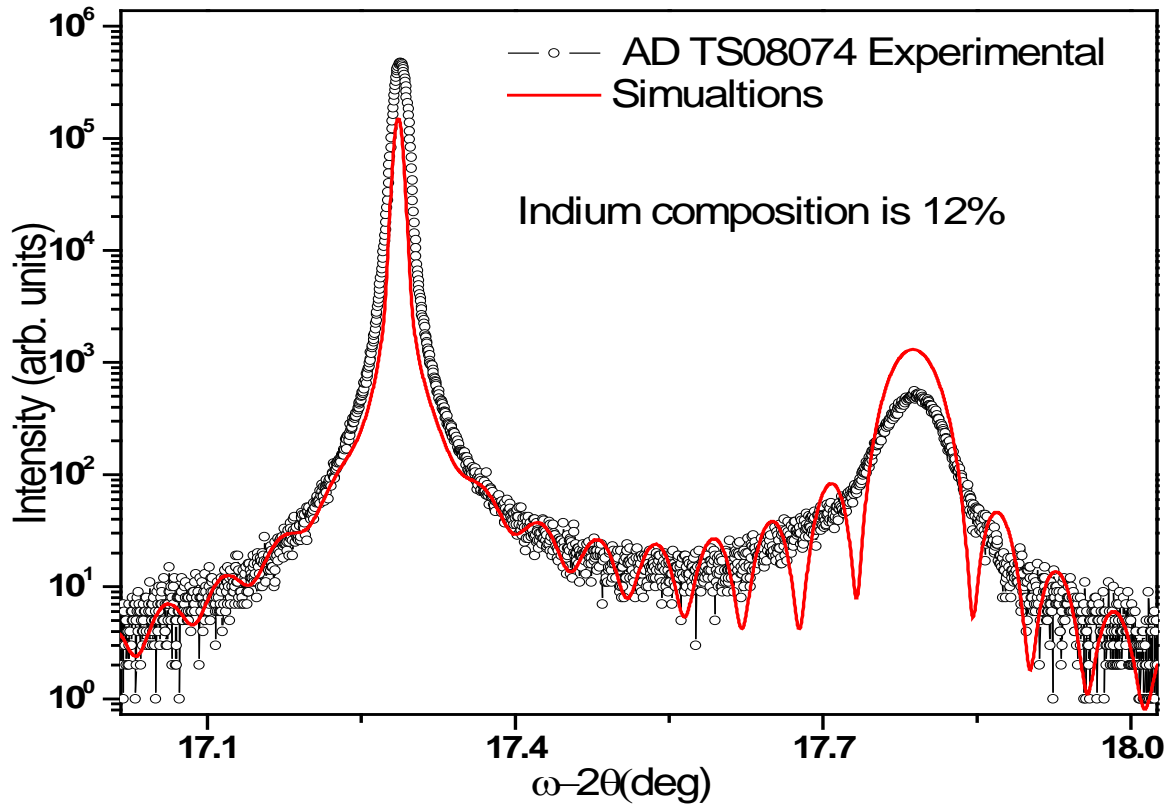
Fig.6.1: (0002) symmetric ω-2θ rocking curve of pristine AlInN/GaN HS fitted with Philip's epitaxy simulation

Fig.6.4 shows typical AFM images with a 2 x2 μm² scan area taken from the pristine and irradiated tensile strained AlInN/GaN HS. It is known that grain size depends on growth conditions like gas flow rate, growth temperature etc. In the present study AFM images clearly show surface morphology with uniform grain sizes for the pristine sample. At higher fluence, a significant change in surface morphology can be seen. The images for irradiated samples show that as Se value increases, the grain size slightly decreases. The surface roughness in terms of root mean square (rms) was measured to be approximately 5 nm for pristine sample. Significantly, Ag ions at moderate fluence have reduced the

surface roughness from 5 to 3.6 nm, while the reduction in rms roughness is insignificant (4.2 nm) for Ni ions irradiated samples.
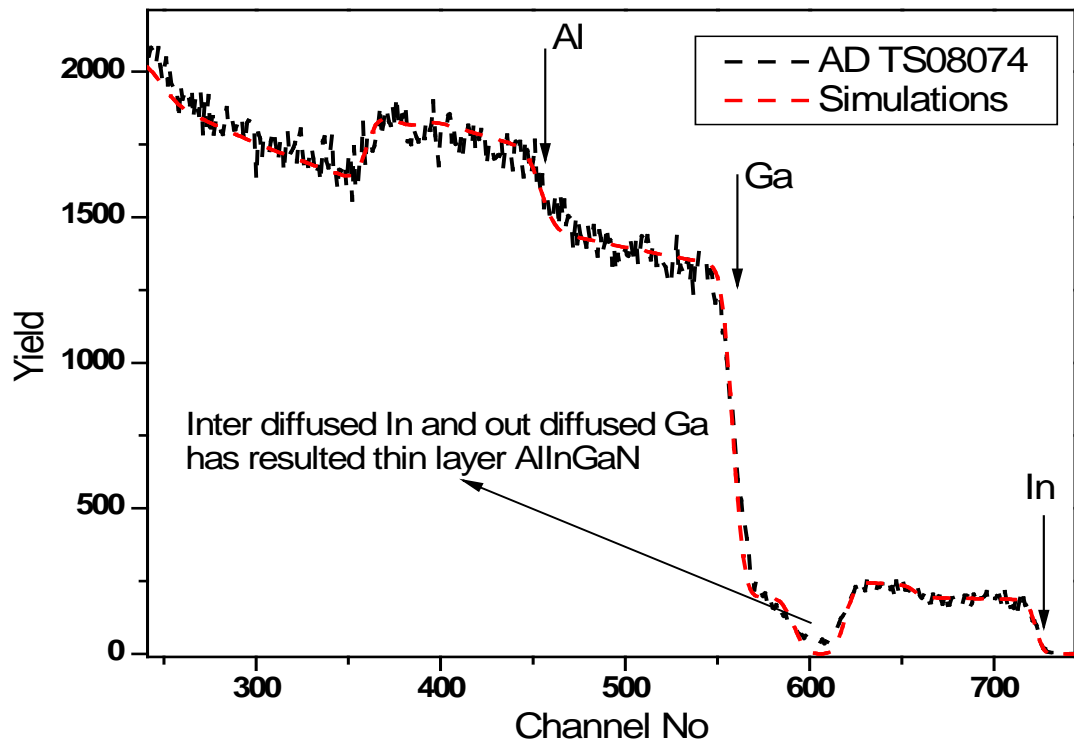
Fig.6.2: RBS spectra of as grown AlInN/GaN HS sample collected in backscattering geometry with detector at 165° has been fitted with SIMRA simulation code.
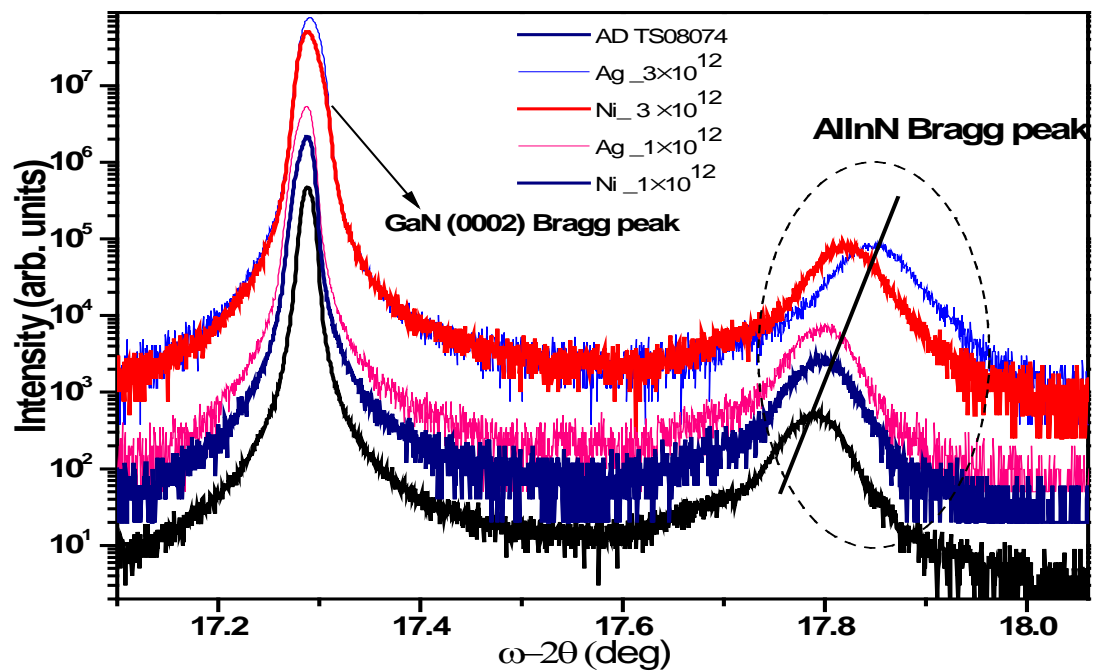
Fig.6.3: (0002) symmetric ω-2θ rocking curves of as grown and irradiated AlInN/GaN HS

a)   b)   c)

d)   e)
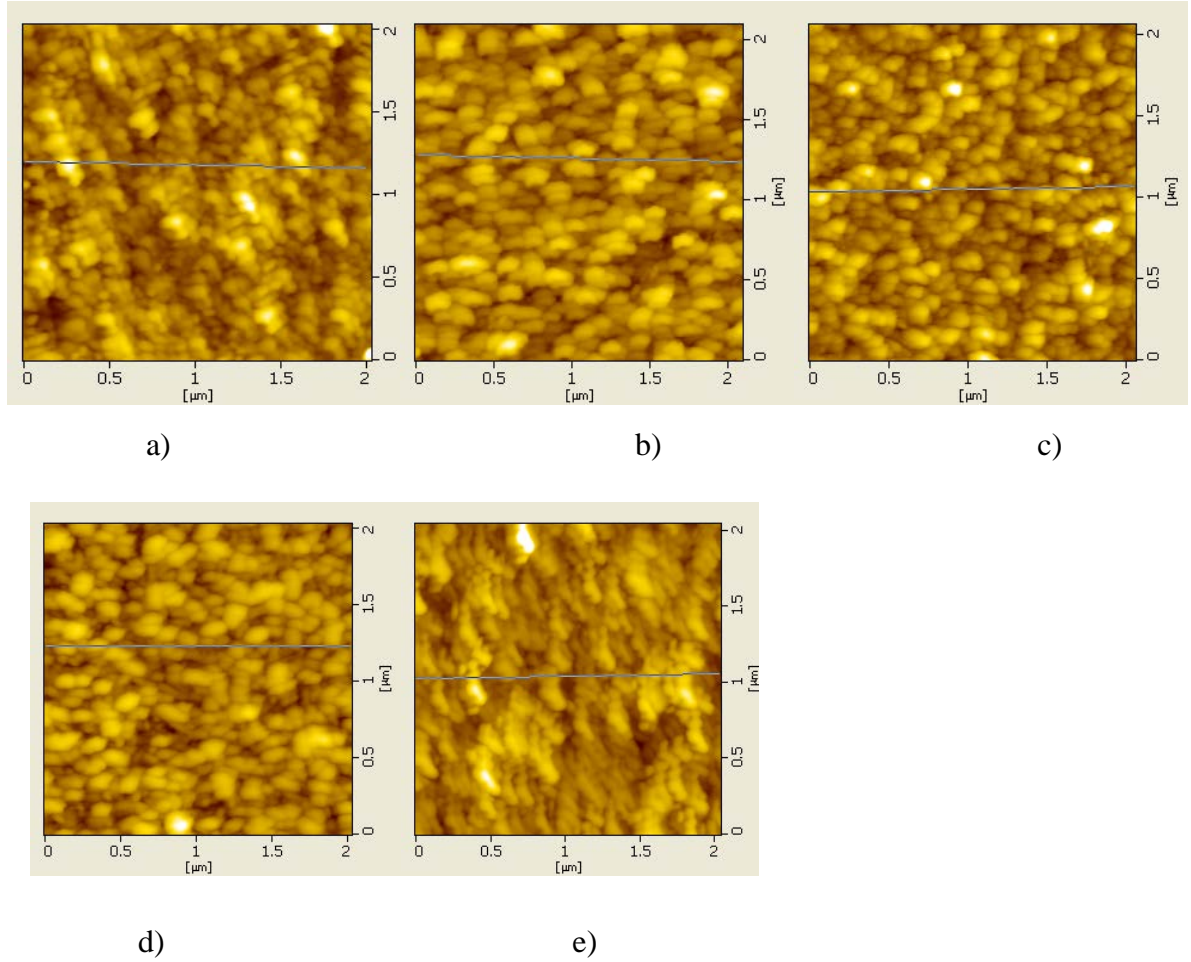
Fig.6.4: AFM images of a) pristine, irradiated b) 80 MeV Ni at 1×10^{12}, c) 100 MeV Ag at 1×10^{12}, b) 80 MeV Ni at 3×10^{12} d) 100 MeV Ag at 3×10^{12} with the scan area of 2×2 μm^2.

Table.6.1 Strain and RMS roughness of pristine and irradiated $Al_{(1-x)}In_xN$/GaN HS

Sample Details	Angular separation between GaN and AlInN Bragg peaks	RMS roughness from AFM
AD TS08074	0.49°	5 nm
80 MeV Ni ions @ 1×10^{12}	0.51°	5 nm
80 MeV Ni @ ions 3×10^{12}	0.53°	4.2 nm
100 MeV Ag ions @1×10^{12}	0.51°	4.2 nm
100 MeV Ag ions @ 3×10^{12}	0.56°	3.6 nm

6.4 Nearly lattice matched AlInN/GaN hetero structures by swift heavy ion irradiation:

RBS measurements are performed on pristine and irradiated samples (T2A, T2B and T2C) for determining Ga and In compositional profiles. The presence of *In, Ga* and *Al* can be observed in the RBS spectrum of pristine sample (T2A) shown in Fig.6. 5. Simulations are carried out using SIMNRA code by varying layer parameters starting with nominal values until a satisfactory fit is obtained. These measurements suggest that the presence of *Ga* in AlInN layer may be due to possible diffusion of *Ga* and *In* across the interface during the growth process. The average *In* composition is estimated to be around 21% in this layer as against the nominal value of 18%. Similar compositional gradients have been reported earlier for AlInN films [23, 24].

Generally, AlInN films close to lattice-matched conditions show pseudomorphic growth [24]. In the present study, the observed compositional gradient may lead to slight lattice mismatch between AlInN layer and GaN substrate. This is further confirmed by high resolution x-ray diffraction measurements. Symmetric rocking curve measurements were performed along the (0002) axis of GaN for determining the average *In* composition and lattice strain. Fig.6.6 shows the measured and simulated ω-2θ scans of the pristine sample (T2A). HRXRD simulation is carried out using the dynamical theory based Philips epitaxy software. The composition and thickness of the layer is optimized by a trial and error method, starting from nominal values until a satisfactory fit is observed. The simulated scan matches reasonably well with experimental data. The average *In* composition and the lattice parameter (c) obtained from these fits are given in Table.6.2. These values can be used for evaluating the out of plane strain in AlInN layer.

Table.6.2 Average indium composition of T2A, T2B and T2C samples obtained from HRXRD and RBS measurements.

Sample ID	Measured Lattice parameters (by HRXRD) C (Å)	Average Indium composition	
		HRXRD	RBS
T2A (Pristine)	5.150	0.21	0.21
T2B (Ni)	5.140 , 5.212 (bi layer)	0.20, 0.29	gradient
T2C (Ag)	5.146 , 5.205 (bi layer)	0.21,0.28	gradient
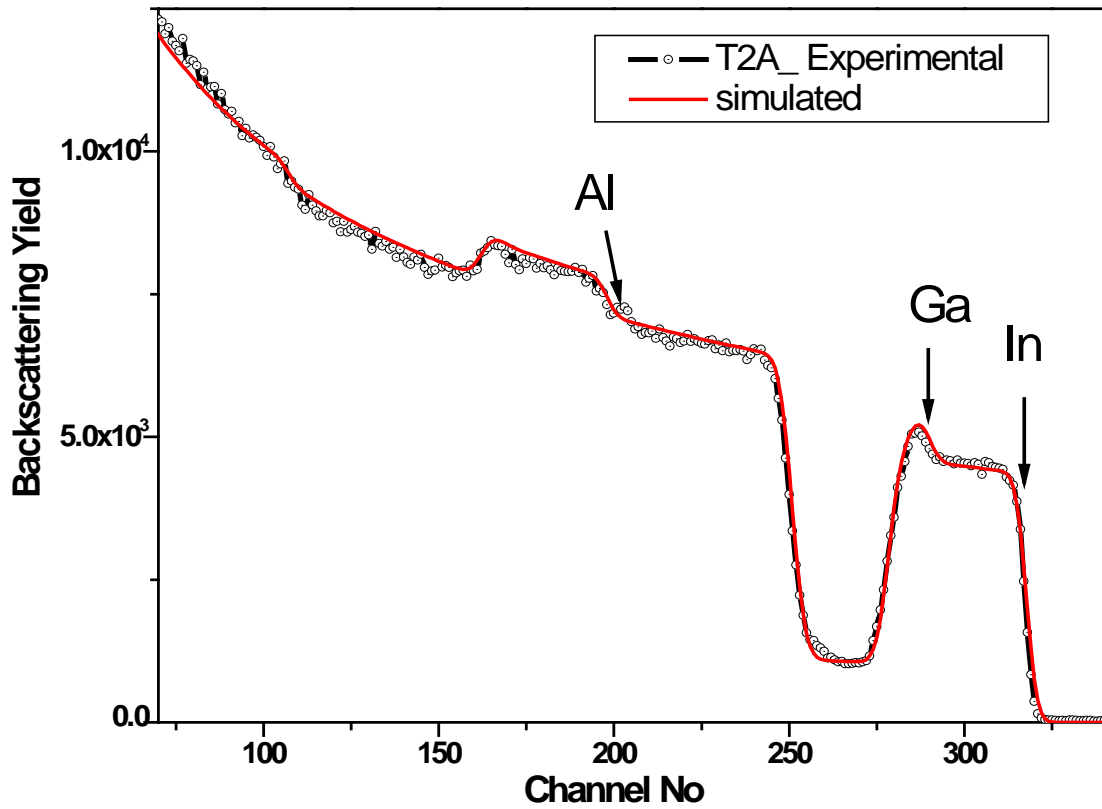
Fig.6.5: Measured and simulated RBS spectra of T2A sample showing Ga diffusion into Indium energy window

The measured RBS and HRXRD spectra of pristine and irradiated samples (T2A, T2B and T2C) are shown in Figures 6.7 and 6.8. These spectra confirm the SHI induced diffusion of *In* and *Ga* elements across AlInN/GaN interface. The enhanced diffusion of *In* and *Ga* due to 100 MeV Ag ion irradiation in T2C sample demonstrates the influence of S_e on SHI-mixing effects. The *Ga*-edge from GaN substrate in RBS spectra is found to be at lower energies in irradiated samples, particularly in T2C, as compared to pristine sample. This further confirms the formation of a thin intermixed layer between AlInN layer and GaN substrate. In fact, SIMNRA simulation of T2C sample suggested the formation of an inter-diffused layer (InGaAlN) with concentration gradients between InAlN and GaN layers. The influence of SHI induced mixing on the lattice strain in AlInN layer is studied using HRXRD measurements. Measured values of In composition and corresponding lattice constants are given in Table.6.2. Fig.6.8 clearly shows a significant shift in the Bragg angle of layer peak and a corresponding change in strain due to SHI irradiation as a function of Se. It is important to note that the ion irradiation can be

used to alter the strain by varying Se. In fact, tensile strain is induced (T2C) in an initially nearly lattice matched / compressive strained layer (T2A).
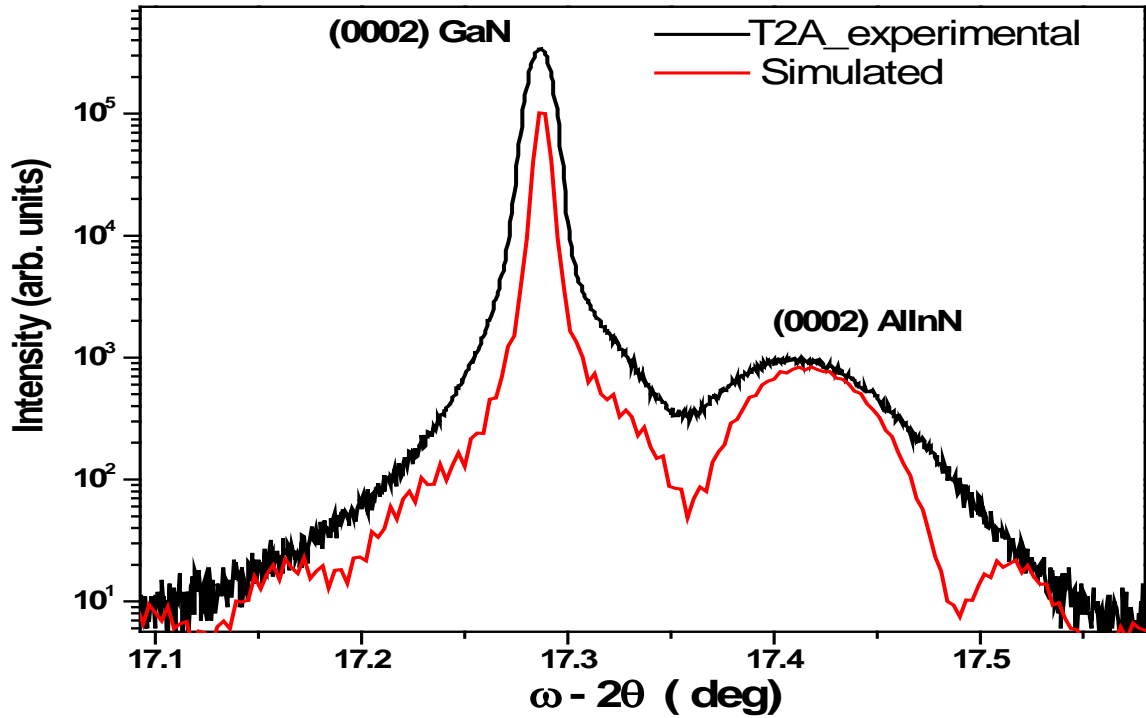
Fig.6.6: (0002) $\omega - 2\theta$ X-ray diffraction for T2A sample along with theoretical simulated profile.

It is known that Ion beams at moderate fluence can create latent tracks in various metal/semiconductor and semiconductor/semiconductor bi layer systems [20]. Such SHI induced intermixing has been observed by different research groups in different systems like Fe/Si , C/Si , C_{60}/Si, Co/Si , V/Si , Zr/Si, Cu/Ge , Ni/Si and Fe/Ni multi layers. In all the above studies, SHI induced mixing at the interfaces has been identified as atomic diffusion in molten phase created by transient temperature spike [25-26]. In the present study, It is noted from Fig .6.7 and Fig.6.8 that T2C sample shows more intermixing than T2B sample, which is due to a significant difference in S_e deposition rates for their corresponding ion propagation in $Al_{(1-x)}In_xN$/GaN HS. The enhanced diffusion of In and Ga across the AlInN/GaN interface at higher S_e (i.e in T2C) can be understood as a consequence of high quenching rates along the path of ions.
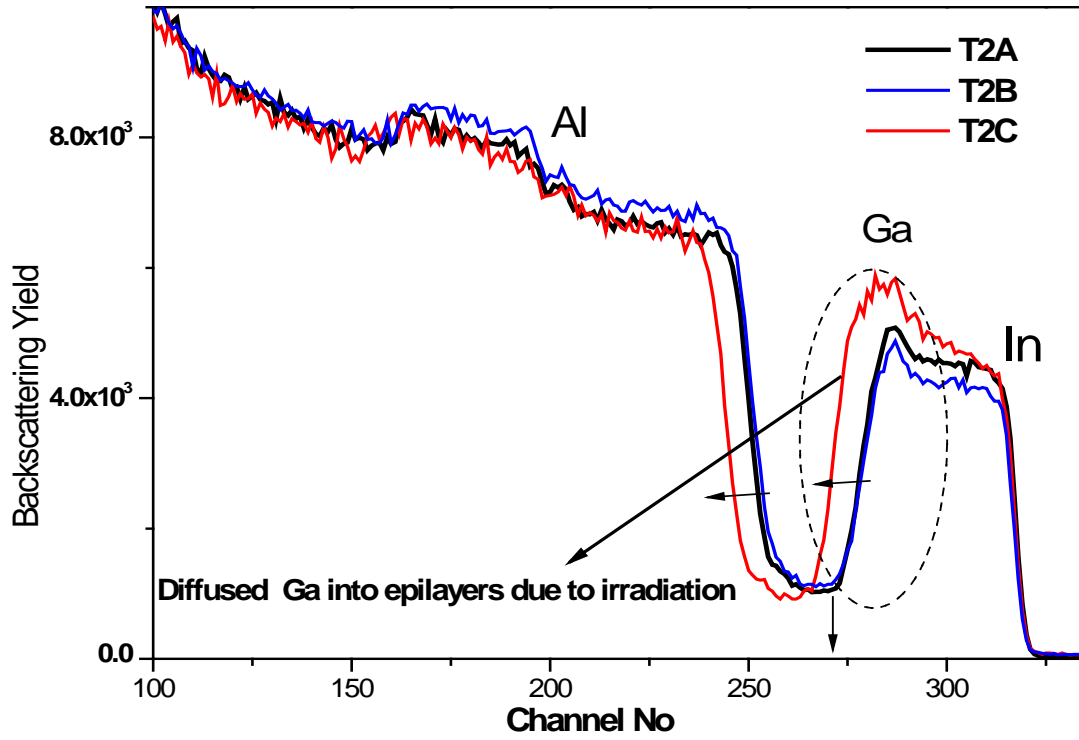
Fig.6.7: RBS spectra of T2A, T2B and T2C samples, SHI induced diffusion of Ga from GaN into AlInN epilayer are evident.
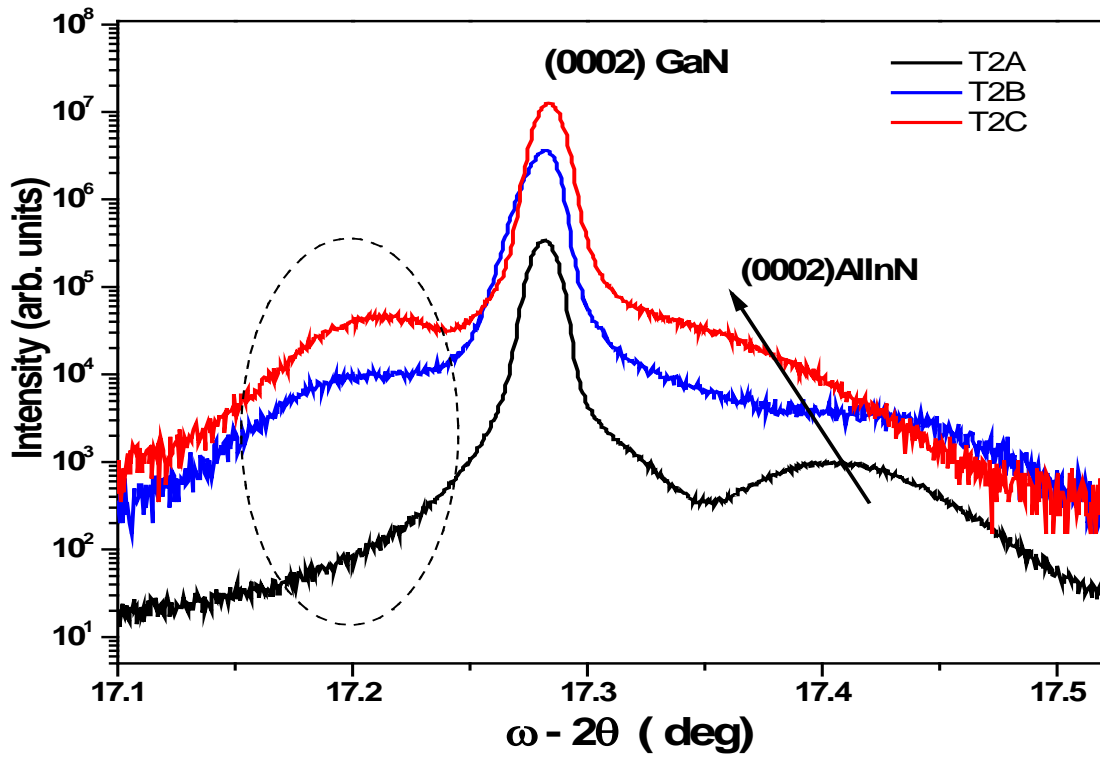
Fig.6.8: The (0002) HRXRD rocking curves of T2A, T2B and T2C samples. SHI induced modification of strain in epilayer is evident in spectra.

6.5 Conclusions

MOCVD grown Al$_{(1-x)}$In$_x$N/GaN HS were irradiated with Ni and Ag ions at varied fluence. HRXRD, RBS and AFM characterization techniques have been used for understanding the structural and surface morphology of pristine and irradiated samples. Philip's epitaxy simulation has been used for Indium composition of HS and is found to be 12 %. Random and simulated spectra of Al$_{1-x}$In$_x$N/GaN HS from RBS experiments are compared. It is evident from the RBS spectra that In and Al signals are completely separated from that of Ga signal. Increase in strain with increase of Se value has been noticed from HRXRD measurements. This means that there is an increase in Bragg angle of AlInN layer which could be attributed to ion beam induced lattice reduction. Eventually, this work demonstrates that ion irradiation can create point defects which affect lattice expansion or compressions (reduction). Hence, irradiation changed interplanar spacing which consequently affected the strain. AFM images clearly show change of surface morphology with irradiation leading to reduction in granular sizes. Significantly, Ag ions at moderate ion fluence have resulted in lower surface roughness from 5 to 3.6 nm, while the reduction in rms roughness is insignificant (4.2 nm) for Ni ions irradiated samples.

SHI induced mixing effects in nearly lattice matched Al$_{(1-x)}$In$_x$N/GaN HS have been studied as a function of S$_e$. RBS technique has been used for determining composition profiles as a function of depth on pristine and irradiated samples. Compositional gradients have been observed in measured RBS spectrum of pristine sample. Average compositions obtained from RBS and HRXRD are in close agreement with nominal values. Moreover, observed diffusion gradient in RBS and HRXRD measurements is correlated with simulations. Change of strain status from nearly lattice matched / compressive strain to tensile strain has also been observed as function of S$_e$. Here it is shown that the SHI-mixing can be used to alter the strain in AlInN/GaN heterostructures. The present study indicates that it is possible to achieve complete mixing of AlInN and GaN layers to prepare a new mixed quaternary alloy (AlGaInN) which is otherwise quite difficult by usual growth methods.

6.6 References:

1. A Dadgar, F Schulze, J Blasing, A Diez, A Krost, M Neuburger, E Kohn, I Daumiller, and M Kunze, Appl. Phys. Lett. 85, 5400 (2004)

2. I M Watson, C Liu, E Gu, M D Dawson, P R Edwards, and R W Martin, Appl. Phys. Lett. 87, 151901 (2005)

3. K Bejtka, R W Martin, I M Watson, S Ndiaye, and M Leroux, Appl. Phys. Lett. 89, 191912 (2006)

4. K Jeganathan, M Shimizu, H Okumura, Y Yano, and N Akutsu, J. Cryst. Growth 304, 342 (2007)

5. S Schmult, T Siegrist, A M Sergent, M J Manfra, and R J Molnar, Appl. Phys. Lett. 90 , 021922 (2007)

6. O Katz, D Mistele, B Meyler, G Bahir, and J Salzmann, IEEE Trans. Electron Devices 52 ,146 (2005)

7. R D Shannon, C T Prewitt, Acta Crystallogr. B 25, 925 (1969)

8. J F Carlin, M Ilegems, Appl. Phys. Lett. 83 ,668 (2003)

9. J F Carlin, C Zellweger, J Dorsaz, S Nicolay, G Christmann, E Feltin, R Butte´, and N Grandjean, Phys. Status Solidi B 242, 2326 (2005)

10. T Matsuoka, Appl. Phys. Lett. 71, 105(1997)

11. M Ferhat, F Bechstedt, Phys. Rev. B 65, 075213 (2002)

12. C Hums, J Blasing, A Dadgar, A Diez, T Hempel, J Christen, A Krost, K Lorenz, and E Alves, Appl. Phys. Lett. 90, 022105 (2007)

13. J F Zeigler, J P Biersac, and U Littmark, Stopping and Range of Ions in Solids (Pergamon, New York, 1985), Vol. 1.

14. L Civale, A D Marwick, T K Worthington, M A Kirk, J R Thomson, L Krusin-Elbaum, Y Sun, J R Clem, and F Holtzberg, Phys. Rev. Lett. 67, 648 (1991)

15. R L Fleischer, P B Price, and R M Walker, J. Appl. Phys. 36, 4645(1965)

16. H Trinkus, Mat. Sc. Forum 248-249 (1997) 3

17. G S Virdi, B C Pathak, D K Avasthi, and D Kanjilal, Nucl. Instr. and Meth. B 187,189(2002)

18. H Boudinov, S O Kucheyev, J S Williams, C Jagadish, and G Li, Appl. Phys. Lett. 78, 943 (2001)

19. S O Kucheyev, J S Williams, J Zou, and C Jagadish, J. Appl. Phys. 95, 3048(2004)

20. C Dufour, Ph Bauer, G Marchal, J Grilhe, C Jaouen, J Pacaud, and J C Jousset, Europhys. Lett. 21 ,671(1993)

21. W Assmann, D K Avasthi, M Dobler, S Kruijer, H D Mieskes, and H Nolte, Nucl. Instr. and Meth. B 146 ,271(1998)

22. D Kanjilal, S Chopra, M M Narayanan, I S Iyer, V Jha, R Joshi, and S K Datta, Nucl. Instr. and Meth. A 328 ,97(1993)

23. K Lorenz, N Franco, E Alves, S Pereira, I M Watson, R W Martin and K P O'Donnell, J. Cryst. Growth 310 **,**4058(2008)

24. V Darakchieva, M Beckers, M-Y Xie, L Hultman, B Monemar, J-F Carlin, E Feltin, M Gonschorek, and N Grandjean, J. Appl. Phys. 103 **,**103513(2008)

25. S K Srivastava, D K Avasthi, W Assaman, Z Wang, H Kuacl, E Jacquet, H D Crastanjen, and M Toulemonde, Phys. Rev. B 71,0193405(2005)

26. K Diva, D Kabiraj, B R Chakraborty, S M Shivaprasad, and D K Avasthi, Nucl. Instr. and Meth. B 222 ,169(2004)

27. Halliwell et al. J. Cryst. Growth 68, 523 (1984)

28. M Mayer, Report IPP 9/113, Max–Planck-Institut für Plasmaphysik, Garching, Germany, 1997.

Chapter-VII

Conclusions and outlook

7.1 InGaAs/InP multi quantum wells

Tensile strained InGaAs/InP multi quantum wells were investigated before and after irradiation using different characterization techniques like HRXRD, AFM and PL for interfaces, surface morphology and band gap, respectively [1]. These structures have been realized with the novel growth technique like MOCVD. Importance of materials and their consequences on strain for band gap engineering under charged particle bombardment has been emphasized. Initially tensile strained MQWs have been further strained by the ion bombardment. As a function of ion fluence, an interface mixing induced disorder is observed from the vanishing of satellite peaks. Irradiation and subsequent annealing to anneal out the defects created by irradiation are discussed. Rapid Thermal Annealing has retrieved intermixing of quantum wells by diffusion of corresponding atomic species such as *In* and *Ga*. The decrease in *In* composition has reduced the epilayer lattice constant which has resulted in a shift of satellite peaks to the higher Bragg angles. As a result, strain into the epilayers further increases and causes a shift in the band gap. Irradiated and subsequently annealed samples show that there is a shift in zeorth order peak. An irradiated sample does not show any photoluminescence but upon annealing band to band transitions are observed. It is concluded that irradiation and subsequent annealing improves interface quality but changes strain which is correlated with the increase in band gap. Thus, a blue shift of 40 meV and 70 meV has been observed upon irradiation and followed by annealing process. AFM studies revealed no significant change in surface morphology. Hence, irradiated and subsequently annealed samples can be used for device applications.

7.2 MOCVD grown bulk GaN

Structural and optical characterizations have been carried out on MOCVD grown GaN samples before and after irradiation. HRXRD, micro-Raman and photoluminescence measurements have been used to understand the irradiation induced effects [2]. Increase in crystalline nature, and lattice swelling in growth direction upon irradiation has been

noticed from decrease of FWHM and shift in Bragg's peak to lower angles. It is evident that irradiation influences lattice parameters and consequently on phonon modes. W-H plots revealed insignificant increase in defect densities upon irradiation. Raman studies yield E_2 (H) modes that are sensitive to local strain which yields blue shift in E_2 mode for higher electronic energy loss. This has been attributed to compressive strain that is consistent with observed HRXRD results. The variation of the line shape of the A_1 (LO) mode of GaN with electronic energy loss is basically due to the coupling of A_1(LO) mode with an over damped plasmon. Therefore it is concluded that as electronic energy loss increases, the coupling of A_1 (LO) mode with an over damped plasmon increases. This could be due to transient rise in lattice temperature during heavy ion bombardment to very high values in a very short interval of time leading to certain collective rearrangements of atoms. The observed mode at 672 cm^{-1} is designated to local vibrational mode originating from the intrinsic defects such as V_N (nitrogen related defects), which is consistent with existing literature values.

Photoluminescence studies have been carried out on as deposited, then on Ni ions irradiated and subsequently annealed GaN samples [3]. Band to band (B-B)transitions are observed from pristine GaN sample but these transitions are missing for the irradiated samples. It shows BL band around 450 nm besides yellow luminescence from Ni ions irradiated GaN. Intensity of BL and YL upon irradiation and subsequent annealing has been correlated to *Ga* and *N* vacancies. From the present study, we can conclude that BL band is due to nitrogen related defects. Irradiated and subsequently annealed GaN shows existence of B-B transitions besides intra-gap defects' level transitions. PL measurements also show the effective reduction in YL intensity after irradiation and followed by annealing process. This can be considered to be arising due to substantial reduction in concentration of deep level defects like *Ga* vacancies which occurs due to annihilation of vacancies by the transfer of heavy ion energy to target electrons. As a consequence, intrinsic point defects like V_{Ga} or their complexes are annealed out along the ion trajectory. Therefore, it is assumed that the BL and YL are associated with *N* and *Ga* vacancies, respectively.

7.3 Tensile strained AlGaN/GaN multi quantum wells

MOCVD grown AlGaN/GaN MQWs have been irradiated with different heavy ions such as 200 MeV Au ions at a fixed fluence of $5x10^{11}$ ions/cm^2 [4], 80 MeV Ni and 120 MeV Au ions at a fixed fluence of $1x10^{12}$ ions/cm^2[5,6]. Several symmetric and asymmetric reflections were recorded to identify the zeroth order peak. Essentially, these measurements have also been used to estimate out-of-plane and in-plane strains from pristine and irradiated samples. Irradiated AlGaN/GaN MQWs with 200 MeV Au ions at a fluence of $5x10^{11}$ ions/cm^2 have shown improved interfaces which is evident from improved intensity of satellite peaks. The measured strain values show that strain increases upon irradiation. Moreover, improved band to band transitions are also observed from enhanced intensity of PL emission. Increase in intensity originated from band to band transitions has been attributed to ion beam induced dynamic annealing process. Therefore, it is reasonable to conclude that origin of intense yellow luminescence is related to recombination of distant donor-acceptor pairs which were created due to ion bombardment.

Aberration corrected Transmission Electron microscope has been used to understand the interfaces of pristine, irradiated MQWs and their buffer layers. In the pristine sample, an improved interface quality and reduced defects along the c-axis have been observed in the MQW region due to presence of AlN and GaN buffer layers. A large number of misfit dislocations at the GaN/AlN interface are seen to bend through the interlayer and thread through the AlGaN/GaN layers. Interface roughness is critical at the buffer layers and diminishes as it reaches the interfaces of MQWs. HAADF-STEM image from Ni ions irradiated MQWs reveal an insignificant difference in MQWs structure as compared to pristine MQWs. However, after 120 MeV Au irradiation, a drastic decrease in MQW quality and a significant increase in defect density are observed from HAADF-STEM images. It is evident from the HRXRD results that moderate electronic energy loss irradiation has improved the quality of the interfaces as compared to pristine AlGaN/GaN MQW interfaces. HRXRD also revealed that, after the initial improvement, the degradation of interfaces increases as electronic energy loss increases. At higher S_e there are two significant observations: a) a red shift and asymmetry in the E_2 (H) mode, which are attributed to ion beam induced intermixing b) a decrease in free carrier concentration where larger lattice damages are introduced. Finally, it is observed that ion beams for a

given projectile energy at a critical electronic energy loss for a fixed fluence does not show any detrimental effects in III- nitride compound semiconductors.

7.4 AlInN/GaN heterostructures

MOCVD grown tensile strained $Al_{(1-x)}In_xN$/GaN heterostructures were independently irradiated with Ni and Ag ions as a function of ion fluence. HRXRD, RBS and AFM characterization techniques have been used for understanding the structural and surface morphology of pristine and irradiated samples [7]. Philip's epitaxy simulation has been used for fitting the experimentally measured HRXRD scans of heterostructures to extract *In* composition. Similarly, the measured and simulated RBS spectra of $Al_{1-x}In_xN$/GaN heterostructures are compared. It is evident from the RBS spectra that *In* and *Al* signals corresponding to channels are completely separated from that of *Ga*. Increase in strain with increase of S_e has been noticed from HRXRD measurements. This means that there is an increase in Bragg angle of AlInN layer which could be attributed to ion beam induced lattice reduction. Eventually, this work demonstrates that the ion irradiation can create point defects which may result in lattice to expand or compress (reduction). Hence, irradiations modify the inter-planar spacing which consequently affected the strain. AFM images clearly show reduction in granular sizes with irradiation. Significantly, Ag ions at moderate ion fluence have resulted in lower surface roughness from 5 to 3.6 nm, while the reduction in rms roughness is insignificant (from 5 to 4.2 nm) for Ni ions irradiated samples.

SHI induced mixing effects in nearly lattice matched $Al_{(1-x)}In_xN$/GaN heterostructures have also been investigated as a function of electronic energy loss [8]. RBS technique has been used for determining composition profiles as a function of depth from surface in pristine and irradiated samples. Compositional inhomogenity has been observed in measured RBS spectrum of pristine sample but the average composition obtained from RBS and HRXRD does not show any variation. Moreover, observed diffusion gradient in RBS and HRXRD measurements is correlated with simulations. Change of strain status from nearly lattice matched / compressive strain to tensile strain has also been observed as a function of electronic energy loss. Here it is confirmed that the SHI induces preferential diffusion of Ga and In across the interface of AlInN/GaN heterostructures.

Thus, it is possible to achieve quaternary alloy (AlGaInN) in AlInN and GaN heterostructures by heavy ion bombardment which could be quite difficult during growth.

7.5 Future prospects

The interesting results obtained in the present investigations have opened up several new directions which should be pursued in future. It is known that ion beam interaction leads to several beneficial effects like nano structuring and healing of defects. On the other hand beyond critical beam parameters creation of defects through electron-phonon coupling has been identified. Defects introduced by implantation have been understood but there is only a limited understanding of defects introduced by swift heavy ions in general in all materials and in particular in III- Nitrides. Thus, it requires non-destructive technique like coherent acoustic phonon (CAP) interferometry for these studies. This has been used for quantification of point defects in ion implanted GaAs based semiconductors but there are no such studies on swift heavy ion irradiated samples. The current irradiations results establish that in GaN, the irradiations not only create defects but can also annihilate some other type of defects. Thus, such irradiated GaN films need to be investigated with coherent acoustic phonon technique to quantify the defect concentration as a function of depth. Another interesting subject is to enhance the optical properties of GaN with ion beams by reducing YL and BL emission related defects and are to be related to observed point defects from CAP technique. Optical responses to local defect concentration as a function of ion beam parameters and subsequent annealing temperatures are other interesting areas which could be investigated.

7.6 References

1. G Devaraju , S Dhamodaran, A P Pathak , G Sai Saravanan, J Gaca, M Wojcik, A Turos, S.A. Khan , D.K. Avasthi , B.M. Arora , Nucl. Instr. and Meth. B 266, 3552 (2008)
2. G Devaraju , A P Pathak , N Srinivasa Rao , V Saikiran , Francesco Enrichi , Enrico Trave , Nucl. Instr. and Meth. B 269, 1925 (2011)
3. G Devaraju , A P Pathak , N Sathish , N Srinivasa Rao , V Saikiran and A I Titov, Nucl. Instr. and Meth. B 269, 890 (2011)
4. G Devaraju, N Sathish, A P Pathak , A Turos , M Bazzan , E Trave , P Mazzoldi , B M Arora, Nucl. Instr. and Meth. B 268, 3001 (2010)

5. A P Pathak, G Devaraju, N Sathish , I Kyriakou, Vacuum, 84,1049, (2010)

6. G Devaraju, A P Pathak , N. Srinivasa Rao, V. Saikiran, N. Sathish, S. V.S Nageswara Rao (accepted for MRS proceeding 2011)

7. G Devaraju, A P Pathak, N Srinivasa Rao, V Saikiran, D Wang , T Scherer, A K Mishra and C Kübel (Accepted for publication in Radiation Effects and Defects in Solids)

8. G Devaraju, S V S Nageswara Rao, N Srinivasa Rao, V Saikiran,T K Chan ,T Osipowicz, M B H Breese and A P Pathak (submitted to in Radiation Effects and Defects in Solids)

<div align="center">

CURRICULAM VITAE

</div>

<div align="right">

Devaraju Gurram
School of Physics
University of Hyderabad
Central University P O, Hyderabad- 500 046, India
Contact number : +91 9440880309
Email: devaraju_hcuin@yahoo.co.in ; ph06ph12@uohyd.ernet.in

</div>

Objective

It is my endeavour to investigate and understand the influence of interface defects on structural, optical and electrical properties of advanced materials for device applications

Current position

• Pursuing PhD (Physics) under the supervision of Prof A P Pathak, School of Physics, University of Hyderabad

Educational details

- M.Sc (Physics) with **first division**, School of Physics, University of Hyderabad, 2003
- All the necessary course works have been completed with distinctions both at University of Hyderabad and Inter university accelerator center, New Delhi.
-

Project experience

Project entitled "Rutherford Backscattering Spectroscopy Study of Channelling and Channelling Radiation at Stacking Faults" has been carried out as an M. Sc project under the supervision of Prof A P Pathak.

Research Experience

- Worked as a **JRF in UFUP** project sanctioned to Prof A P Pathak from Aug 2006 to July 2008
- Worked for **Center for Nano technology as a JRF** since July 2008 to March 2010.
- Working as **CSIR–DSRF** from 01.04.2010 to till date
- Worked as visiting scholar in Prof Mazzoldi's Lab at **University of Padova, Italy**, 28th Feb to 15th March, 2009.
- Worked as visiting scholar in Prof Mazzoldi's Lab at **University of Padova, Italy**, 08.07.2010 to 17.07.2010
- Selected for **Research Fellowship in Science for Meritorious Students** (RFSMS) from Centre for Advanced studies, which is sponsored by UGC

Teaching Experience

- Worked as a Asst. Prof of Physics for Royal college of Engineering, Medak from 08.07.2004 to 06.06.2006

Oral presentations (International conferences)

- 24th International Conference on Atomic Collisions in Solids, Krakow-Poland
- Materials Research Society, 24th & 29th April, 2011, San Francisco, USA

Travel support

- **DST-PURSE** grant at University of Hyderabad sanctioned funds to attend and present paper at 24th International Conference on Atomic collisions in solids (ICAS-24), Krakow-Poland
- Selected for **DST International Travel Scheme** to attend and present research work at prestigious Material Research Society (MRS)-2011, San Francisco, USA

Conferences/Workshops attended (presented posters):

1. Workshop on Nanotechnology with ion beams and possible applications, IUAC-New Delhi, 31st Oct - 1st Nov. 2006

2. Workshop on "Advanced X-Ray Techniques for Characterization of Nano Materials (XTNM-2008)" DMRL, Hyderabad, 27th Feb - 29th Feb. 2008.

3. Presented a poster at 18th International Conference on Ion Beam Analysis (IBA), School of Physics, University of Hyderabad, Hyderabad, 23rd Sept - 28th Sept. 2007.

4. "Material Characterization and surface modification in Research and Industry using ion Accelerator (MCIA)" IOP, Bhubaneswar, March 31st March - 4th April, 2008.

5. "Optoschool 2008" ,TIFR, 27th July to 2nd Aug. 2008

6. "Gallium Nitride: Growth, Characterization and Device applications (GAETEC)" Hyderabad, 13th June 2008.

7. Workshop on Advanced simulations for ion beam analysis by IAEA and ICTP, Trieste, Italy, 22nd Feb - 27th Feb. 2009.

8. Presented a poster at India-Singapore Joint Physics Symposium (ISJPS-2010), School of Physics, University of Hyderabad, 19th Feb -21st Feb. 2010

9. 24th International Conference on Atomic Collisions in Solids, Krakow-Poland , 19th July - 23rd July, 2010

10. Presented a poster at Materials Research Society-2011, San Francisco, USA, 24th & 29th April, 2011

11. Presented a poster at 50th International conference of Electron Microscopy, DMRL, Hyderabad, 6th July - 8th July, 2011

12. Presented a poster at Frontiers in Physics, School of Physics, University of Hyderabad, 27th & 28th Oct, 2011

Publications list

1. Ion beam modification of strained InGaAs/InP characterized by HRXRD, PL and AFM, G Devaraju , S Dhamodaran , A P Pathak , G Sai Saravanan , J Gaca , M

Wojcik ,A Turos , S A Khan , D K Avasthi , B M Arora, **Nucl. Instr. and Meth. B** 266, 3552 (2008)

2. Ion beam modification studies of InP based multi quantum wells**,** S. Dhamodaran, G. Devaraju, A.P. Pathak, A. Turos, D.K. Avasthi, R. Kesavamoorthy, B.M. Arora, **Nucl. Instr. and Meth. B** 266, 1810 (2008)

3. Investigation of strain in AlGaN/GaN Multi Quantum Wells by complementary techniques, **AIP Conf. Proc**. 1099, 353 (2009), G. Devaraju, N. Sathish, A. P. Pathak, S. Dhamodaran, J. Gaca, M. Wojcik, A. Turos, and B. M. Arora.
(Invited talk by Prof A P Pathak)

4. Effects of swift heavy ion irradiation on band gap of strained AlGaN/GaN Multi Quantum Wells, G Devaraju, A P Pathak, et al. **Nucl. Instr. and Meth. B** 268, 3001(2010),

5. Ion beam studies of multi-quantum wells of III-nitrides**,** A P Pathak, G Devaraju et al. **Vacuum**, 84,1049, (2010)

6. Synthesis of Ge nanocrystals by atom beam sputtering and subsequent rapid thermal annealing, N Srinivasa Rao, A P Pathak and G Devaraju et al. **Solid State Communications**, 150, 2122 (2010)

7. SHI induced re-crystallization of Ge implanted SiO_2 films**,** N Srinivasa Rao, A P Pathak, G Devaraju et al. **Nucl. Instr. and Meth. B** 268, 11-12, (2010), 1741,

8. Electronic stopping dependence of Ion beam induced modifications in GaN**,** G Devaraju, A P Pathak et al. Nucl. Instr. and Meth. B 269, 890 (2011)

9. Growth and characterization of nc-Ge prepared by microwave annealing, N Srinivasa Rao, A P Pathak, G Devaraju et al. **Vacuum**, 268,1741, (2010)

10. Photoluminescence and Photoluminescence excitation studies in 80 MeV Ni ions irradiated MOCVD grown GaN, G Devaraju, A P Pathak et.al, **Nucl. Instr. and Meth. B** 269, 1925 (2011)

11. Ion beam treated strained AlGaN/GaN multi quantum wells: HAADF- STEM, HRTEM, Raman and HRXRD characterizations, G Devaraju, A P Pathak et al (Accepted for publication in **Radiation Effects and Defects in Solids**)

12. Structural Changes Induced by Swift Heavy Ion Beams in tensile strained Al $_{(1-x)}$In$_x$N /GaN Hetero-structures**, Accepted for MRS proceedings** 2011

13. Ion beam mixing effects in nearly lattice matched AlInN/GaN hetero structures by swift heavy ion irradiation, G Devaraju, A P Pathak et.al, in press **Radiation Effects and Defects in Solids**)
14. SHI induced effects in FMWCNTs, V Saikran, A P Pathak, N Srinivasa Rao, G Devaraju et.al, under review REDS

15. Synthesis and Tailoring of GaN nanoparticles by RF magnetron sputtering at Room Temperature, G Devaraju, A P Pathak et al (Under preparation)

PERSONAL PROFILE

Name   : G. Devaraju
Date of Birth   : 01.08.1979
Languages Known   : English, Hindi, and Telugu

References:

1. Prof A P Pathak
   School of Physics
   University of Hyderabad
   appsp@uohyd.ernet.in
   anandp5@yahoo.com

2. Prof B M Arora
   Department of Electrical Engineering
   IIT Mumbai, Mumbai
   arora.brijmohan@gmail.com

3. Prof G Mattei
   Department of Physics
   University of Padova
   Italy
   giovanni.mattei@unipd.it